

4434

LIBRARY
JAWAHARLAL NEHRU CENTRE
FOR ADVANCED SCIENTIFIC RESEARCH
JAKKUR POST
BANGALORE - 560 064



A Wavelet Analysis of Possible Connections Between Solar Processes, Indian Monsoon Rainfall and ENSO Indices



A Thesis
Submitted for the Degree of
DOCTOR OF PHILOSOPHY

by
SUBARNA BHATTACHARYYA



ENGINEERING MECHANICS UNIT
JAWAHARLAL NEHRU CENTRE FOR ADVANCED SCIENTIFIC
RESEARCH
(A Deemed University)
Bangalore - 560 064

DECEMBER 2005

LIBRARY
JAWAHARLAL NEHRU CENTRE
FOR ADVANCED SCIENTIFIC RESEARCH
JAKKUR POST
BANGALORE - 560 064

To my parents

532.593

PO5

DECLARATION

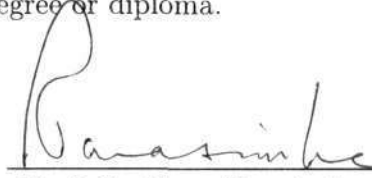
I hereby declare that the matter embodied in the thesis entitled “ **A Wavelet Analysis of Possible Connections Between Solar Processes, Indian Monsoon Rainfall and ENSO Indices**” is the result of investigations carried out by me at the Engineering Mechanics Unit, Jawaharlal Nehru Centre for Advanced Scientific Research, Bangalore, India under the supervision of Prof. Roddam Narasimha and that it has not been submitted elsewhere for the award of any degree or diploma.

In keeping with the general practice in reporting scientific observations, due acknowledgment has been made whenever the work described is based on the findings of other investigators.

Subarna Bhattacharyya.
Subarna Bhattacharyya

CERTIFICATE

I hereby certify that the matter embodied in this thesis entitled “ **A Wavelet Analysis of Possible Connections Between Solar Processes, Indian Monsoon Rainfall and ENSO Indices**” has been carried out by Ms. Subarna Bhat-tacharyya at the Engineering Mechanics Unit, Jawaharlal Nehru Centre for Ad-vanced Scientific Research, Bangalore, India under my supervision and that it has not been submitted elsewhere for the award of any degree or diploma.



Prof. Roddam Narasimha

(Research Supervisor)

Acknowledgements

Its now time for me to take few moments and reflect back on all the tremendous efforts it took not only on my part, but also on all those around me without whose unconditional support my thesis would not have seen the light of this day.

I have the great fortune and privilege of working under the supervision of a legendary scientist and personality like Prof. Roddam Narasimha. I express my sincere gratitude to him for allowing me to work under his supervision. Right from imparting technical guidance, building confidence in my research work, exuberating inspiration, giving me exposure to various kinds of subjects to enable multidisciplinary interactions and applications, inspiring me to speak at scientific conferences both in India and abroad, enabling meetings with peers in my field of work, and yet relentlessly correcting all my mistakes however silly they are, – I am really indebted to him for such endless list of wise suggestions and advices both in my research and personal life. I am ever so thankful to Mrs. Narasimha for her warm hospitality.

I owe sincere gratitude to Prof. Arnab Rai Choudhuri of Physics Department of Indian Institute of Science (IISc) for providing us the solar process data and also helping us to understand the basics of solar physics that causes the sunspot and its cycle. I am very thankful to Prof. P. G. Vaidya of National Institute of Advanced Studies (IISc campus) who gladly obliged us whenever we needed a discussion and feedback on our methods and results of research. His much valued advice has helped us a great deal in performing the analysis with noise signals. I am thankful to Prof. R. N. Iyengar for his advices on applying time-frequency methods to rainfall analyses. For all the wavelet analyses that I learnt, I thank Prof. G. V. Anand of department of Electrical Communication Engineering (IISc), Prof. Vittal Rao of Mathematics department (IISc) and of course Prof. R. Narasimha. Dr. H. N. Shankar of Peoples' Education Society (PES) Engineering College, Bangalore, has helped me to a great extent with basics of linear algebra and vector spaces.

During my course of work I corresponded and even met with eminent scientists whose suggestions took us a long way into our research. I am grateful to Sir D. R. Cox (Imperial College, London) for his suggestions on modelling long-range dependencies. I am thankful to Prof. D. J. Thompson (Queens University, Canada) for very useful discussions on statistical signal processing in handling nonlinearity and nonstationarity in geophysical signals. I am also thankful to Dr. Umberto Amato (Scuola di Matematica Computazionale, Napoli, Italy), Prof. Brani Vidakovic (Georgia Institute of Technology, USA), Prof Raymond O Neil (International University of Bremen, Germany) for their valuable comments and suggestions on wavelet analysis and applications.

Discussions with scientists from the solar-terrestrial community present at the SORCE 2005 meeting in Durango, Colorado, USA, particularly, Prof Gary Rottman (National Centre for Atmospheric Research, Colorado), Prof Harry van Loon (North West Research Associate, Colorado), Dr. K. Kodera (Meteorological Research Institute, Japan) , Dr. Drew Shindell (NASA Goddard Institute for Space Studies), Dr. Judith Lean (Naval Research Laboratory), Prof. Joan Feynman (NASA Jet Propulsion Laboratory), Prof A. Ruzmaikin (NASA Jet Propulsion Laboratory), Dr. Madhulika Guhathakurata (NASA Hq, Washington D.C.), Prof. S. Solanki

(Max-Planck Institute fur Sonnensystemforschung, Germany), Dr. Julia Saba (Lockheed Martin) and Dr. Keith Strong (Lockheed Martin), have inspired me immensely and helped me fine tune several aspects of my work.

I am thankful to all members of the academic and administrative section of my institute JNCASR for their support and help throughout the period of my thesis. I am grateful to the administrative officer, Mr. A. Jaychandra for providing me accomodation for myself and my family, time and again during this period. Prof. Rama Govindarajan and Dr. K. R. Sreenivas of EMU have always been a source of moral support and inspiration that made my stay in JNC very memorable. Vinod, Sameen and Kirti have been very helpful as colleagues and friends. I am grateful to Ms. J. Lakshmi of National Institute of Advanced Studies who has helped us to prepare the diagrams in the 9th chapter in particular.

I express my sincere gratitude to Ms. K. Nagarathna (SERC, IISc) for being a tremendous source of mental and moral support right from the first day that I joined in this PhD program. She has always been a true freind, who has been constantly helping and guiding me through many of my difficult times. Sarita also has been a great friend and of tremendous help to me both intellectually and spiritually.

Friends like Sutirtha, Sanjib, Subhabrata, Sudipta and Swaraj, have made my stay here quite homely and delightful. Taking refuge in musical and cultural endeavours with Sanjib, Satyaki, Biswaroop, Amitava, Pradyut and many others have provided me with much needed recreations and welcome breaks from my otherwise computing schedules. Sutirtha and Sanjib always provided me with any and all kinds of technical help whenever and wherever I needed them.

Last but not the least I convey my deepest gratitude for my parents who have always encouraged and inspired me to strive for the best in whatever I do and have unconditionally and unquestioningly supported me in this endeavour. Had it not been for my husband Sanjib and his unflinching support and inspiration through all these enduring years, it would not have been possible for me to complete this colossal work. I am much indebted to my parents-in-law who have actively supported me through this trying period. I am much thankful to my little son Soham who has actively cooperated in all my efforts. Special thanks are due to my mother and mother-in-law, together with my brothers Ratnadeep, Joydeep, Rajeev, Mithu, Rintu and Shyam who have actively contributed in taking care of Soham and bringing him up. Ratnadeep and Joydeep deserve special thanks for providing me much needed moral support during this time.

Subarna Bhattacharyya
23rd December 2005

Preface

That solar activity influences climate and long term variability is now a well-accepted idea as evidence for possible association between solar processes and terrestrial climate indices keeps getting stronger. However it has not been clear whether there are any such significant effects on shorter time scales (of the order of 10 to 100y). The idea that the tropics can amplify a small radiant flux signal to a relatively large and dynamic climate change, in the tropics as well as elsewhere in the world, serves to provide motivation for the present work. The main objective here is to investigate possible connections between solar activity, Indian monsoon rainfall and the El-Nino southern oscillation (ENSO) indices, using different methods of time series analysis. The present thesis is arranged into 11 chapters and an appendix, the contents of which are briefly stated below.

The first chapter presents a survey of previous work on solar-terrestrial relations. In general such work has been somewhat sceptically received by much of the meteorological community for several reasons: the associations have not always been statistically significant at sufficiently high levels, reliable data using modern instrumentation is available only for a relatively short period of time (of order 100 years), and no completely convincing physical mechanisms that may explain links between solar and meteorological processes on such relatively short time scales have yet been established. However, there has been renewed interest in this field in the recent past especially with the advent of newer mathematical tools of time series analysis like wavelets, coupled with availability of increasingly reliable climatic records. In chapter 2 we present a detailed description of all the rainfall, solar activity and ENSO indices analyzed in this study. The rainfall indices pertain to the five different homogeneous rainfall regions identified by Parthasarathy et al. (1993), the homogeneous Indian monsoon (HIM) rainfall, and the all India summer monsoon rainfall (AISMR). In some of the present work, we also look at the annual rainfall from each of 29 meteorological subdivisions in India. The often-used AISMR is not the best rainfall index for analysis, as the geographical area it covers is meteorologically heterogeneous, and so physically coherent signals will tend to be weaker as illustrated by the present analyses. The solar indices under study are the annual sunspot numbers, group sunspot numbers and the solar irradiance. The ENSO indices under consideration are the global ENSO index, the Nino3.4 SST and the Nino3 SST.

A time domain analysis of all the above-mentioned data is performed and the results are reported in chapter 3 of the thesis. Over the 120 y period (1871-1990) for which reliable Indian rainfall statistics are available, solar activity parameters exhibit nonstationarity. Taking this fact into account, we present the results of an analysis of three solar activity and seven Indian monsoon rainfall indices. Statistics are compared over two distinct test periods respectively of low and high solar activity, each comprising three complete solar cycles, offering the highest contrast within the analysed period of 120 y. It is found that the average rainfall is higher in all seven rainfall indices during periods of greater solar activity, at confidence levels varying from 75% to 99%, being 95% or greater in three of them.

Chapter 4 presents a simple wavelet analysis. It is found that the power in the 8-16 y band during the period of higher solar activity is higher in 6 of the 7 rainfall time series, at confidence

levels exceeding 99.99% in all 6 cases. These results, together with those of the time domain analysis, support existence of connections between Indian rainfall and solar activity.

The methods adopted in Chapters 3 and 4 are simple and direct, and involve the solar activity index solely to identify appropriate test periods; the quantitative value of the index does not affect the statistic tested. In order to assess possible quantitative connections with solar processes, we next present results from a wavelet cross-spectral analysis in chapter 5. The cross spectra are computed for rainfall-solar activity, ENSO-rainfall as well as ENSO-solar activity. The statistical significance of the computed cross-spectra is first estimated from the procedure proposed by Torrence and Compo (1998). It will be shown that this procedure suggests very high significance levels which could often be quite misleading when one of the processes (sunspots in this case) has strong periodicities on longer time scales.

Chapter 6 presents a new procedure that is proposed here to overcome the above mentioned limitation of the Torrence-Compo procedure. The principle behind the new procedure is to compare the cross spectrum under question with that between solar activity and three specially generated noise signals, one white (WN) and the other two simulating respectively the frequency spectrum (SN) and amplitude probability distribution (AN) of rainfall. This procedure is in part of the Monte Carlo type. The difference in solar-rainfall and solar-noise cross spectra is then subjected to standard statistical tests. Over the two test-periods identified in Chapter 3, the average cross power of the solar activity index with HIM rainfall exceeds that with the noise at z -test confidence levels exceeding 99.99% over period-bands covering the 11.6 y sunspot cycle. These results provide strong additional evidence for connections between Indian rainfall and solar activity.

In Chapter 7 we repeat this analysis for all the other homogeneous zone rainfall time series in India, in order to explore the spatial variations between the different homogeneous regions. The results show that West Central India (WCI), North West India (NWI) and AISMR are similar in their temporal characteristics, while North East India (NEI) is distinctly different from all of them. Central North East India (CNEI) and Peninsular India (PENSI) have characteristic features that are in between those of WCI and NEI. Cross spectral analysis confirms that greater solar activity is associated in all cases with greater rainfall (supporting the conclusion from time-domain analysis), although at significance levels that are distinctly high ($> 95\%$) in 3 (HIM, WCI and AISM) and lower ($< 90\%$) in 4 (NWI, CNEI, NEI and PENSI) out of the 7 cases studied. This variation is organized roughly along the longitude across the country. This regional variation is not inconsistent with the simulations of Haigh *et al.* (2004), showing a displacement of the Hadley cell depending on solar activity.

Evidence presented in Chapter 8 shows that connections of ENSO with these solar process parameters are statistically stronger than those between ENSO and summer monsoon rainfall. The global wavelet cross spectra between solar irradiance and monsoon rainfall, and that between irradiance and the ENSO index, show significant power around the period of the 11 year solar cycle, passing the chi-squared test of significance proposed by Torrence and Compo (1998) at levels exceeding 95% and 97.5% respectively. The global wavelet cross power spectra between the ENSO index and the all India summer monsoon rainfall show a peak in the 3-4 year period range at significance levels of only 70%. Two distinct test-periods are found in the computed cross-spectrum showing that the average rainfall is higher when average ENSO index is lower, which coincides with periods of greater solar activity; the z -test confidence levels for the connections exceed 95%. Even over the slightly longer period of 1850-1998 over which the AISMR has been reconstructed, statistical analysis reveals significant influence by sunspots and solar irradiance, particularly over the two test-periods defined earlier. An increase in solar activity decreases

ENSO but increases rainfall at the 8-16 y band. The link between ENSO and solar activity is weaker than the link between solar activity and rainfall but stronger than that between ENSO and rainfall. The effect of Nino 3.4 positive tendencies on the monsoon rainfall is to decrease the rainfall. Both these effects occur in the test periods of lower solar activity.

The global cross spectrum for ENSO and solar activity index exhibits peaks around the 11 y period at confidence levels of 90% or higher. In particular, the confidence level for the solar irradiance-ENSO index is as high as 97.5%. This confirms that there is a stronger connection between ENSO and solar activity as compared to the ENSO-rainfall connection. Greater solar activity is associated with lower ENSO activity and vice-versa, supporting the well-known inverse relationship between ENSO and rainfall. More importantly, this finding suggests that Indian rainfall is affected by solar processes indirectly through ENSO. A detailed investigation of the ENSO-monsoon triad over the two test periods identified in Chapter 3 provides additional insight into the more complex mutual relationships in the triad. An increase in solar activity decreases the ENSO index and increases the monsoon rainfall in the 8-16 y period band, but has the opposite effect in the 2-7 y period band. The net effect of solar processes on rainfall thus appears to be the result of counteracting influences on short and long periods, the latter on the whole dominating over the former.

The problem of the association between solar processes and rainfall is tackled by a simple new wavelet technique in Chapter 9. This method provides information on the phase relationships between sunspots and rainfall, an issue that the other two methods adopted in the thesis cannot tackle. The wavelet transform coefficient maps of sunspot number and HIM rainfall annual time series reveal striking similarities, around the 11-year period. The novel method suggested in this chapter treats maxima in the absolute value of the wavelet transform coefficient at the 11-year period, for sunspot and rainfall data, as point processes in time. A statistical scheme for identifying the dependence between the two processes is devised. A regression analysis of parameters in these processes reveals a nearly linear trend, with small but systematic deviations from the regressed line. Suitable periodic function models for these deviations have been obtained through an unconstrained error minimisation scheme. These models provide an excellent fit to the point process data. Statistical significance tests suggest with 99% confidence that the residual deviations are sample fluctuations obtained from normal distributions. It is concluded that sunspot-rainfall phase relations are modulated by cycles of longer periods (of order 40-100 y).

In chapter 10 we summarise all the results obtained and conclude that, over durations of a few decades, three independent statistical procedures all confirm that Indian monsoon rainfall increases in periods of higher solar activity and decreases in periods of lower solar activity. However this effect has a distinct spatial variation spread over the country as a whole. ENSO indices decrease during periods of higher solar activity and increase during lower solar activity periods; there are spatial variations in the ENSO-monsoon relationship as well. Chapter 10 also examines possible explanations for the results obtained and suggests a schematic model for the complex dynamics underlying associated atmospheric processes, and discusses new vistas for future investigations.

Publications

- Bhattacharyya S., Narasimha R. and Rai Choudhuri A., (2002), Analysing the wavelet maps of north east Indian rainfall and sunspot index time series data, *Proceedings of International Conference and Instructional Workshop on Wavelet Analysis, 4-8th January, Chennai, India.*
- Bhattacharyya S. and Narasimha R. (2003), Wavelet cross spectral analysis of Indian monsoon rainfall and solar activity parameters, *Symposium on Advances in Fluid Mechanics, July 24th-25th, Jawaharlal Nehru Centre For Advanced Scientific Research, Bangalore, India.*
- Bhattacharyya S., and R. Narasimha, (2003), Wavelet Analysis Of Monsoon Variability As Affected By Solar Processes, *Proceedings of Scale Interaction and Variabilities of Monsoon SiVoM 6th-10th October 2003, Munnar, India.*
- Bhattacharyya S., and R. Narasimha. (2004), Wavelet analyses of connexions between solar process and Indian monsoon rainfall, poster presented at *European Geophysical Union conference, 25th-30th April, Nice, France, 2004.*
- Bhattacharyya S. and R. Narasimha, (2004), Indian rainfall increases in epochs of higher solar activity, *Workshop on Wavelet Analysis and Applications, Electrical Communications Engineering, Indian Institute of Science, Bangalore, India, 9-10th August.*
- Bhattacharyya, S., and R. Narasimha (2005), Possible association between Indian monsoon rainfall and solar activity, *Geophys. Res. Lett.*, 32, L05813, doi:10.1029/2004GL021044.
- Bhattacharyya, S., and R. Narasimha (2005), Evidence of strong link between Indian rainfall and solar activity, presented at the *SORCE 2005 meeting in Colorado, USA during 14th-16th September 2005. To appear in 'The Earth Observer'.*
- Bhattacharyya, S., and R. Narasimha (2005), A novel analysis of the connection between Indian monsoon rainfall and solar activity, accepted for presentation at the *Fall Meeting of American Geophysical Union (AGU) at San Francisco during 5-8 December 2005, Eos Trans. AGU, 86, 52.*
- Bhattacharyya, S., and R. Narasimha (2005), Wavelet cross-spectral analysis of Indian monsoon rainfall and solar activity, 2005GL024505, Communicated to *Geophys. Res. Lett.*
- Bhattacharyya, S., and R. Narasimha (2005), Connections between ENSO, Indian monsoon and Solar processes using wavelet analysis, *To be submitted*
- Bhattacharyya, S., and R. Narasimha (2005), A novel analysis of the connection between Indian monsoon rainfall and solar activity using wavelet analysis and point process methods, *To be submitted*

Tables

3.1	Confidence levels for homogeneous rainfall regions	28
3.2	z test confidence levels for the subdivisions	32
4.1	Values of z statistic for the rainfall, ENSO and solar activity	42
5.1	Highest significance levels obtained in cross spectra	60
7.1	Probability density function of rainfall	76
7.2	Probability distribution function of rainfall	76
7.3	Transformation function for simulating PDF matched noise signals for rainfall	77
7.4	Confidence level from z test for rainfall, and test signals WN, SN, AN	77
9.1	Table for model parameters for various metrological subdivisions	124
10.1	% Contribution to cross power	133
10.2	% Contribution to cross power (contd)	134

Figures

2.1	Map of sub divisions	16
2.2	Map of homogeneous regions	17
2.3	Rainfall time series of 6 homogeneous regions	18
2.4	Rainfall time series of 10 subdivisions.	18
2.5	Rainfall time series of next 10 subdivisions.	19
2.6	Rainfall time series of next 9 subdivisions.	20
2.7	Solar Activity Time Series.	21
2.8	Solar Activity Time Series. The bottom panel shows the solar irradiance reconstruction by Lean (2004)	22
2.9	SST Time Series.	23
3.1	Time series of three solar indices, indicating test periods of low and high solar activity selected for analysis, and the means over the test periods for each parameter in green and red respectively.	26
3.2	Time series showing four Indian rainfall indices, indicating test periods of low and high solar activity selected for analysis, and the means over each test period.	27
3.3	Map showing homogeneous monsoon regions of India. Marked in bars are the % difference of rainfall means over test periods with respect to the annual means and encircled numbers next to them indicate the confidence level at which the differences are significant.	29
3.4	Rainfall differential map of meteorological subdivisions of India. Marked in colours are the % confidence levels to which the difference of rainfall means over the two test periods are significant. Red: 95–99.99%, orange: 90–95%, yellow: 80–90%, green: 70–80%, blue: 60–70% and cyan: 50–60%.	30
3.5	Nino3, Nino3.4 and global ENSO time series. Marked in red are the respective means over the test-period 1 which are greater than the means marked in green for test-period 2 at the indicated confidence levels by the z -test.	31
3.6	Rainfall over homogeneous regions, sunspot number and global ENSO time series. Means marked in red are greater than the means marked in green over the five-cycle test-periods considered, at the indicated confidence levels by the z -test.	31
4.1	The real and imaginary part of the complex morlet wavelet in the time domain	35
4.2	Wavelet power spectrum of HIM rainfall (top panel) and sunspot number (bottom panel)	36
4.3	Wavelet power spectrum of WCI rainfall (top panel), NWI rainfall (middle panel) and AISM rainfall (bottom panel)	37
4.4	Wavelet power spectrum of NEI rainfall (top panel), CNEI rainfall (middle panel) and PENSI rainfall (bottom panel)	38
4.5	Wavelet power spectrum of ENSO (top panel), NINO 3.4 (middle panel) and NINO 3 (bottom panel) sst index.	38

4.6	Individual wavelet power over different period bands as percentages of the total individual wavelet power. Band (1): 1–2 y, (2): 2–4 y, (3): 4–8 y, (4): 8–16 y, (5): 16–32 y, (6): 32–64 y; the band limits are closed on the left and open in the right of the interval.	39
4.7	8–16 y, 9–13 y and 10–12 y Band averaged wavelet power: HIM, WCI, NWI rainfall in the top three panels and Sunspot number in the bottom panel. Marked on respective curves are straight lines showing the means over each of the two test periods.	40
4.8	8–16 y, 9–13 y and 10–12 y Band averaged wavelet power: CNEI, PENSI, NEI rainfall in the top three panels and Group Sunspot number in the bottom panel. Marked on respective curves are straight lines showing the means over each of the two test periods.	41
4.9	8–16 y, 9–13 y and 10–12 y Band averaged wavelet power: AISM rainfall, ENSO, Nino 3.4, Nino 3 SST indices in the top four panels and solar irradiance in the bottom panel. Marked on respective curves are straight lines showing the means over each of the two test periods.	41
5.1	Wavelet cross power spectrum between HIM rainfall and sunspot number, contours showing regions at 50% to 99% confidence level	46
5.2	Global wavelet cross power spectrum between HIM rainfall and sunspot number	47
5.3	Wavelet cross power spectrum of five homogeneous and AISM rainfall with sunspot number. Contours of regions with 90%, 95% and 99% are shown respectively in green, blue and white lines.	48
5.4	Global wavelet cross power spectrum of five homogeneous rainfall and AISM with sunspot number. Sunspot, Rainfall and Cross Spectrum shown respectively in red, blue and black lines. Confidence lines marked in red dashed lines and confidence levels indicated in each figure.	49
5.5	Wavelet cross power spectrum between AISM rainfall and solar irradiance, green and blue thick contours mark regions where the cross spectrum exceeds the reference spectrum at 90% and 95% confidence level respectively.	49
5.6	Global wavelet cross power spectrum between AISM rainfall and solar irradiance, dashed line mark regions where the cross spectrum exceeds the reference spectrum at 95% confidence level	50
5.7	Wavelet cross power spectrum between homogeneous rainfall and solar irradiance, green and blue thick contours mark regions where the cross spectrum exceeds the reference spectrum at 90% and 95% confidence level respectively.	50
5.8	Wavelet cross power spectrum between ENSO index and HIM rainfall, blue thick contours mark regions where the cross spectrum exceeds the reference spectrum at 95% confidence levels.	51
5.9	Global Wavelet cross power spectrum between ENSO index and HIM rainfall, dashed lines mark regions where the global cross spectrum exceeds the reference spectrum at 65% confidence levels.	52
5.10	Wavelet cross power spectrum of ENSO index with five homogeneous and AISM rainfall; blue thick contours mark regions of 95% confidence levels.	53
5.11	Global Wavelet cross power spectrum of ENSO index with AISM rainfall, dashed lines mark regions where the global cross spectrum exceeds the reference spectrum at 67.5% confidence levels.	54

5.12	Global Wavelet cross power spectrum between ENSO index and NEI rainfall, dashed lines mark regions where the global cross spectrum exceeds the reference spectrum at 85% confidence levels.	54
5.13	Global Wavelet cross power spectrum between ENSO index and NWI rainfall, dashed lines mark regions where the global cross spectrum exceeds the reference spectrum at 75% confidence levels.	55
5.14	Global Wavelet cross power spectrum between ENSO index and CNEI rainfall, dashed lines mark regions where the global cross spectrum exceeds the reference spectrum at 75% confidence levels.	55
5.15	Global Wavelet cross power spectrum between ENSO index and PENSI rainfall, dashed lines mark regions where the global cross spectrum exceeds the reference spectrum at 75% confidence levels.	56
5.16	Wavelet cross power spectrum of ENSO index with sunspot number (top panel) and solar irradiance (bottom panel), blue thick contour mark regions where the cross spectrum exceeds the reference spectrum at 90% confidence level	57
5.17	Global wavelet cross power spectrum between ENSO index and sunspot number, dashed line mark regions where the cross spectrum exceeds the reference spectrum at 90% confidence level	58
5.18	Global wavelet cross power spectrum between ENSO index and solar irradiance, dashed line mark regions where the cross spectrum exceeds the reference spectrum at 97.5% confidence level	58
5.19	Wavelet cross power averaged over different period bands as percentages of the total wavelet cross power. Band (1): 1–2 y, (2): 2–4 y, (3): 4–8 y, (4): 8–16 y, (5): 16–32 y, (6): 32–64 y; the band limits are closed on the left and open in the right of the interval.	59
5.20	Homogeneous rainfall map of India showing percentage confidence levels at which the sunspot-rainfall global cross spectrum peaks.	61
5.21	Homogeneous rainfall map of India showing percentage confidence levels as well as the period at which the ENSO-monsoon global cross spectrum peaks.	62
6.1	Time series of solar index, HIM rainfall and the three test signals for noise, indicating in each case the means over the test periods of low and high solar activity. The numbers marked in between the means indicate the percentage confidence levels at which the difference between means over the two periods is significant by the z-test.	65
6.2	Comparison of probability distribution of AN and spectrum of SN with corresponding characteristics of HIM rainfall	66
6.3	Wavelet cross power spectrum of HIM rainfall and sunspot number (top panel) and that between WN and sunspot number (bottom panel)	68
6.4	Global wavelet cross power spectra and confidence lines obtained from Torrence and Compo (1998) test.	69
6.5	Difference between wavelet cross power of HIM-sunspot and (1) WN-sunspot (top panel), (2)SN-sunspot (middle panel), (3)AN-sunspot (bottom panel).	70
6.6	Wavelet cross power averaged over 8–16 y, 9–13 y and 10–12 y bands, with means in the two test periods.	71
7.1	Comparison between PDF and Spectrum of target and simulated rainfall for five homogeneous regions and AISM.	78

7.2	A sample of three test signals WN, SN, AN alongwith sunspot number and WCI rainfall.	79
7.3	Global wavelet cross power spectra for rainfall-Sunspot and WN-Sunspot.	80
7.4	Mean Cross spectra of sunspot number with WN, SN and AN for WCI rainfall.	81
7.5	Difference between WCI-sunspot cross spectra and mean test signal-sunspot number cross spectra for each test signal.	82
7.6	Mean Cross spectra of sunspot number with WN, SN and AN for NWI.	82
7.7	Difference between NWI-sunspot cross spectra and mean test signal-sunspot number cross spectra for each test signal.	83
7.8	Mean Cross spectra of sunspot number with WN, SN and AN for CNEI.	83
7.9	Difference between CNEI-sunspot cross spectra and mean test signal-sunspot number cross spectra for each test signal.	84
7.10	Mean Cross spectra of sunspot number with WN, SN and AN for NEI.	84
7.11	Difference between NEI-sunspot cross spectra and mean test signal-sunspot number cross spectra for each test signal.	85
7.12	Mean Cross spectra of sunspot number with WN, SN and AN for PENSI.	85
7.13	Difference between PENSI-sunspot cross spectra and mean test signal-sunspot number cross spectra for each test signal.	86
7.14	Mean Cross spectra of sunspot number with WN, SN and AN for AISM.	86
7.15	Difference between AISM-sunspot cross spectra and mean test signal-sunspot number cross spectra for each test signal.	87
7.16	9-13, 8-16 and 10-12 y band averaged wavelet cross power of rainfall and the test signals with sunspot number with means marked over the two solar activity test periods for all homogeneous rainfall and AISM.	88
8.1	Raw time series of AISM rainfall in mm, ENSO index in hundredth of a degree Centigrade, solar irradiance in W/m^2 , and sunspot number, indicating epochs of low and high solar activity selected for analysis, and the means over the epochs for each parameter. The difference in means over the two test periods are significant at greater than 97%, 95%, 99.999% and 99.9% by the <i>z</i> -test, for AISM rainfall, ENSO index, solar irradiance and sunspot numbers respectively.	92
8.2	Wavelet cross power spectrum between ENSO index and solar irradiance (Top panel) and between sunspot number and AISM rainfall (Bottom panel). Contours in green, blue and black mark regions where the cross spectrum exceeds the reference spectrum at 90%, 95% and 99% confidence levels respectively.	93
8.3	Wavelet cross power spectrum between ENSO index and AISM rainfall(Top panel) and between ENSO index and sunspot number (Bottom panel). Contours in green and blue mark regions where the cross spectrum exceeds the reference spectrum at 90% and 95% confidence levels respectively.	94
8.4	Global wavelet cross power spectrum between (a) ENSO index and solar irradiance marked in solid blue line, (b)AISM rainfall and solar irradiance in black, (c) ENSO index and sunspot number in orange, (d) AISM rainfall and sunspot in magenta, and (e) ENSO and AISM rainfall in purple. The corresponding dotted lines mark regions where the cross spectrum exceeds the reference spectrum at the confidence levels marked in the same order of colour. The % confidence levels crossed by each of the spectrum are given in the corresponding colours.	94

8.5	8-16 y band averaged wavelet power and cross power between ENSO and HIM, WCI, NWI and CNEI rainfall	95
8.6	8-16 y band averaged wavelet power and cross power between ENSO, and NEI and PENSI rainfall	96
8.7	3-6 y band averaged wavelet power and cross power between ENSO and HIM, WCI, NWI and CNEI rainfall	97
8.8	3-6 y band averaged wavelet power and cross power between ENSO, and NEI and PENSI rainfall	98
8.9	Band averaged wavelet power for ENSO and HIM rainfall and solar irradiance . .	99
8.10	Wavelet cross power for Nino 3.4 with solar irradiance (top panel) and sunspot (bottom panel)	100
8.11	Wavelet cross power for Nino 3.4 with AISM rainfall	100
8.12	Global cross power for Nino 3.4 with AISM rainfall, solar irradiance and sunspot	101
8.13	8-16 y band averaged wavelet power for Nino 3.4 and solar irradiance.	101
8.14	8-16 y band averaged wavelet power for Nino 3.4 and sunspot.	102
8.15	8-16 y band averaged wavelet power for Nino 3.4 and AISM.	102
8.16	Time series for Nino 3.4 tendencies.	103
8.17	Scatter diagram of AISM rainfall against Nino 3.4 tendency time series.	103
8.18	Wavelet Power Spectra for Nino 3.4 tendency (top panel), AISM rainfall (second panel), Sunspot Number (third panel) and Solar Irradiance (bottom panel). . . .	104
8.19	Wavelet Cross Power Spectra of Nino 3.4 tendencies with: Sunspot Number (top panel), Solar Irradiance (second panel), and AISM rainfall(bottom panel).	105
8.20	Wavelet Cross Power Spectra of Nino 3.4 tendencies with: HIM (top panel), WCI (second panel), and NWI rainfall(bottom panel).	106
8.21	Wavelet Cross Power Spectra of Nino 3.4 tendencies with: CNEI (top panel), NEI (second panel), and PENSI rainfall(bottom panel).	107
8.22	Wavelet Cross Power Spectra of Nino 3.4 tendencies with Solar Irradiance (top panel) and AISM rainfall (second panel), and between Solar Irradiance and AISM rainfall(bottom panel).	107
8.23	Wavelet cross power for Nino 3 and Sunspot (top panel) and Nino 3 and AISM (bottom panel).	108
8.24	Wavelet cross power for Nino 3 and Solar Irradiance (top panel) and Nino 3 and Sunspot(bottom panel).	108
8.25	2-7 y (top panel) and 8-16 y (bottom panel) band-averaged wavelet power for Sunspot numbers (SS), Solar Irradiance (IR), ENSO (EN), Nino 3 (N3), Nino 3.4 (N3.4), Nino 3.4 Tendencies (NT), HIM (HI), WCI (WC), AISM (AI) and NEI (NE)	110
8.26	2-7 y(top panel) and 8-18 y (bottom panel) band-averaged wavelet cross power for sunspot numbers-HIM (S-H), Sunspot-NEI (S-N), Irradiance-HIM (I-H), Irradiance-AISM (I-A), ENSO-HIM (E-H), ENSO-NEI (E-N), ENSO-AISM (E-A), Nino 3.4 -HIM (T-H), Nino 3.4 -NEI (T-N), Nino 3.4 -AISM (T-A), ENSO-Sunspot (E-S), ENSO-Irradiance (E-I), Nino 3.4 Tendency-Sunspot (T-S), Nino 3.4 -Irradiance (T-I).	111
9.1	Wavelet transform coefficients of Sunspot Number (absolute values of real part; local scaling; Morlet wavelet; 1440 pts;)	114

9.2	Wavelet transform coefficients of NEI monthly rainfall (absolute values of real part; local scaling; Morlet wavelet; 1440 pts;)	115
9.3	Wavelet transform coefficients of four homogeneous monthly rainfall (absolute values of real part; local scaling; Morlet wavelet; 1440 pts;)	116
9.4	Comparison of NEI and Sunspot number WTC maxima around the 11 year period.	117
9.5	Point process time series of occurrence of WTC maxima in homogeneous rainfall and Sunspot number.	118
9.6	Regression analysis results of NEI and CNEI WTC with sunspot number WTC.	121
9.7	Regression analysis results for HIM and NWI WTC with sunspot WTC.	123
9.8	Regression analysis results for WCI and PENSI WTC with sunspot WTC.	124
9.9	Homogeneous rainfall map of India showing the periods obtained from regression analysis. Band 1: 30-60 y, Band 2: 60-80 y, Band 3: 80-100y, Band 4: 100-122 y	125
9.10	Homogeneous rainfall map of India showing the amplitudes for different period bands obtained from regression analysis. Band 1: 30-60 y, Band 2: 60-80 y, Band 3: 80-100y, Band 4: 100-122 y	126
10.1	Possible Explanation	135

Contents

Acknowledgements	i
Preface	iii
List of Publications	xiii
1 Literature Review	1
1.1 Background History	1
1.2 Solar Activity and Monsoon Rainfall	2
1.3 Studies of data on long term solar-terrestrial climate relationships	5
1.4 Models for Possible Solar-Terrestrial Climate links	6
1.5 ENSO, Monsoon Rainfall and Solar Variability	8
1.6 Studies using wavelet based methods	9
1.7 Present Work	10
2 The Data Analysed	14
2.1 Sources of Data	14
2.1.1 Rainfall	14
2.1.2 Solar Activity	21
2.1.3 ENSO Index	22
2.2 Discussion	23
3 Time Domain Analysis	25
3.1 Introduction	25
3.2 Identifying nonstationarity in time series	25
3.3 Statistical Significance Test	26
3.4 Results	27
3.4.1 Rainfall	27
3.4.2 Results from SST data	28
3.4.3 Five-cycle test period	29
3.5 Conclusions	33
4 Wavelet Power Spectral Analysis	34
4.1 Introduction	34
4.2 Wavelet Power Spectrum	34
4.2.1 Band Averaged Wavelet Power	36
4.3 Results	36
4.4 Power in different period bands	39
4.4.1 Band Averaged Wavelet Power	39
4.5 Conclusion	43

5	Wavelet Cross Spectral Analysis by Torrence-Compo Method	44
5.1	Introduction	44
5.2	Wavelet Cross Power Spectrum	44
5.2.1	Global Wavelet Power Spectrum	45
5.2.2	Torrence-Compo Significance Testing Procedure	45
5.3	Results for monsoon rainfall and solar activity	46
5.4	Results for ENSO index and monsoon rainfall	51
5.5	Results for ENSO index and solar activity	57
5.6	Conclusions	61
6	Wavelet Cross Spectral Analysis Of Rainfall Using Noise Test Signals	64
6.1	Introduction	64
6.2	Data Analysed and Methods Used	65
6.3	Comparison between rainfall and noise cross-spectra	66
6.3.1	Band Averaged Wavelet Cross Power	66
6.4	Results	67
6.5	Conclusions	71
7	Spatial Analysis Of Cross Spectra	75
7.1	Introduction	75
7.2	Results	75
7.2.1	Noise Test Signal Approach	81
7.2.2	Band Averaged Cross Power	88
7.3	Conclusion	89
8	Connection Between ENSO, Indian Rainfall And Solar Activity	90
8.1	Introduction	90
8.2	The data analysed	91
8.3	Wavelet Method of Analysis	91
8.4	Results	91
8.4.1	ENSO - Solar Activity - AISM Rainfall	91
8.4.2	ENSO-MONSOON	95
8.4.3	Results for connections between NINO 3.4, AISM, Solar Activity	99
8.4.4	Results for Connections between Nino 3.4 Tendency, Rainfall and Solar Activity	103
8.4.5	Results for connections between NINO 3, AISM and Solar Activity	108
8.5	Discussion	109
8.6	Conclusions	111
9	Wavelet Maps And Point Process Analysis of WTC Maxima	113
9.1	Introduction	113
9.2	Wavelet Maps	113
9.3	Statistical Analysis of Similarities	119
9.3.1	Regression approach	120
9.3.2	Method Implemented	120
9.4	Discussion	123
9.5	Conclusions	126

10 Conclusions, Explanations and Vistas Ahead	128
10.1 Conclusions	128
10.2 Possible Explanations	133
10.3 Vistas Ahead	135
References	136

Literature Review

1.1 Background History

There is a long history of research seeking and analysing evidence for any possible association between solar processes and terrestrial weather and climate indices. So far studies aimed at unraveling such influences have in general concentrated on searching for relations between indicators of solar activity and terrestrial climate records. On the shorter time scales (less than centuries) these have been in general somewhat sceptically received by much of the meteorological community. There are several reasons for this skepticism: the associations have not always been statistically significant at sufficiently high levels (Burroughs 1992), reliable data using modern instrumentation is available only for a relatively short period of time (of order 10^2 years), correlations attempting to describe sun-weather relations have not been robust in time, and no completely convincing physical mechanisms that may explain links between solar and meteorological processes have yet been established.

The major parameter characterizing solar processes in relation to climate has been connected with sunspots. Sunspots are regions of strong magnetic fields produced by a dynamo process that involves nonlinear interactions between the solar plasma and the magnetic field. It is also believed that the sun has a cycle with twice the period of the sunspots, i.e. 22 y (see Rai Choudhuri (1999)), and some other cycles as well. The sunspot number we refer to in this thesis is the relative sunspot number R often taken as a measure of the spot activity of the sun. This number was introduced by Wolf in 1848. The Wolf sunspot number is defined as $R = K(10g + f)$, where f denotes the total number of spots on the visible disk irrespective of the size, while g denotes the number of spot groups. K is a reduction coefficient that depends on several factors, namely the observer's method of counting the spots and subdividing them into groups, on the size of the telescope used and the magnification employed, as well as on the seeing conditions. The value of $K = 0.60$ is being continuously used at the Zurich Observatory since 1882 to the present day. It is well known that the basic period of the sunspot cycle, defined as the time between successive maxima or minima, is approximately 11 years. According to Waldmeier (1961), the sunspot cycle is not strictly periodic since the time between successive maxima or minima shows considerable variation. He found an average period of 10.9 y with the

fluctuations ranging from 7.3 – 17.1 y when only the intervals between successive maxima are considered. On the other hand an average interval between successive minima turns out to be 11.1 y with the range of variation 9.0 – 13.6 y. A study by Feng *et al.* (1998) over the period 1700-1993 reveals that the sunspot number varies in time with periods between 9 and 15 years, with the majority of the periods occurring within 11 ± 1 years. Besides the 11 year period, the sunspot cycle also exhibits short term variations with a 27-day periodicity due to solar rotation.

With this brief background on the sunspot numbers we take a look at the historical work done so far on the sunspot–rainfall association.

1.2 Solar Activity and Monsoon Rainfall

The earliest studies of possible association between solar activity and Indian monsoon rainfall go back to the pioneering work of Sir Gilbert Walker (1923). In his study on correlations in seasonal variations of weather, he surmised that variations in solar radiation produce variation in seasonal weather over a large part of the earth's surface. A period of increased sunspot numbers not only indicates a period of greater disturbance and general solar activity, but also implies the sun's enhanced magnetic activity. All of these could manifest in a corresponding increase in the heat and light radiated by the sun. Larger sunspots could imply higher solar radiation values. Walker (1923) reports a correlation coefficient of 0.59 (with a probable error of about a tenth of this amount) between 42 monthly mean values of sunspot numbers and the heat radiated during the period 1905–1912. In his view, the three most important meteorological elements to be considered for examining the effect of solar variations on terrestrial weather are temperature, pressure and rainfall. Among these, Walker (1923) studied extensively the effect of sunspots on rainfall over several stations in India as well as other parts of the world. The correlation coefficient of sunspots with the total annual rainfall over the plains of India during the period 1865–1912 was +0.26. Over the 9 Indian stations of Moulmeina, Tezpur, Calcutta, Agra, Rawalpindi, Jacobabad, Bombay, Nagpur and Madras the correlation coefficients of rainfall at the individual stations with sunspots were respectively found to be +0.03, +0.02, –0.03, +0.19, +0.03, +0.14, +0.11, +0.03 and +0.19. From these numbers, Walker concluded that 'the variations in solar activity affect the monsoon as a whole but not the irregularities in the geographical distribution of the rainfall of India as a whole'. Walker (1923) also reports the correlation coefficient of +0.16 between sunspots with variations in the height of water in the Nile river over a period of 131 years from 1749 to 1903; in case of Mississippi the coefficient is –0.08 while for the Caspian Sea and Lake Constance the coefficients are –0.03 and –0.16 respectively.

From such results Walker concludes that 'it would appear that the coefficient of rainfall with sunspots is not in general larger than would be produced by mere chance: for among 100 stations whose rainfall may be regarded as independent the probable value of the largest coefficient is

four times the probable value for a single station. It is only where the coefficients over a region have some appreciable tendency towards uniformity that a real relationship may be concluded. The relationships seem real in the case of Nile and India; but perhaps the clearest case is South America'.

Later studies by Jagannathan and Raghavendra (1964) concluded that the duration of wet spells in the arid and semi-arid regions of Rajasthan are related to sunspot cycle characteristics. In a further study on changes in the pattern of south-west monsoon rainfall distribution over India and its association with sunspots, Jagannathan and Bhalme (1973) used power spectrum analysis and found certain significant periodicities corresponding to the sunspot cycle and its higher harmonics, with regional preferences.

The presence of the quasi-biennial oscillation and the 11-year sunspot cycle in the annual rainfall of India at several stations have been also reported by Jagannathan and Parthasarathy (1973). They used correlation and power spectral analysis of the rainfall distribution in 48 meteorological stations spread all over India. They computed lag-one serial correlation r_1 for each of the rainfall time series and statistically tested their significance using one-tail 95% significance point of the Gaussian distribution. They found that r_1 is positive and also significantly greater than the 95% point for rainfall at only five stations: Trivandrum, Fort Cochin, Akola, Veraval, Sagar and Shillong; at these stations the lag-two (r_2) and lag-three (r_3) serial correlations are equal to or greater than r_1^2 and r_1^3 . A Markov linear-type persistence is indicated at these stations. Although r_1 is positive and significant at Daltonganj, Allahabad and Darjeeling the persistence in those cases is not linear. At Bangalore and Darbhanga, the lag-one correlation is significantly negative, thus indicating the presence of high-frequency oscillations. Jagannathan and Parthasarathy (1973) further made a Mann-Kendall rank statistic test at 95% and 99% confidence level. Here a positive rank statistic value indicates an increasing tendency while a negative value indicates a decreasing tendency. They found a significantly increasing trend at Trivandrum, Fort Cochin, Bellary, Belgaum, Masulipatnam, Bombay, Veraval, Indore and Leh, while Darjeeling and Simla exhibited a significant decreasing trend. Further, in order to understand the above trend they applied a low pass filter to these time series which suppresses the high frequency oscillations; the trend that emerges thereof is not linear but oscillatory comprising periods of more than 10 years. They studied the power spectrum using Tukey's (1950) procedure and found periods close to an 11 year cycle (solar cycle) at five stations, namely Sagar (12.0-14.6 y), Allahabad (7.7-12.0 y), Jodhpur (8.0-12.5 y), Darjeeling (10.1-14.6 y) and New Delhi (10.1-12.0 y) where they are significant to greater than 95%. At Silchar they found a period of 8.8 - 12.0 y at a confidence level greater than 99%.

Coming to more recent work, the detailed periodicity analysis of Indian monsoon rainfall undertaken by Krishna Kumar (1997) did not reveal an 11-year periodicity with greater than 90% significance. However, Krishna Kumar reports a period of 13.3 y in two subdivisions, West Rajasthan and West Madhya Pradesh, at confidence levels of 95% and 90% respectively, using

the Blackman-Tukey (1958) method.

A study of century-scale events in monsoonal climate over the past 24000 years by Sirocko *et al* (1993) presents evidence that the response of the southwest monsoon over the Arabian Sea to long-term gradual changes in insolation are indicative of the rapid changes in local climate induced by the slow solar forcing during the transition from glacial to post-glacial periods. A study of high resolution record of oxygen isotope $\delta^{18}\text{O}$ variations in Th-U-dated stalagmite from Oman for the period 9.6–6.1 ky before present, which serves as a proxy for variations in tropical circulation and monsoon rainfall, has been recently reported by Neff *et al* (2001). Excellent correlations between records of $\delta^{18}\text{O}$ and $\Delta^{14}\text{C}$ from tree rings, which reflect changes in solar activity, suggests that one of the primary controls on centennial to decadal scale changes in tropical rainfall and monsoon intensity is variation in solar radiation. Thus Neff *et al.* establish a strong coherence between solar variability and the monsoon in Oman in the period 9–6 ky ago.

Agnihotri *et al.* (2002) demonstrated solar influence on the intensity of the Indian monsoon using proxy data of surface productivity and continental run-off of sediment core 2502G (21.8° N 68° E, dating back to approximately 1200 years) from the northeastern Arabian Sea. They found that the intensity of the Indian monsoon decreased during periods of solar minima of the last millennium. Reconstructed monsoon intensity variations inferred from the varve thickness data (obtained from a sediment core off Pakistan) exhibited a pattern matching fairly that of reconstructed total solar irradiance during the last millennium,– thus reinforcing their conclusion on solar influence on the monsoons in India. Furthermore, a spectral analysis performed by them revealed significant periodicities of 200, 110, 70 and 55 years in proxy data of Indian monsoon intensity, while the total solar irradiance data revealed significant periodicities of 194, 113, 77 and 53 years. The cycles of monsoon activity were thus attributed to solar forcing in their work. Another study by Agnihotri and Dutta (2003), subjecting all India summer monsoon rainfall over the period 1813–1994 to a 20 year running average, revealed a prominent 60 y period which is close to the 55 y cycle present in monsoonal proxies of the northeastern Arabian Sea, which in turn could be driven by solar variability. Their study on centennial scale variations in Indian, east equatorial and Chinese monsoonal rainfall reveals that precipitation systems over these regions resonate with short-term/multi-decadal solar frequencies, although the amount of total rainfall in different regions may be different depending on their local geographic conditions.

More recently, Kodera (2004), using a modern meteorological dataset for the period 1958–1999, confirms the results obtained by Neff *et al* (2001). Kodera's analysis suggests that the solar influence on Indian monsoon activity originates from the stratosphere through modulation of the upwelling in the equatorial troposphere, which provides a north-south seesaw of convective activity over the Indian ocean sector during summer. This in turn leads to higher precipitation over Arabia and India during periods of higher solar activity. Kodera believes that the solar influence on monsoon activity is not due to a change in radiative heating in the troposphere.

Stager (2005) provides evidence from Lakes Naivasha and Victoria in Africa that suggests that prolonged sunspot minima caused lake levels to rise there during the Little Ice Age. He puts forth the hypothesis that solar cooling could have caused symmetrical equatorward shrinking of the tropical rain belts, thus increasing rainfall in equatorial Africa while causing droughts at higher tropical latitudes. Van Loon (2005) reports a probable influence of the decadal solar oscillation in the Pacific ocean, expressing itself in a weakening of the Aleutian low, stronger trade winds across the equator, lower sea-surface temperatures and rainfall in the equatorial belt and higher rainfall in the inter-tropical convergence zone (ITCZ) and south Pacific convergence zone (SPCZ).

1.3 Studies of data on long term solar-terrestrial climate relationships

A brief review of the work reported in this field in the last 15 years is presented in this section.

A study by Beer *et al* (1990) regarding the use of ^{10}Be in polar ice to trace the 11-year cycle of solar activity opened up the possibility of studying the long-term behaviour of solar activity and the history of solar-terrestrial relationships. Friis-Christensen and Lassen (1991) showed the existence of a high correlation between the variation of the length of solar cycles and of northern hemisphere terrestrial temperature for the period 1861 to 1989. They suggested that shorter solar cycles accompany higher solar activity and vice versa. The independent determination of the cycle length based on the intervals between the maxima of the sunspot numbers is consistent with that obtained using the minima of the sunspot numbers. This indicates that the sunspot cycle length may provide with a physically meaningful index of solar activity. It was also found that the long term variation of the global temperature in the form of an index of the North Atlantic sea ice shows that each of the maxima in long term solar activity occurring around 1770, 1850 and 1940 has been accompanied by a corresponding minimum in the 22 year running mean value of the extent of sea ice around Iceland. Kelly and Wigley (1990) in their work argued that a change in the solar constant is unlikely to account for more than a small fraction of the observed warming in global mean surface temperature since the mid-19th century, as their results suggest that the influence of enhanced greenhouse effect on global mean temperature has dominated over the direct influence of solar variability since the mid-19th century. But Friis-Christensen and Lassen (1991) seem to suggest that the net increase of the Northern Hemisphere temperature during the last 130 years might be partly attributed to the increased greenhouse effect, but that departure from the long term behaviour during 1940-1970, when the temperature decreased, may be partly due to the decrease in solar activity during that period as indicated by the variation in the length of the solar cycle. However, more recently, a criticism of the above conclusions of Friis-Christensen and Lassen (1991), due to Damon and Laut (2005), suggests

that the otherwise strong agreement between the solar curve and terrestrial temperatures during the global warming of the recent decennia might well be an artifact of adding, to a heavily smoothed/filtered curve, four additional points (which were only partially filtered) covering the period of recent global warming.

1.4 Models for Possible Solar-Terrestrial Climate links

Although the basic causes underlying any relationship between solar processes and terrestrial climate still remain unclear, some plausible mechanisms are now beginning to emerge.

The nature of the problem may be illustrated by noting that, while monitoring of the total solar irradiance by satellites over a period of about two decades has confirmed that there is an 11-year variation in electromagnetic radiation, the magnitude of this perturbation in flux is of order 2 W/sq m , i.e. a few tenths of one per cent of the total, which is 1350 W/sq m (Willson and Hudson 1988; Lee *et al.* 1995). A change of this order has been estimated to cause the global mean surface temperature of the earth to change by about 0.1°K . It has been found that for a significant atmospheric response this would have to be enhanced by a factor of between 3 and 10 (Wigley and Raper 1990). The mechanisms by which such amplification can occur are not yet understood, but they could be dynamical or chemical. One clue is that, while the radiation in the visible and infrared part of the spectrum remains relatively stable, changes in the ultraviolet, X-ray and radio wavelengths can be huge (two to three orders of magnitude). A plausible mechanism would thus operate through chemical effects in the stratosphere and a dynamical coupling thereto with the troposphere, e.g. through ozone or through effects on stratospheric zonal winds and vertically propagating planetary waves.

To study the impact of solar variability on climate, Haigh (1996, 1999) constructed a general circulation model to simulate changes in solar irradiance and stratospheric ozone in order to investigate the response of the atmosphere to the 11-year solar activity cycle. Her results show that solar-induced increases in stratospheric ozone and lower stratospheric temperatures, occurring in response to enhanced solar irradiance, result in stronger summer easterly winds, which penetrate into the tropical upper troposphere and force tropospheric circulation patterns poleward. These changes can influence subsequent climate response. This reasoning is reinforced by the discovery of the signal of the 11-year sunspot cycle in the upper troposphere-lower stratosphere, reported by Labitzke and Van Loon (1997), who further analysed their results using GCM models (see Labitzke *et al.* (2002)). The correlations between stratospheric constant pressure levels (at least as high as 25 km) and the solar cycle show a consistent pattern, with highest correlations in the subtropics. The variation of stratospheric heights in phase with the sunspot cycle is associated with temperature variations on the same time scale in the middle and upper troposphere. The spatial distribution of the correlations indicates that year-to-year changes in tropical and subtropical vertical motions contain a component on the time scale of the

solar cycle. Furthermore, the correlations between the total ozone column and the sunspot cycle are found to be lowest in the equatorial regions where ozone is produced, and in the subpolar regions where the largest amounts are found. Such characteristics of the spatial distribution of correlations may be attributed to the fact that the subtropical heights of the constant-pressure surfaces in the ozone layer are higher in the maximum than in the minimum years of the sunspot cycle. Higher subtropical heights during solar maxima depress the poleward transport of ozone through the subtropics and thus create an abundance of ozone.

Kodera (2005) studies the solar influence on the troposphere through stratospheric dynamical processes. He suggests that small zonal wind anomalies in the subtropics during the winter hemisphere could be produced by changes in the ozone heating rate. This in turn could be amplified through interaction with planetary waves propagating from the troposphere. Solar effects can be dynamically transmitted to the troposphere in two ways: (a) poleward and downward shift of the westerly jet through interaction with planetary waves and the wave reflection, and (b) the modulation of the mean meridional circulation. The former could explain the solar influence on the North Atlantic Oscillation while the latter could explain the solar effect on the monsoonal rainfall and El Niño.

Ruzmaikin and Feynman (2002) report the influence of solar variability on the major mode of Northern Hemisphere variability, the North Annular Mode. A later study by Ruzmaikin (2005), using empirical orthogonal decomposition, reveals that the Northern Hemisphere variability and the Nile river basin variability are closely related to solar variability.

Shindell *et al.* (2001) studied the solar forcing of regional climate change during the Maunder minimum using the general circulation model (GCM) of the Goddard Institute of Space Studies (GISS). Their results provide evidence that relatively small solar forcing may play a significant role in century-scale northern hemisphere (NH) winter climate change. In fact Shindell *et al.* (2005) incorporate, into their latest GISS model E/III, the relative contribution of chemistry and transport to ozone changes in the tropopause region, and unravel their key role in altering the dynamics via changing the meridional temperature gradient in that region. Their new model captures the historical patterns of the climate response to long-term solar irradiance changes in an improved way.

A model involving combination of solar cycle length and green house forcing could explain many features of the global mean surface air temperature, as outlined by Kelly and Wigley (1992). In another study by Lassen and Friis-Christensen (1995), an extension of the cycle length record into the more distant past using a combination of sunspot number and auroral observations revealed a strong correlation between the variation in the period of the sunspot cycle and indicators of climate, like long-term variations in global temperature.

While such mechanisms cannot be said to have been understood at a level where we are confident about the causes of a significant link between solar processes and tropical weather, it is now also well known that in a nonlinear system small changes in input are capable of causing

relatively large changes in the output. At the present stage, therefore, the results described in this thesis, showing strong connections between monsoon rainfall and sunspot parameters, must be seen as empirical facts that demand further work on possible physical, dynamical and chemical mechanisms responsible for the present observations.

1.5 ENSO, Monsoon Rainfall and Solar Variability

There have been extensive studies of the ENSO phenomenon in recent decades. El Nino is said to occur if 5-month running means of sea surface temperature (SST) anomalies in the Nino 3.4 region (5° N -5° S, 120° - 170° W) exceed 0.4° C for 6 months or more (see Trenberth 1997). Although El Nino initially meant an annual weak warm current that ran southward along the coast of Peru and Equador during the Christmas time, subsequently it became associated with the unusually large warmings that recur every few years and in turn change the local and regional ecology there. This coastal warming often gives way to anomalous warming extending till the International date line in the Pacific ocean. It is this Pacific basinwide phenomenon that influences global climate patterns. The atmospheric component linked to El Nino is called the 'Southern Oscillation', and scientists refer to the phenomenon where both the atmosphere and ocean collaborate together as ENSO, an abbreviation for 'El Nino - Southern Oscillation'.

Studies on what is now called ENSO date back to Sir Gilbert Walker's remarkable work in the early 1900s. His search for inter-relationships between contemporary and antecedent meteorological phenomena in several parts of the world, using basic correlation techniques, confirmed a see-saw connection between the pressure at Azore and Iceland and a similar variation in the North Pacific Ocean. From his studies, even the other sympathetic oscillations appeared to be a phenomenon on a much larger scale, which he called the 'Southern Oscillation'. Walker defines the 'Southern Oscillation' as a tendency for air to be removed from the Pacific area as air accumulates in and around the Indian ocean and vice-versa. Walker conjectured that the symptoms of the southern oscillation are not confined to pressure but are also evident in the rainfall of India, Java and Australia, as well as some air temperature records over selected areas. He further concluded that these oscillations do not have regular periodicity, nor do they form the dominant part of the variance of the elements at any place. Nevertheless they could be related to but not controlled by sunspots. Walker thought that 'They are systematic swaying of interconnected world conditions which is intensified or checked by solar changes'.

A large number of studies on ENSO (see Walker and Bliss 1937, Normand 1953, Torrence and Webster 1998) and its connection with the Indian monsoon rainfall have been reported in recent decades (see Normand 1953, Troup 1965, Meehl 1987, Yasunari 1990, and Torrence and Webster 1999). In particular, Torrence and Webster (1999) show that ENSO and Indian monsoon rainfall exhibit interdecadal changes in variance and coherency over the period 1871-1996. Their study revealed that during intervals of high ENSO variance (1875-1920 and 1960-1990), the annual-

cycle variance is lower than average in all India rainfall, and conversely, during the interval 1920-1960 of low ENSO variance, there is higher than average annual cycle variance in all India rainfall. Such an inverse relationship also appears at the 12-20 y timescale particularly during 1875-1910.

Incidentally, in some recent work, Krishna Kumar *et al.* (1999) examined the weakening of the inverse relationship between the Indian Monsoon and ENSO in the light of global warming. The decreasing correlation between ENSO and Indian monsoon rainfall during the last decade might be a typical epoch of the ENSO/Monsoon system as suggested by the findings of Maraun and Kurth (2005). According to them there exist epochs of phase coherence between ENSO and Indian monsoon rainfall. Attempts have also been made to study the interconnections of ENSO (see Mendoza *et al.* 1991) and global sea surface temperatures (see Reid and Gage 1991, Reid 1991) with sunspot numbers. More recently, a study concerning prediction of Indian rainfall index using the ENSO and sunspot cycles have been reported employing an artificial neural network approach (see Srilakshmi *et al.* 2003).

A recent study by Mehta and Lau (1997) shows that while solar irradiance and monsoon co-vary with nearly the same phase, the solar irradiance and Nino 3 SST seem to vary with opposite phases on multi-decadal time-scales. It may be noted that in their study, 42% and 30% of the total solar irradiance variance were explained by the multi-decadal and 11-year irradiance components respectively. Furthermore, their study also suggests the possibility that the multi-decadal irradiance component influences the monsoon more than the 11 year component.

Precise solar irradiance measurements have only been made since 1978, whereas a much longer data stretch is required to establish long-term relationships with climate. In order to reconstruct solar irradiance over a longer stretch of time using historical records of solar activity indicators, several models have been suggested, see for instance Foukal and Lean (1990), Lean *et al.* (1995), Solanki and Fligge (1999) and Lean *et al.* (2002). However, there emerges no consensus in all these studies as to what could be the best model to reconstruct irradiance variations. According to Foukal and Wigley (2004), the solar irradiance reconstructions used so far in the climate models could even be a factor of 5 larger than can be explained. While this could largely affect the physics of the problem, for the present work it is the *pattern* of the solar irradiance time series that is more relevant, and we use the standardised solar irradiance data of Lean (2004) for this purpose.

1.6 Studies using wavelet based methods

With the advent of wavelet transform analysis as a tool well suited to the study of multiscale, nonstationary processes over finite spatial and temporal domains, there has been a recent surge in interest in incorporating such techniques for climate signal detection and analysis, as can be seen in the works of Weng and Lau (1994), Lau and Weng (1995), Torrence and Compo (1998),

Torrence and Webster (1998, 1999), Kailas and Narasimha (2000), Kulkarni (2000), Narasimha and Kailas (2001), and more recently in the works of Anderson and Woodhouse (2005). The use of the continuous wavelet transform in a study by Fligge *et al* (1999), using several indicators of solar activity like sunspot number, sunspot area, plage area or ^{10}Be records, reveals variations in the length of the solar cycle which are in agreement with the results originally published by Friis-Christensen and Lassen (1991).

In a recent study by Kailas and Narasimha (2000) and Narasimha and Kailas (2001), wavelet analysis of rainfall over the homogeneous Indian Monsoon area for the period 1870-1990 revealed a set of modes in the rainfall time series characterised by jittery oscillations or quasi-cycles with approximate average periods of 3.0, 5.8, 11.6, 20.8, 37 and 80 years. Indeed the quasi-cycle of period 11.6 years in the monsoon rainfall seems to correspond to the length of the 11-year solar cycle as reported in most of the above mentioned studies.

1.7 Present Work

In the light of the above brief review of the present state of solar-climate studies we revisit in this thesis the specific problem of possible links between Indian monsoon rainfall and solar processes. A major feature of the present work is the use of direct records of monsoon rainfall (rather than proxies), and the extensive use of different wavelet techniques. The idea that the tropics can amplify a small radiant flux signal to a relatively large and dynamic climate change (Haigh 2001, 2004, 2005), Visser 2003) in the tropics as well as elsewhere in the world, serves to provide motivation for the present work. The main objective here is to investigate possible connections between solar activity, Indian monsoon rainfall and the El-Nino southern oscillation (ENSO) indices, using different methods of time series analysis.

A detailed description of all the rainfall, solar activity as well as ENSO indices analyzed in this study is presented in chapter 2. The rainfall indices selected for study are Indian monsoon rainfall over the five different homogeneous rainfall regions identified by Parthasarathy *et al.* (1993), the homogeneous Indian monsoon (HIM) rainfall, and the all India summer monsoon rainfall (AISMR). We also look at the annual rainfall from each of 29 meteorological subdivisions in India. It must incidentally be stressed that the often-used AISMR is not the best rainfall index for analyses like the present, as the geographical area it covers is not meteorologically homogeneous, and so physically coherent signals will tend to get diluted due to heterogeneity. This point will be illustrated across many of the chapters through various analyses. The solar indices under study are the annual sunspot numbers, group sunspot numbers and the solar irradiance. The ENSO indices under consideration are the global ENSO index, the Nino3.4 SST and the Nino3 SST.

A time domain analysis of all the above-mentioned data is performed and the results are reported in chapter 3 of the thesis. Over the 120 y period (1871–1990) for which reliable Indian

rainfall statistics are available, solar activity parameters exhibit nonstationarity. Taking this fact into account, we present here the results of an analysis of four solar activity indices and seven major Indian monsoon rainfall time series. Statistics are compared over two distinct test periods respectively of low and high solar activity, each comprising three complete solar cycles. It is found that the average rainfall is higher in all seven rainfall indices during periods of greater solar activity, at confidence levels varying from 75% to 99%, being 95% or greater in three of them.

Chapter 4 presents a simple wavelet analysis of the rainfall, solar and ENSO data. It is found from this analysis that the power in the 8–16 y band during the period of higher solar activity is higher in 6 of the 7 rainfall time series, at confidence levels exceeding 99.99% in all six cases. These results, together with those of the time domain analysis, support existence of connections between Indian rainfall and solar activity.

Next, we present a wavelet cross-spectral analysis of solar activity and homogeneous Indian monsoon rainfall in chapter 5. First we define the wavelet cross power spectrum in mathematical terms and describe the statistical test for significance that we use in the analysis. The cross spectrum results for rainfall-solar activity, ENSO-rainfall as well as ENSO-solar activity are described in this chapter in detail. The statistical significance of the computed cross-spectrum is first estimated from the procedure proposed by Torrence and Compo (1998). It will be shown that this procedure suggests very high significance levels. This is traced to the use of a reference spectrum which utilises lag-1 and lag-2 auto-correlations of the signals being analysed. When one of these (solar activity in the present case) has a strong periodic component the test is misleading, as is easily demonstrated by replacing rainfall with white noise time series.

Chapter 6 presents a new procedure that is proposed here to overcome the above mentioned limitation of the Torrence - Compo procedure. The principle behind the new procedure is to compare the cross spectrum under question with that between solar activity and three specially generated noise signals, one white and the other two simulating respectively the frequency spectrum and amplitude distribution of rainfall. As is evident, this procedure is in part of the Monte Carlo type. The difference in solar-rainfall and solar-noise cross spectra can then be subjected to standard statistical tests to assess significance. It is found that over the two test-periods respectively of high and low solar activity, each comprising three complete solar cycles, as already defined in Chapter 3, the average cross power of the solar activity index with rainfall exceeds that with the noise at z -test confidence levels exceeding 99.99% over period-bands covering the 11.6 y sunspot cycle. These results provide strong additional evidence for connections between Indian rainfall and solar activity.

Having studied the cross-spectrum between the three test signals and sunspots for the case of HIM rainfall, we now perform this analysis for all the other homogeneous zone rainfall time series in India, so as to learn more not only about the temporal but also the spatial variations between the different homogeneous regions. The details of this spatial analysis are reported

in chapter 7. For each of the homogeneous regions, we first simulate ensembles of three kinds of test signal, namely, white noise (WN), a noise simulating the rainfall spectrum (SN) and a noise simulating the amplitude probability distribution (AN) of the rainfall time series under consideration. Next we compute the ensembles of cross spectrum of the sunspot number time series with each of these test signals and study the differences between them and that between the original rainfall and sunspot numbers. From the graphs displayed in this chapter, it is clear that the results from for West Central India (WCI), North West India (NWI) and AISMR are similar in nature, while North East India (NEI) is distinctly different from all of them. Central North East India (CNEI) and Peninsular India (PENSI) have characteristic features that are in between those of WCI and NEI.

Even over the slightly longer period of 1850-1998 over which an all India summer monsoon rainfall has been reconstructed, statistical time series analysis reveals significant influence by sunspots and solar irradiance, particularly over the two test-periods defined earlier. Evidence presented in chapter 8 shows that connections of ENSO with these solar process parameters are stronger than those between ENSO and summer monsoon rainfall. A continuous Morlet wavelet transform applied to these data further confirms the above conclusion. The global wavelet cross spectra between solar irradiance and monsoon rainfall, and those between irradiance and the ENSO index, show significant power around the period of the 11 year solar cycle, passing the chi-squared test of significance proposed by Torrence and Compo (1998) at levels exceeding 95% and 97.5% respectively. The global wavelet cross power spectra between the ENSO index and the all India summer monsoon rainfall show a peak in the 3-4 year period range at significance levels of 70%. Similar relations are also found between sunspot numbers and ENSO, and between sunspot numbers and monsoon rainfall. Two distinct epochs are found in the computed cross-spectrum showing that the average rainfall is higher when average ENSO index is lower. These epochs coincide with periods of greater and lower solar activity; the z -test confidence levels for the connections exceed 95%. This shows that there is a stronger connection between ENSO and solar activity as compared to the ENSO-rainfall connection. Greater solar activity is associated with lower ENSO activity and vice-versa, supporting the well-known inverse relationship between ENSO and rainfall. More importantly, this finding suggests that Indian rainfall is affected by solar processes indirectly through ENSO.

The problem of the existence of possible correlations between the solar cycle period as extracted from the yearly means of sunspot numbers and any periodicities that may be present in the Indian monsoon rainfall has been addressed using a new technique involving wavelet analysis in chapter 9. The wavelet transform coefficient maps of sunspot-number time series and those of the homogeneous Indian monsoon rainfall annual time series reveal striking similarities, especially around the 11-year period. A novel method to analyse and quantify this similarity devising statistical schemes is suggested in this chapter. The wavelet transform coefficient maxima around the 11-year period for the sunspot numbers and the monsoon rainfall have each

been modelled as a point process in time, and a statistical scheme for identifying a trend or dependence between the two processes has been devised. A regression analysis of parameters in these processes reveals a nearly linear trend with small but systematic deviations from the regressed line. Suitable function models for these deviations have been obtained through an unconstrained error minimisation scheme. These models provide an excellent fit to the time series of the given wavelet transform coefficient maxima obtained from actual data. Statistical significance tests on residual deviations suggest with 99% confidence that the deviations are sample fluctuations obtained from normal distributions.

In chapter 10 we summarise all the results obtained and conclude that, over durations of a few decades, Indian monsoon rainfall increases in periods of higher solar activity and decreases in periods of lower solar activity. However this effect has a distinct spatial variation spread across the country as a whole. ENSO indices follow an inverse relationship with solar activity and there are spatial variations in the ENSO-monsoon relationship as well. Chapter 10 also examines possible explanations for the results obtained and suggests a schematic model for the complex dynamics underlying associated atmospheric processes, and discusses new vistas for further investigations in future.

The Data Analysed

2.1 Sources of Data

The present analysis involves monsoon rainfall, solar and ENSO indices for the period 1870–1990 spanning 120 years. The rainfall indices have been obtained from Parthasarathy *et al* (1995). The solar data have been mainly obtained from the NOAA site <ftp://ftp.ngdc.noaa.gov/STP/SOLAR.DATA>, while the data for Global SST ENSO index have been obtained from the website <http://jisao.washington.edu/data/globalssstenso/>. A more detailed description of these data sets follows in the sections below.

2.1.1 Rainfall

The rainfall data from Parthasarathy *et al.* (1995) are also available as IITM-IMR data set at the Indian Institute of Tropical Meteorology website. The details about how these data were procured and pre-processed are as follows.

A network of 306 almost uniformly distributed rain-gauge stations, each providing one representative station per district having a reliable record since 1871, was considered for the creation of the data set. The four meteorological subdivisions of hilly regions of India parallel to the Himalayan mountain range were excluded from the study since dearth of an adequate rain-gauge network in the region leads to low areal representation. Also excluded from Parthasarathy's network of rain-gauges are the two island subdivisions (Lakshwadeep and Andaman/Nicobar) which are far away from the mainland. The contiguous area with the network of 306 stations spans 29 meteorological subdivisions of India and covers about 2,880,000 sq.km., which is about 90 percent of the total area of the country. The subdivisional/regional rainfall series provide monthly (January - December) area-weighted rainfall data for each of the 29 meteorological subdivisions of India (out of a total of 35), and were obtained by assigning the district area as the weight for each rain-gauge station in that subdivision. Furthermore, assigning the subdivision area as the weight to each of the subdivisions in the region, the area-weighted monthly rainfall series have been obtained for various homogeneous regions of India as well as for India as a whole.

For much of the present analysis, seven annual area-weighted rainfall time series for the period

1871-1990 have been considered, namely the all India summer monsoon rainfall (AISMR), and the north east India (NEI), north west India (NWI), central north east India (CNEI), west central India (WCI), peninsular India (PENSI) and the homogeneous Indian monsoon (HIM) rainfall. Of these, the last 6 are indicative of monsoon rainfall over the broad meteorologically homogeneous regions in India as defined by Parthasarathy *et al.* (1995). The choice of these 6 regions was based primarily on a considerable degree of spatial coherence. The HIM region covers the central and north-western parts of India amounting to 55% of the total land area of the country, and is considered to be by far the most characteristic index of the component of Indian rainfall dominated by the dynamics of the south west monsoon. It is well known that the NEI region shows in many ways an anti-correlation with the HIM region (Parthasarathy *et al.* 1993).

It may be noted that although rainfall data are available for the period 1871-2003, data for the later period 1991-2003 are preliminary estimates based on the subdivisional means supplied by the India Meteorological Department (IMD), which are in turn based on a variable network. Although the IMD data have been rescaled to conform to the long-term means of the respective subdivisions in the IITM-IMR data set, the full set of data for 306 stations are yet to be updated. We therefore select for our analysis the period 1871-1990, for which proper data from these 306 stations are available.

Furthermore, we consider the rainfall time series from each of the 29 meteorological subdivisions in India, the raw data for which are obtained from the Indian Institute of Tropical Meteorology, Pune. Two maps showing all the meteorological subdivisions and the 6 homogeneous regions are shown in figures 2.1 and 2.2 respectively. The raw data for rainfall from the 6 homogeneous regions are displayed in figure 2.3. Figures 2.4, 2.5 and 2.6 show the rainfall time series from all the meteorological subdivisions.

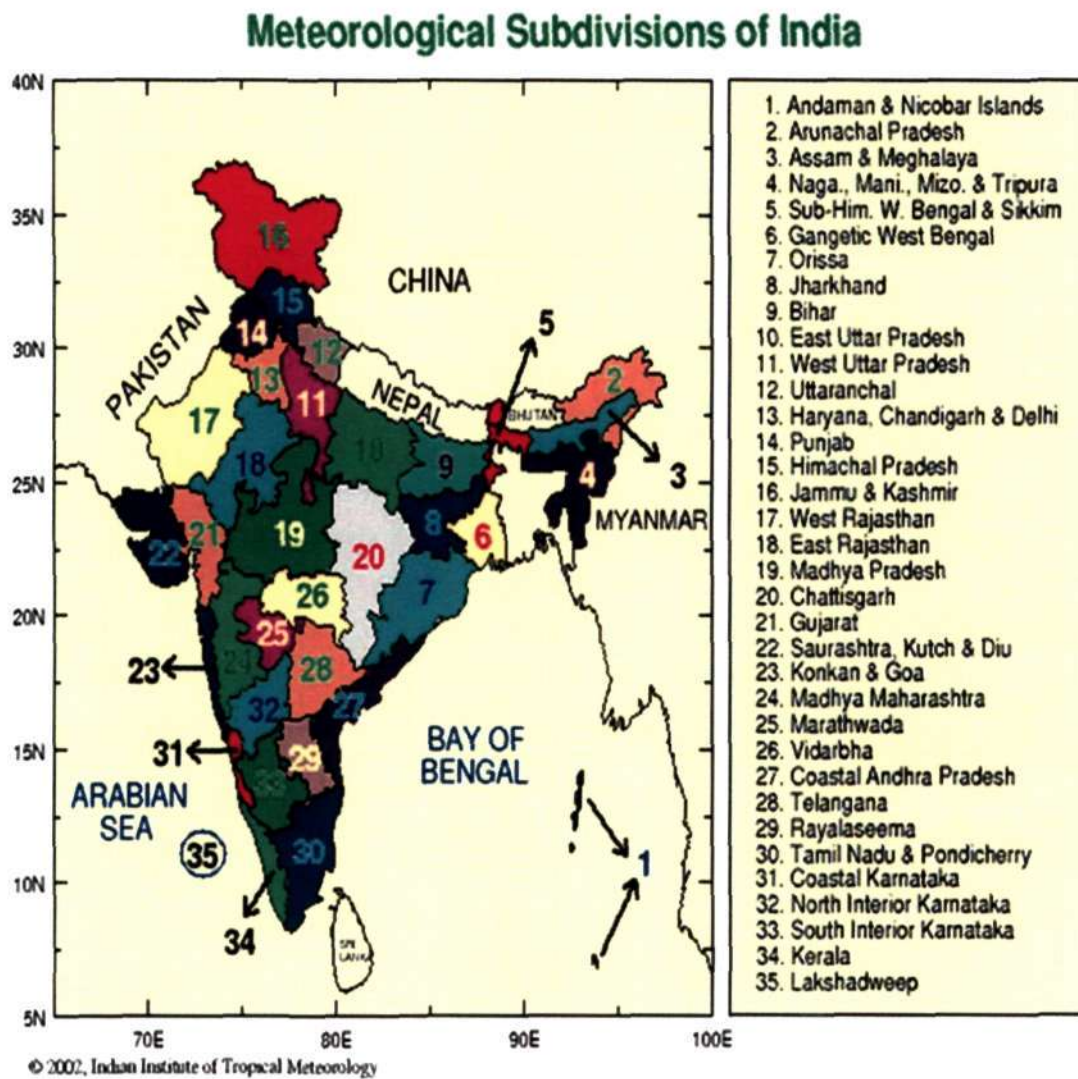


Figure 2.1. Map of sub divisions

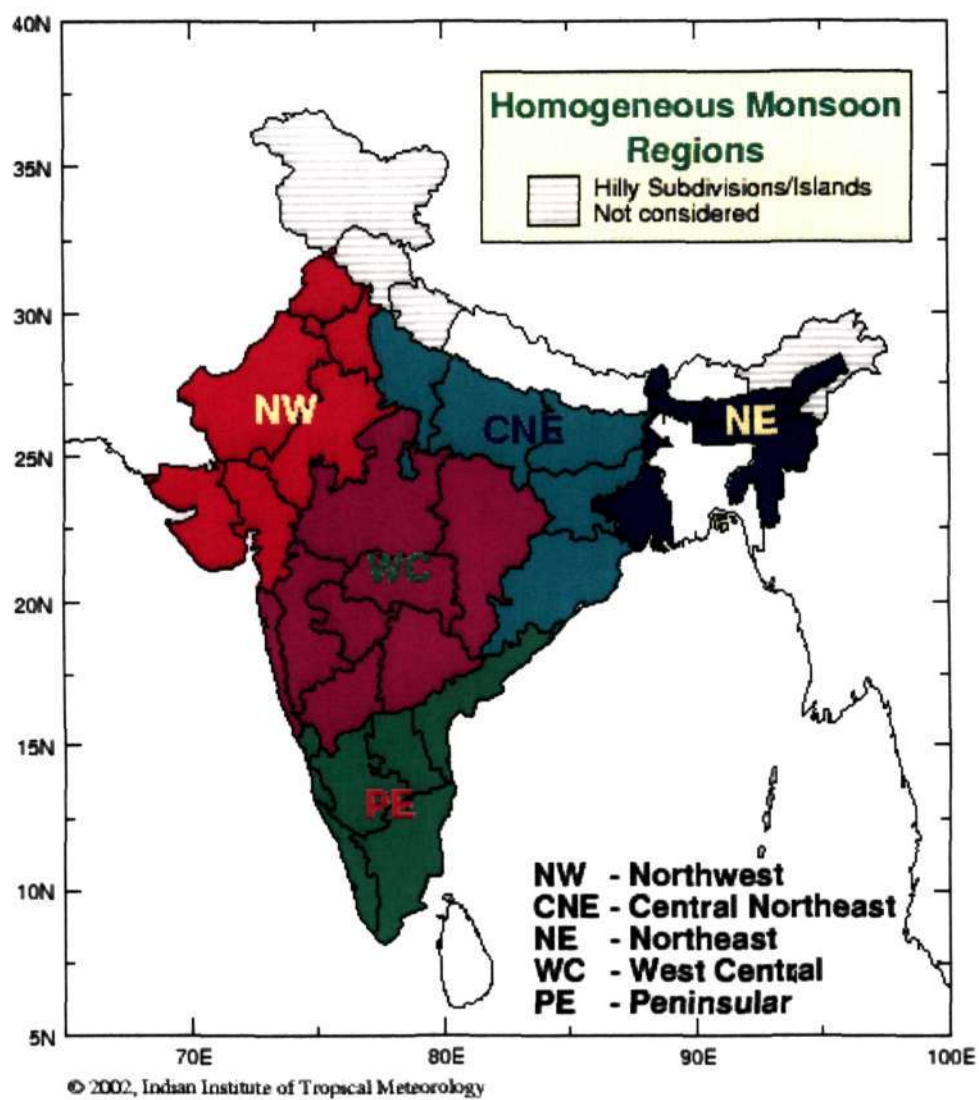


Figure 2.2. Map of homogeneous regions

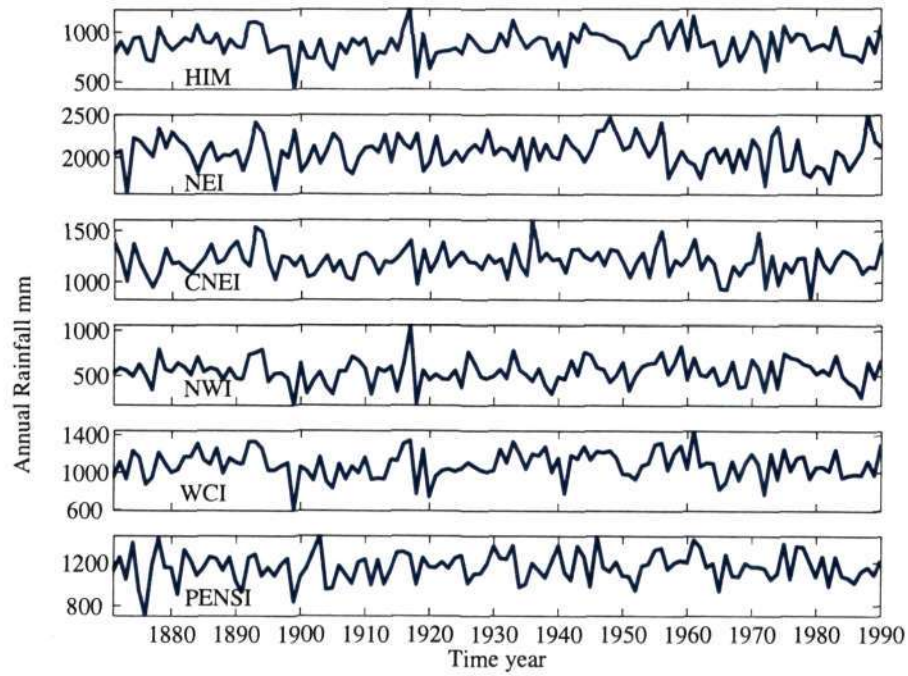


Figure 2.3. Rainfall time series of 6 homogeneous regions

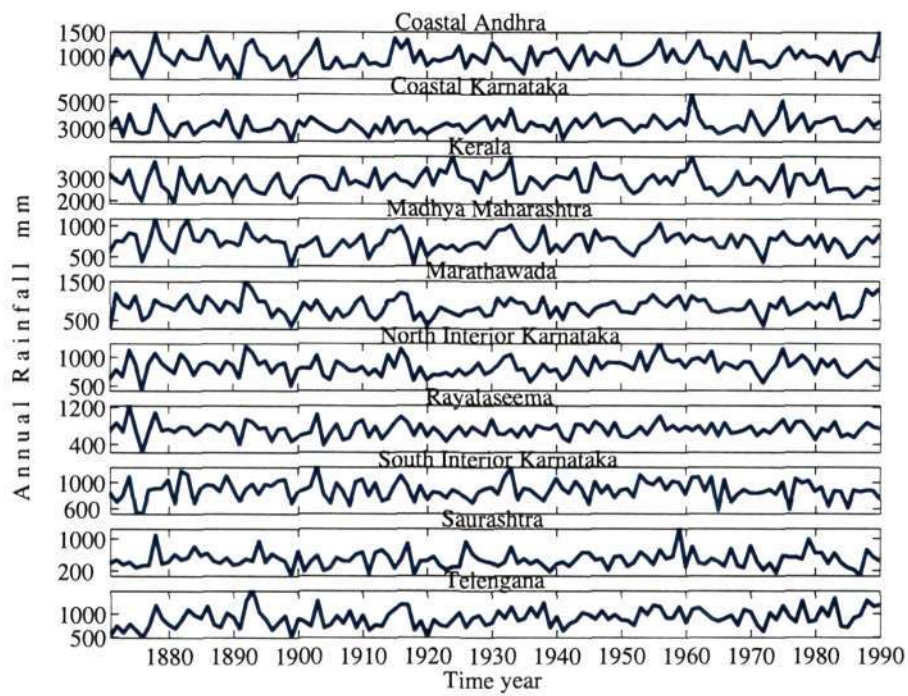


Figure 2.4. Rainfall time series of 10 subdivisions.

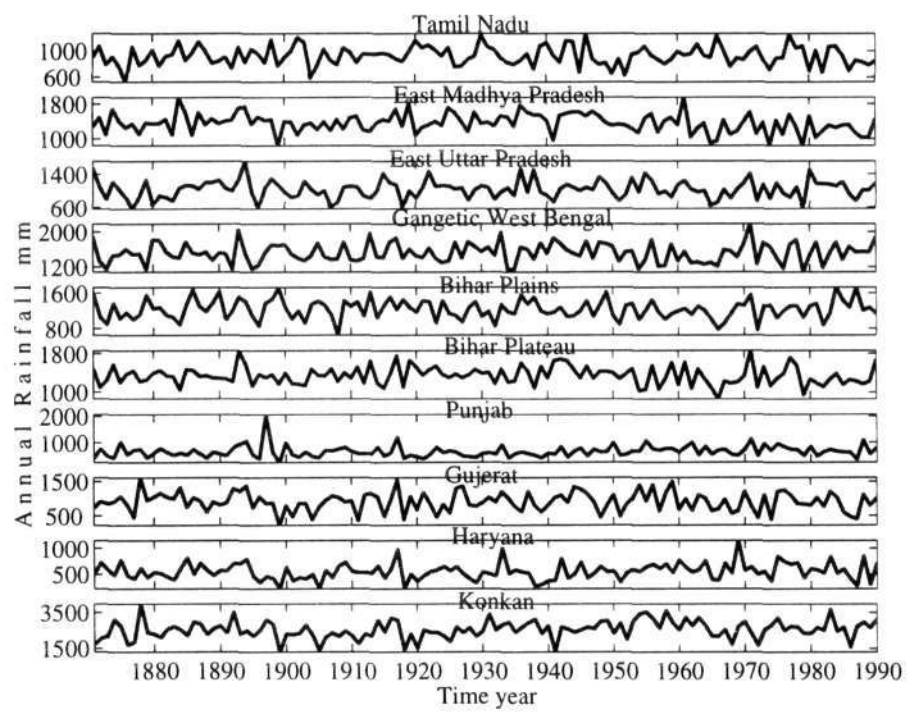


Figure 2.5. Rainfall time series of next 10 subdivisions.

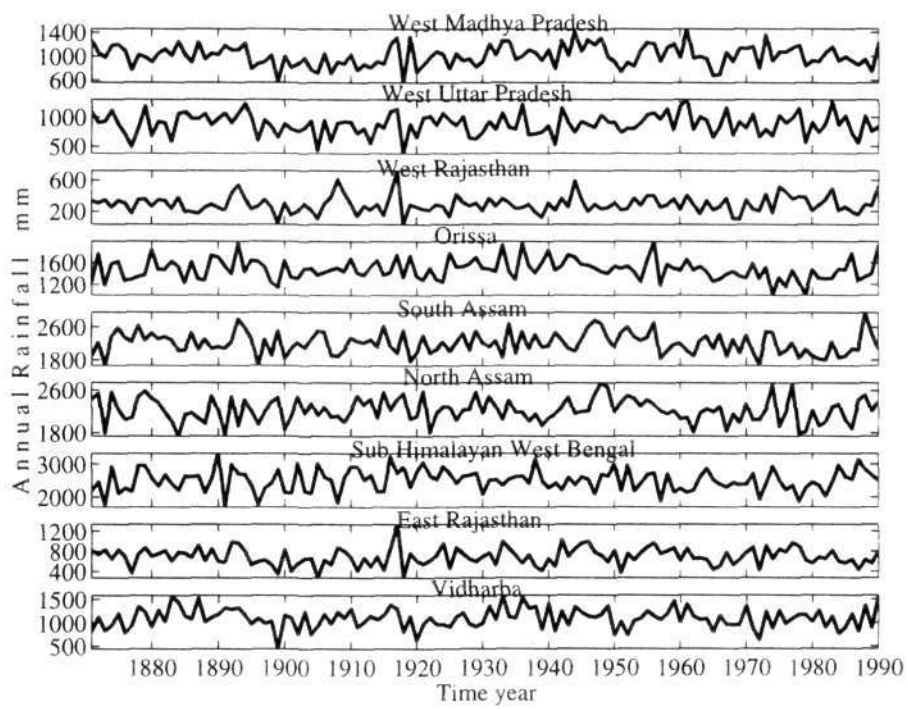


Figure 2.6. Rainfall time series of next 9 subdivisions.

2.1.2 Solar Activity

The solar indices under study are sunspot number, group sunspot number and solar irradiance. Sunspot areas have also been studied, but have been found to provide no new information. The sunspot index data have been obtained from Rai Choudhuri (1999) and Fligge *et al.* (1999), and the data for group sunspot number from the NOAA site <ftp://ftp.ngdc.noaa.gov/STP/SOLAR.DATA>. Since individual sunspots live typically for several days, sunspot data (unlike rainfall) are not cumulative. All monthly data on sunspots are usually compiled by taking averages of daily data over a month. The monthly average sunspot number plotted against time does not appear very smooth (see, for example, the website <http://science.msfc.nasa.gov/ssl/pad/solar/image/zurich.gif>). Figure 2.7 displays a time series of the monthly sunspot number which shows a lot of jitter as compared to the annual solar activity data shown in figure 2.8.

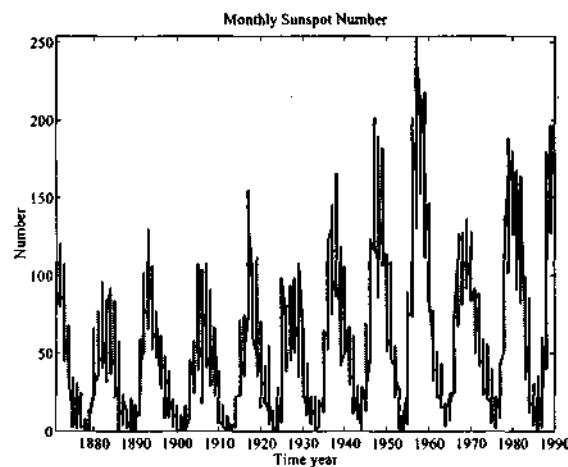


Figure 2.7. Solar Activity Time Series.

The data for the time series of annual mean solar irradiance has been obtained from Lean (2004) (see also Lean *et al.*, 1995), available at the online resource of the World Paleoclimate Data Center website: ftp://ftp.ncdc.noaa.gov/pub/data/paleo/climate_forcing/solar_variability/lean_20_irradiance.txt. Precise solar irradiance measurements have only been made since 1978, whereas a much longer data stretch is required to establish a long term relationship with climate. In order to reconstruct solar irradiance over a longer stretch of time using historical records of other solar activity indicators, several models have been suggested, see for instance Foukal and Lean (1990), Lean *et al.* (1995), Solanki and Fligge (1999), Lean *et al.* (2002) and Foukal and Wigley (2004). However, out of all these studies, no consensus has yet emerged as to what could be the best model to reconstruct irradiance variations. According to Foukal and Wigley (2004), the solar irradiance reconstructions used so far in the climate models could even be a factor of 5 larger than can be explained by these models. While this divergence among the models could

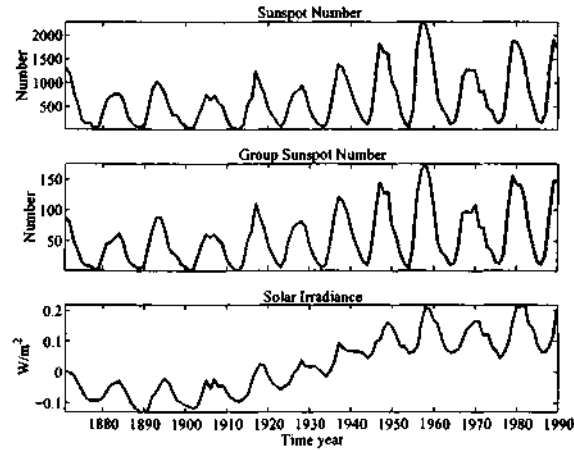


Figure 2.8. Solar Activity Time Series. The bottom panel shows the solar irradiance reconstruction by Lean (2004)

affect studies of the physics of the problem, for the present work it is the pattern of the solar irradiance time series that is more relevant. We therefore use the standardised solar irradiance (Lean 2004) for this analysis.

2.1.3 ENSO Index

We consider three different ENSO indices for our analysis, namely, the global SST ENSO index, and the Nino 3 and Nino3.4 SST anomalies.

The global SST ENSO index has been obtained from JISAO data site at <http://jisao.washington.edu/data/globalsstenso/>. The data uses the eastern equatorial Pacific SST index as an ENSO index. The index is taken as the average SST anomaly equatorward of 20 degrees latitude (north and south) minus the average SST poleward of 20 degrees, i.e (20N–20S) minus (20N–90N,20S–90S) over the longitude grid $0^{\text{deg}}E - 358^{\text{deg}}E$. The anomalies are in hundredths of a degree Celsius and are measured with respect to the period 1950-79. The number of observations contributing is at least 1000 in each month and year beginning in 1850. The input data is the Comprehensive Ocean-Atmosphere DataSet (COADS), version 2.0, for 1800-1997 and the National Center for Environmental Prediction real-time marine data for 1998 to 2003. Computing the index as the difference of two time series removes a spurious step-jump in SST observations at the onset of World War II. This jump is associated with changes in measurement practices. The difference also removes the common portion of the trend in SST. The monthly ENSO index data have been summed over a year to obtain the annual ENSO index.

The data for Nino Region 3 SST anomalies (indices) in degrees Celsius are discussed and appear as figures in Trenberth (1997). The Nino 3 Region is bounded by 90W-150W and 5S-5N. Monthly means were computed for each time series for the period 1950-1979. These

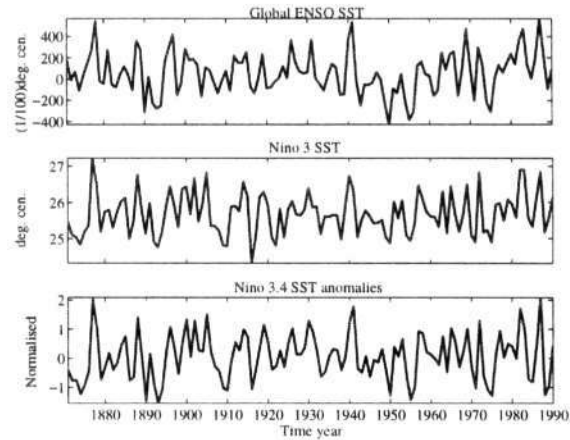


Figure 2.9. SST Time Series.

means were then subtracted from their respective time series for the entire data set (1950-1998). Finally, a five-month running mean was applied to each time series. The data is at http://www.cgd.ucar.edu/cas/catalog/climind/Nino_3_3.4_indices.html. The raw SST data is from the NOAA Climate Prediction Center at the website <http://www.cpc.ncep.noaa.gov/data/>.

The Nino 3.4 Region is bounded by 120W-170W and 5S-5N. The computational recipe for the Nino 3.4 index involved computing the area-averaged total SST over each month from the Nino 3.4 region as well as the monthly mean over 1950-1979 and then subtracting the latter from the former to obtain the SST anomalies. The anomalies are then smoothed with a 5-month running mean and then normalised by the standard deviation over the climatological period 1950-1979. The value -9.999 denotes 'missing' data. An ASCII text version of this file may be obtained at <ftp://ftp.cgd.ucar.edu/pub/CAS/TNIN34>. Figure 2.9 shows the three SST time series under consideration.

2.2 Discussion

The range of scales over which the rainfall data can provide useful information on temporal variability is limited at one end by resolution, since not more than 12 points per year are available, and at the other end by the limited length of data stretch of 120 years. Our aim here is to study possible correlations of the solar activity with the rainfall data and the ENSO index with time scales of order years to decades. Although these data are available in monthly as well as quarterly resolution, we filter out fluctuations in these data at small time scales by using yearly data. For the present study we have found annual rainfall to be the most appropriate rainfall index to use. For the rest of the analysis to follow, we shall be using the annual rainfall data from the five homogeneous regions as well as the HIM and All India Summer Monsoon

Rainfall data, together with the sunspot number , group sunspot number , solar irradiance and the ENSO, Nino3 and Nino3.4 indices.

A detailed time-domain analysis using statistical methods follows in the next chapter.

Time Domain Analysis

3.1 Introduction

Over the 120 y period (1871–1990) solar activity parameters exhibit nonstationarity as can be seen in figure 2.8 of the previous chapter. Taking this fact into account, we present here the results of an analysis of the three solar activity indices and the seven major Indian monsoon rainfall time series mentioned in Chapter 2. We perform the analysis over two distinct test periods respectively of low and high solar activity, each comprising three complete solar cycles. In the sections to follow we first illustrate the results graphically and then describe the statistical significance-testing scheme adopted to analyse the results. Further, results of the statistical analyses for rainfall over all the individual meteorological subdivisions will also be presented, as also the results of the time-domain statistical analysis on the three SST time series.

3.2 Identifying nonstationarity in time series

A brief background history on the study of solar-terrestrial connections has been presented in Chapter 1. Studies by Jagannathan and Bhalme (1973) as well as Jagannathan and Parthasarathy (1973) used mainly classical correlation and power spectral analysis to identify significant periodicities in the rainfall distribution. They reported the presence of the 11-year sunspot cycle at significance level of 95% or higher in only 5 meteorological stations. In the detailed periodicity analysis of Indian monsoon rainfall undertaken more recently by Krishna Kumar (1997), an 11-year periodicity has not been found with greater than 90% significance. Indeed, correlations attempting to describe sun-weather relations have not been robust in time, and sometimes may have switched signs (see Walker (1923)).

In all these studies, the nonstationarity of the processes analyzed was not recognized, and hence classical spectral analysis can lead to misleading results.

Now simple cross correlations already show that solar activity effects are not immediate, but they could be cumulative over a decadal scale, so that the effects (if any) are to be sought in the climate and not the weather. Figure 3.1 shows the time series of three solar activity parameters. All three clearly show a non-stationary character over the duration of the data stretch. To

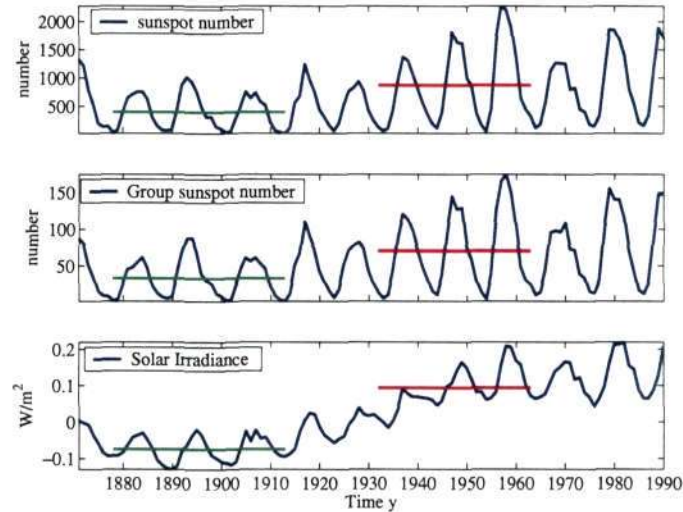


Figure 3.1. Time series of three solar indices, indicating test periods of low and high solar activity selected for analysis, and the means over the test periods for each parameter in green and red respectively.

test for possible connections between solar activity and rainfall, especially over multi-decadal scales, it seems appropriate to select two periods, of approximately the same duration, over which the contrast in solar activity is as high as possible. Furthermore, to allow for cumulative effects of solar activity on the rainfall, it is preferable to choose consecutive complete solar cycles (considering the period from one minimum to the next as one complete cycle) in each of the two test periods. Based on these considerations the most appropriate choice turns out to be the two intervals 1878–1913 and 1933–1964 respectively; each comprises three complete cycles, and has neighbouring cycles at either end of higher and lower amplitudes respectively. For comparison, brief results will be cited also for the sub-optimal test periods 1878–1933 and 1934–1986, each comprising five complete cycles. Longer full-cycle test periods will clearly overlap.

The rainfall time series are illustrated in Figure 3.2 by plots of data for three homogeneous regions and (as an interesting extreme case) the Konkan subdivision (on the west coast). While the solar indicators have a clearly cyclic character, the rainfall time series appear irregular and random, but one can already notice the marked difference in average rainfall between the two test periods, especially for the Konkan time series. (Incidentally such marked differences are seen all along the west coast.)

3.3 Statistical Significance Test

To test for possible connections between solar activity and rainfall, especially over multi-decadal scales, we therefore adopt the following procedure:

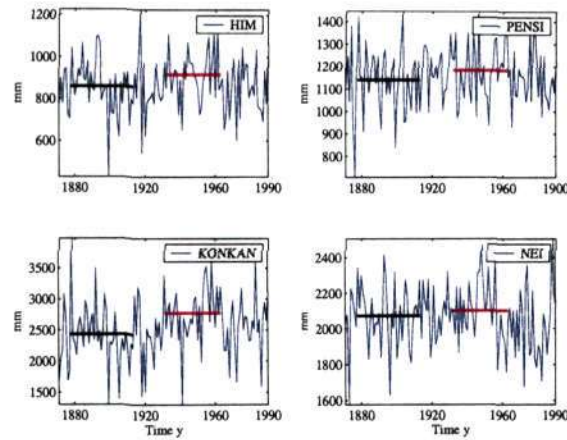


Figure 3.2. Time series showing four Indian rainfall indices, indicating test periods of low and high solar activity selected for analysis, and the means over each test period.

- 1) Select two test periods of approximately same duration over which the contrast in solar activity is the highest.
- 2) To allow for cumulative effects of solar activity on the rainfall, choose consecutive complete solar cycles in each test period

The most appropriate choice for the two test periods is clearly 1878–1913 and 1933–1964.

Each test period comprises three complete cycles, and has neighbouring cycles at either end of higher and lower amplitudes respectively.

3) Perform the following tests. *Z*-test:

Null Hypothesis: Means over the two test periods are the same .

F-test:

Null Hypothesis: Variances over the two test periods are the same.

Rejection of the null hypothesis indicates the presence of trends at an appropriate confidence level.

3.4 Results

3.4.1 Rainfall

Now we compare the mean rainfall over the two periods. Table 3.4.1 lists the annual rainfall means μ_1 and μ_2 respectively for the two periods for all the homogeneous regions considered; both the test periods and the corresponding means are shown on figure 3.2. The null hypothesis

Table 3.1. Confidence levels for homogeneous rainfall regions

Region	μ_1 mm ¹	μ_2 mm ²	% con- fidence ³	$(\frac{\mu_2 - \mu_1}{\bar{\mu}} * 100)\%$ w.r.t mean ⁴
AISMR	853.5	883.0	95	3.5
HIM	858.6	916.5	96.8	6.7
WCI	1067.2	1145.7	99	7.3
PENSI	1140.5	1183.2	85	3.6
CNEI	1204.2	1235.4	80	3.0
NWI	542.0	565.1	75	5.0
NEI	2071.8	2100.2	75	1.4

that the difference in mean annual rainfall between these two periods is zero is rejected at the maximum confidence levels listed in Table 1 using a one-tailed z -test (Crow *et al.* (1960)). Thus the mean annual rainfall during 1933–64 (higher solar activity) is everywhere higher than that during the period 1878–1913 (lower solar activity). However the confidence level is 95% or higher in 3 cases out of 7, including AISM and HIM, and reaches 99% in WCI. At the other extreme, it is a low 75% in NEI and NWI. Also listed in the table are the percent differences in mean rainfall over the two test periods as compared to the respective annual mean rainfall. ^{1 2 3 4}

These percentages as well as the percentage confidence level for the z -test considered are depicted on a map of India for the homogeneous regions in figure 3.3. It appears from this figure that the sunspot-rainfall association is strong over much of India but weak over the north-west and north-east. This analysis is further extended for all the individual meteorological subdivisions of India and the results are shown in the form of a colour coded map in figure 3.4. The west coast subdivisions of Konkan, Kerala and Coastal Karnataka as well as West Madhya Pradesh show highly significant results (96.3% to 99.9%). In fact figure 3.4 shows that rainfall during 1933-1964 has been strikingly higher than during 1878-1913 along the entire western coast.

Results from the standard F -test (Crow *et al.* 1960) are listed in Table 3.4.1. They show that the variances in test period 1 are greater than those in test period 2 in 19 out of 29 subdivisions, 15 of which are generally in the western half of the country. Confidence levels vary from 50% to 99.9%, see Table 3.4.1.

3.4.2 Results from SST data

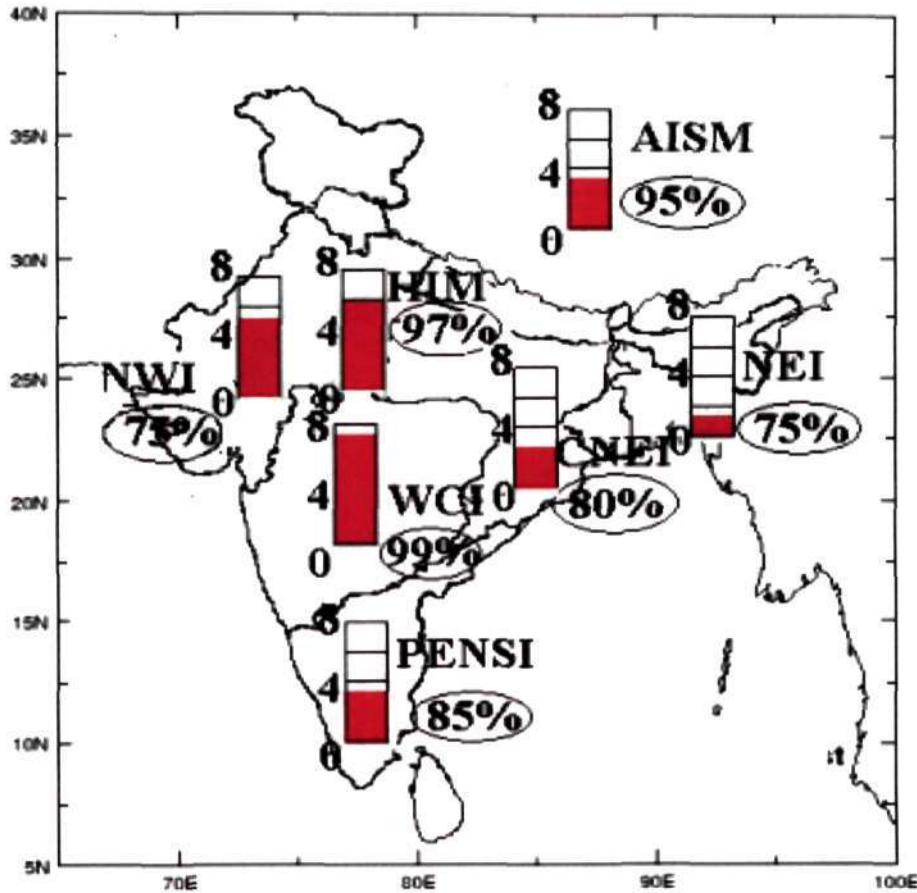
The three time series for the sea surface temperature (SST) data considered for the analysis, namely Nino3, Nino3.4 and global ENSO, are shown in figure 3.5. It can be readily seen that the

¹Mean rainfall over three cycles of low solar activity, 1878-1913.

²Mean rainfall over three cycles of high solar activity, 1933-1964.

³Confidence level at which $\mu_1 - \mu_2$ differs from zero by the z -test.

⁴% Difference in mean rainfall over the two epochs with respect to the annual mean rainfall.



S32.593
P05

Figure 3.3. Map showing homogeneous monsoon regions of India. Marked in bars are the % difference of rainfall means over test periods with respect to the annual means and encircled numbers next to them indicate the confidence level at which the differences are significant.

major trend of all the three different data over the two test periods is identical with the mean anomalies in the lower solar activity period being higher than those in the higher solar activity period (unlike rainfall, which is higher in higher solar activity period). This is to be expected, as it is well known that monsoon rainfall and ENSO indices are generally anticorrelated. However the confidence levels to which the differences in means over the two test period are significant are highest in case of the global ENSO data (95%), and lowest in case of Nino3.4 (55%).

3.4.3 Five-cycle test period

For the five-cycle solar activity test periods 1878–1933 and 1934–1986 the mean rainfall in 4 of the 6 rainfall time series in the second test period is again higher, but at lower confidence levels, varying from 62.5% (PENSI) to 92.5% (WCI), as can be seen in figure 3.6. The results

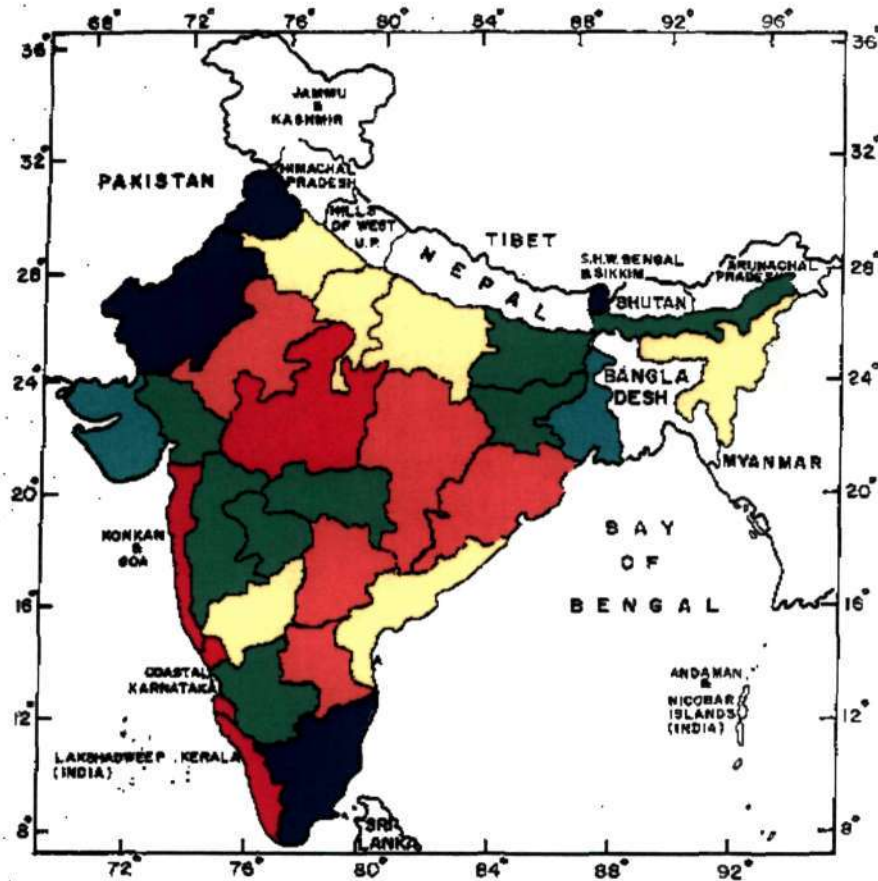


Figure 3.4. Rainfall differential map of meteorological subdivisions of India. Marked in colours are the % confidence levels to which the difference of rainfall means over the two test periods are significant. Red: 95–99.99%, orange: 90–95%, yellow: 80–90%, green: 70–80%, blue: 60–70% and cyan: 50–60%.

for NEI and CNEI rainfall and the ENSO index however show the opposite trend which is not unexpected.

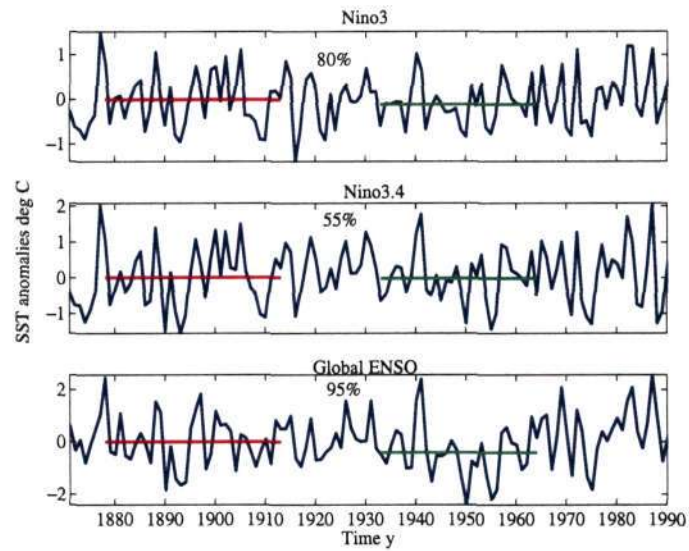


Figure 3.5. Nino3, Nino3.4 and global ENSO time series. Marked in red are the respective means over the test-period 1 which are greater than the means marked in green for test-period 2 at the indicated confidence levels by the z -test.

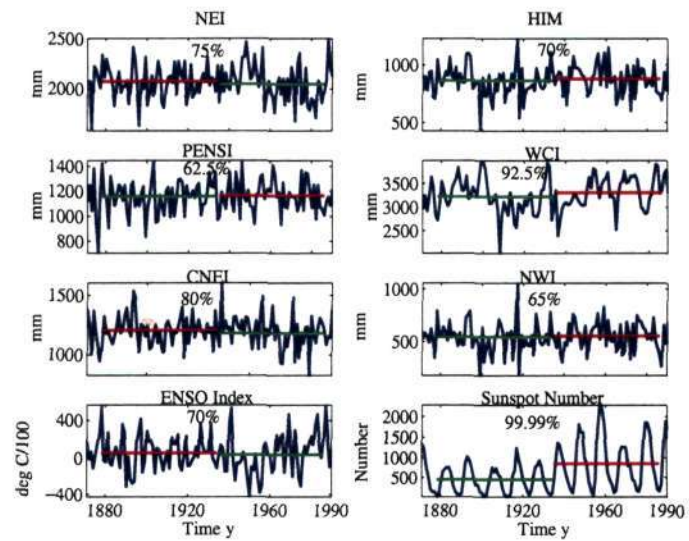


Figure 3.6. Rainfall over homogeneous regions, sunspot number and global ENSO time series. Means marked in red are greater than the means marked in green over the five-cycle test-periods considered, at the indicated confidence levels by the z -test.

Table 3.2. z test confidence levels for the subdivisions

Region	% confidence levels	$(\frac{\mu_1 - \mu_2}{\mu})\%$
Coastal Andhra Pradesh	82.5	-4.7
Coastal Karnataka	96.3	-7.9
Kerala	97.0	-6.8
Madhya Maharashtra	72.5	-2.9
Marathawada	77.5	-4.2
North Interior Karnataka	87.5	-5.2
Rayalaseema	92.5	-7.5
South Interior Karnataka	72.5	-2.1
Saurashtra	57.5	+2.1
Telangana	92.5	-7.7
Tamil Nadu	62.5	+1.1
East Madhya Pradesh	92.5	-4.9
East Uttar Pradesh	82.5	-4.6
Gangetic West Bengal	50.0	+0.2
Bihar Plains	77.5	+2.9
Bihar Plateau	77.5	-2.7
Punjab	62.5	-2.5
Gujrat	72.5	-4.2
Haryana	87.5	-7.0
Konkan	99.9	-13.5
West Madhya Pradesh	99.9	-12.3
West Uttar Pradesh	82.5	-4.9
West Rajasthan	62.5	-2.7
Orissa	92.5	-4.3
South Assam	87.5	-2.4
North Assam	77.5	-1.7
Sub-Him West Bengal	67.5	+1.5
East Rajasthan	92.5	-9.2
Vidharbha	77.5	-3.4

3.5 Conclusions

The present statistical analysis, over the identified test periods of high and low solar activity, leads to the following conclusions:

- Greater solar activity is associated in all cases with greater rainfall, although at significance levels that are distinctly high (exceeding 97%) in 2 out of 6 homogeneous cases studied (HIM (97%) and WCI (99%)), and greater than 75% even in the other 4 cases (NEI (75%), NWI (75%), CNEI (80%) and PENSI (85%)). (AISM rainfall does not represent a homogeneous region, and for this reason it is not the best case for studying solar/rainfall associations; but even here the confidence level is 95%.)
- In 9(15) out of 29 subdivisions, rainfall is higher during the high solar test period at z -test confidence levels exceeding 90%(80%) respectively.
- The strongest connections between solar activity and rainfall are observed along the west coast and in central India, and the weakest in northwest and north-east India.
- The mean SST anomalies in the lower solar activity period are higher than those in the higher solar activity period. The confidence levels at which the difference in means is significant are highest in case of the global ENSO data (95%) and lowest in case of Nino3.4 (55%).

We believe the present results are robust because (i) although there are regional variations, many independent rainfall time series show strong effects over geographically contiguous and climatologically coherent zones (including the west coast, not separately identified as a homogeneous zone in the analysis of Parthasarathy *et al.* (1993)); (ii) 3- and 5-cycle test periods lead to mutually reinforcing conclusions. Further we may note that the regional variations revealed by the present analysis are not inconsistent with the simulations of Haigh *et al.* (2004); see also Kodera (2005), Van Loon (2005), Ruzmaikin (2005), all of whom suggest that a major effect of higher solar activity may be a displacement in the Hadley cell. Such a displacement of coherent circulation patterns, depending on its magnitude, can have different effects on rainfall in different regions. This issue will be discussed at greater length in Chapter 10.

The present analysis provides strong evidence for a connection between Indian rainfall and solar processes, not only on centennial or millennial scales (which has been shown in the case of certain rainfall proxy data), but also on multi-decadal scales, using actual reliable measured rainfall.

Wavelet Power Spectral Analysis

4.1 Introduction

Wavelet transform analysis is a powerful tool which is well suited to the study of multiscale, nonstationary processes over finite spatial and temporal domains (see Daubechies (1990)). A time series can be easily decomposed in a time-frequency plane using wavelet transforms. This enables one to determine the dominant modes of variability, including how those modes vary with time. A step by step method of performing continuous wavelet analysis together with associated statistical significance tests on the wavelet spectrum is provided by Torrence and Compo (1998).

Wavelet methods have earlier been used to analyse Indian rainfall by Torrence and Webster (1998), Torrence and Compo (1998), Kailas and Narasimha (2000), and Narasimha and Kailas (2001). In particular, the last reference analyses Indian monsoon rainfall and identifies six 'quasi cycles', with average periods of 2.92, 5.8, 11.4, 19.9, 34.2 and 79.8 y. Iyengar and Raghukantha (2004), using the totally independent method of 'intrinsic' mode functions introduced by Huang *et al.* (1998), have identified 'intrinsic' modes with periods virtually identical to those observed by Narasimha and Kailas (2001). These numbers suggest the presence of several super- and sub-harmonics of the basic sunspot period of about 11 y. In continuation of this on-going research, we now present an analysis of the possible association between indicators of solar activity and Indian monsoon rainfall using the continuous wavelet transform (with the Morlet mother function) as the basic tool.

4.2 Wavelet Power Spectrum

Since an extensive literature on wavelet analysis is available in the pioneering works of Grossman and Morlet (1984), Daubechies (1992), Chui (1992), Meyer (1993), Mallat (1989) and Farge (1992), we briefly mention only a few useful results on continuous wavelet transforms. We choose the complex Morlet wavelet as the mother wavelet, since it is specially useful in determining the presence of cycles (Kronland-Martinet *et al.* 1987).

The Morlet wavelet function is given by

$$\Psi_0(\eta) = \pi^{-1/4} e^{i\omega_0\eta} e^{-\eta^2/2}, \quad (4.1)$$

where ω_0 is a nondimensional frequency, taken equal to 6 in order to satisfy the admissibility condition whereby the wavelet function must have zero mean and must be localized in both time and frequency space (see Farge 1992). η is a nondimensional time parameter. Figure 4.1 shows the Morlet function.

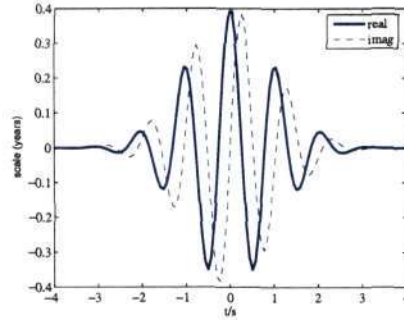


Figure 4.1. The real and imaginary part of the complex morlet wavelet in the time domain

For a discrete sequence R_n , $n = 0, \dots, (N - 1)$, the continuous wavelet transform $W_n^R(s)$ is defined as the convolution of R_n with a scaled and translated version of the wavelet function $\Psi(\eta)$, as given by the expression

$$W_n^R(s) = \sum_{n'=0}^{N-1} R_{n'} \psi^* \left[\frac{(n' - n)\delta t}{s} \right], \quad (4.2)$$

where $*$ denotes the complex conjugate, and δt is the (sampling) time interval between two consecutive points in the time series. The wavelet function at each scale s is normalised to have unit energy; this demands that

$$\hat{\psi}(s\omega_k) = \left(\frac{2\pi s}{\delta t} \right)^{1/2} \hat{\psi}(s\omega_k), \quad (4.3)$$

$$\int_{-\infty}^{\infty} |\hat{\psi}(\omega')|^2 d\omega' = 1, \quad (4.4)$$

where $\hat{\psi}$ is the Fourier transform of ψ . The wavelet power spectrum of R_n is given by the convolution $W_n^R(s) * [W_n^R(s)]^*$, and the wavelet power by the magnitude $|W_n^R(s) * [W_n^R(s)]^*|$.

4.2.1 Band Averaged Wavelet Power

The band-averaged wavelet power $R_b^S(t)$ is a weighted sum of the wavelet power spectrum over a given band of scales as proposed by Torrence and Compo (1998),

$$R_b^S(t) = \frac{\delta_j \delta t}{C_\delta} \sum_{j_1}^{j_2} \frac{|W_n^S(s_j)|}{s_j}, \quad (4.5)$$

where $s_j = s_0 2^{j\delta_j}$, $j = 0, 1, \dots, J$ and $J = \delta_j^{-1} \log_2(N\delta t/s_0)$. We choose $\delta_j = 0.25y$ in order to obtain a reasonably fine resolution in scale. The constant $C_\delta = 0.776$ is a scale-independent reconstruction factor for the Morlet function (Torrence and Compo (1998)).

4.3 Results

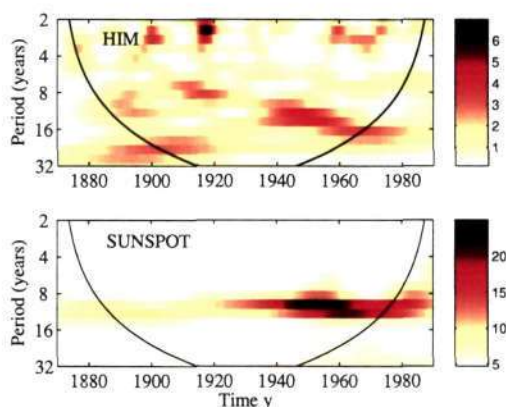


Figure 4.2. Wavelet power spectrum of HIM rainfall (top panel) and sunspot number (bottom panel)

In order to investigate whether a more direct association between solar activity and rainfall can be established, we now present a wavelet analysis in the form of colour-coded contour maps of wavelet power spectra as functions of time and Fourier period (henceforth referred to as period), as shown in figures 4.2 to 4.5. The individual wavelet power maps for the HIM rainfall and sunspot number are respectively shown in the top and bottom panels of figure 4.2.

From the distribution of wavelet power in the two cases, it may be noted that the nonstationarity in HIM time series at various time scales is greater than that present in the sunspot time series. It is seen that the 8-16 y period band exhibits by far the highest wavelet power in the case of sunspot number. Although the sunspot cycle is normally considered to have a period of about 11.6 y, different numbers are quoted in the literature. Solar cycle lengths vary

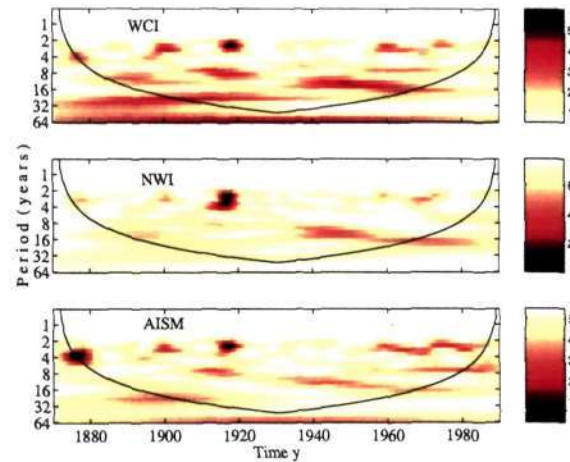


Figure 4.3. Wavelet power spectrum of WCI rainfall (top panel), NWI rainfall (middle panel) and AISM rainfall (bottom panel)

over the range of 9 to 13 y (Lassen and Friis-Christensen (1995)). The value 11.6 y is close to the geometric mean of the ends of the 8-16 y band. While the 8-16 y period band exhibits the highest wavelet power in the case of sunspot number, HIM exhibits the most power in the 2-7 year band, but substantial power in the 8-16 y period band also, thus suggesting connections with solar activity.

Figure 4.3 shows the wavelet power spectra for WCI, NWI and AISM rainfall. WCI exhibits substantial power in the 8-16 y as well as 16-32y period bands as compared to the 2-7 y band; NWI exhibits high power over the short time interval (or epoch) 1915-1920 in the 2-4 y band and considerable power over the longer stretch 1935-1960 in the 8-16 y band, while AISM rainfall shows high power in short stretches (1873-1881, 1897-1903, 1915-1920, and 1956-1977) in the 2-7 y band but considerable power over the longer stretches 1906-1920 and 1930-1950 in the 8-16 y band. Incidentally the characteristics of AISM rainfall noted above may well be a consequence of the heterogeneity of the index, in contrast to those corresponding to the homogeneous regions.

The wavelet power spectra for NEI, CNEI and PENSI are shown in figure 4.4. NEI and PENSI show substantial power in short stretches over the 2-7 y and 16-32 y bands, almost exhibiting an antiphase relationship to HIM, while CNEI shows power well distributed over the 2-7y, 8-16y as well as the 16-32 y period bands. In fact CNEI shows characteristics which are in-between those of HIM and NEI.

Figure 4.5 shows the wavelet power spectra for the global ENSO index, Nino 3.4 and Nino 3 SST. Both the ENSO index and Nino 3 SST exhibit prominent power not only in the 3-7 y band but also in the 8-16 y band, although the power is higher mostly in the first half of the time duration 1871-1920. Nino 3.4 SST does not show considerable power in the 8-16 y band as compared to the 3-7y period; there seems to be no marked difference between the power over

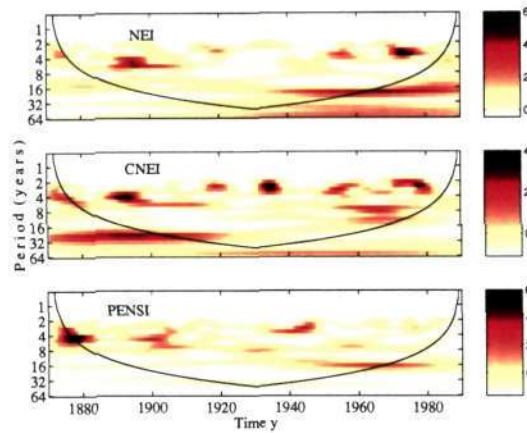


Figure 4.4. Wavelet power spectrum of NEI rainfall (top panel), CNEI rainfall (middle panel) and PENSI rainfall (bottom panel)

the first (1871-1920) and second half (1921-1990) of the time duration in this case.

Not only HIM, but WCI, NWI, AISM as well as CNEI rainfall and ENSO and Nino 3 SST index, exhibit most power in the 2–7 year band, but substantial power in the 8–16 y period band also, thus indicating connections with solar activity.

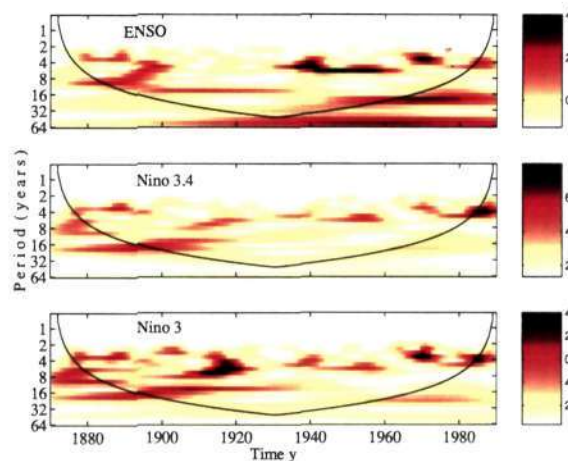


Figure 4.5. Wavelet power spectrum of ENSO (top panel), NINO 3.4 (middle panel) and NINO 3 (bottom panel) sst index.

4.4 Power in different period bands

In order to make a quantitative comparison, we compute the wavelet power over the dyadic period bands 2–4, 4–8, 8–16, 16–32, and 32–64 y as percentages of total wavelet power for each case. The results are shown in figure 4.6. (Incidentally we adopt the convention that when we refer to the (m-n) year band we mean the years m, m+1, ..., n-1.) It can be seen that the contributions in the 8–16 y band vary over the range 11.3% to 25.2% among the rainfall time series considered (the highest being in NWI and HIM) and between 14.8% in ENSO to 21.1% in Nino 3.4 SST indices.

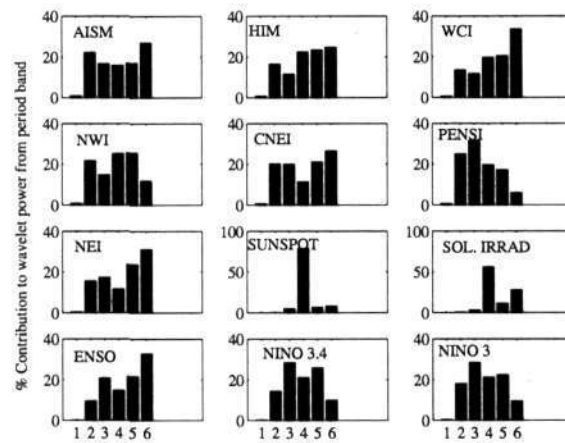


Figure 4.6. Individual wavelet power over different period bands as percentages of the total individual wavelet power. Band (1): 1–2 y, (2): 2–4 y, (3): 4–8 y, (4): 8–16 y, (5): 16–32 y, (6): 32–64 y; the band limits are closed on the left and open in the right of the interval.

4.4.1 Band Averaged Wavelet Power

To further study the implication of the presence of relatively high power in the 8–16 y, 9–13 y and 10–12 y bands, we make a comparison of the mean wavelet power in these bands over the two three-cycle test periods introduced in Chapter 3, namely, 1878-1913 and 1933-1964. These plots are shown in figures 4.7 and 4.8 in case of the rainfall and in figure 4.9 in case of ENSO indices. In the bottom most panel of each of these figures is shown the corresponding plot for the solar activity index. It can be readily seen that the mean band averaged wavelet power over test period 2 (i.e. 1933-1964) is greater than that in test period 1 (i.e. 1878-1913) across all the bands for six out of seven rainfall time series considered, the only exception being NEI. Similar behaviour is observed for the sunspot number (see figure 4.7, bottom panel) as well as for group sunspot number (see figure 4.8, bottom panel). However in case of solar irradiance, shown in figure 4.9, bottom panel, the 10–12 y band averaged power shows higher power in test period

1 as compared to that in test period 2, the trend in this case being reverse to that observed at the 10-12 y band averaged power for sunspot and group sunspot number. The trend in ENSO-rainfall indices is again consistently opposite to those of the rainfall-sunspot and rainfall-solar irradiance in the bands considered.

A z -test, already described in Chapter 3, has been performed to determine the statistical significance of the difference in the mean band averaged wavelet power over the two test periods. The values of the z -statistic so obtained in each of the cases is listed in table 4.1. Values of z -stat greater than 3.719 in magnitude indicate confidence level of 99.99% or higher.

In all the rainfall cases except NEI, and in all solar activity cases except irradiance, the power is higher in the period of higher solar activity compared to that in the low activity period, at confidence levels exceeding 99.9% by the z -test. With the few exceptions in case of three bands (those of 8-16 y, 9-13 y and 10-12 y) for solar irradiance and two bands (those of 9-13 y and 10-12 y) for Nino 3.4, all the other cases pass the test at confidence levels of 99.95% or greater.

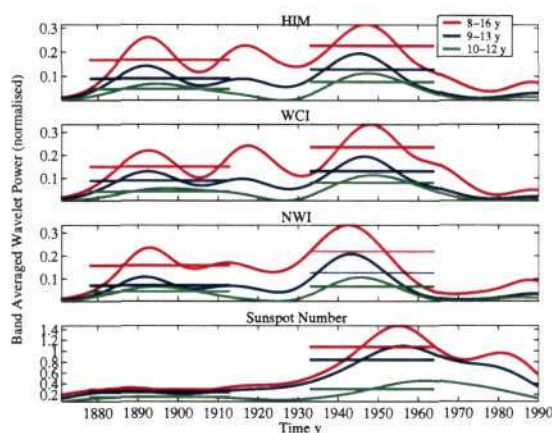


Figure 4.7. 8-16 y, 9-13 y and 10-12 y Band averaged wavelet power: HIM, WCI, NWI rainfall in the top three panels and Sunspot number in the bottom panel. Marked on respective curves are straight lines showing the means over each of the two test periods.

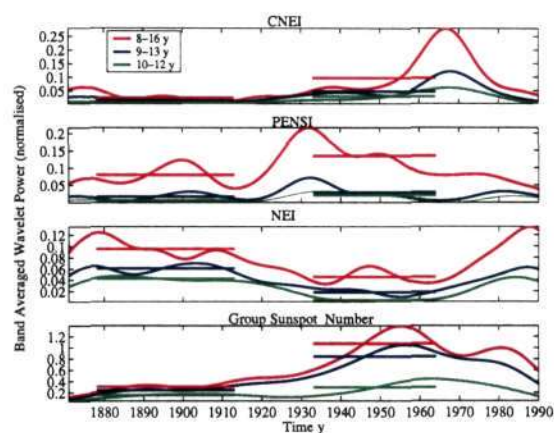


Figure 4.8. 8–16 y, 9–13 y and 10–12 y Band averaged wavelet power: CNEI, PENSI, NEI rainfall in the top three panels and Group Sunspot number in the bottom panel. Marked on respective curves are straight lines showing the means over each of the two test periods.

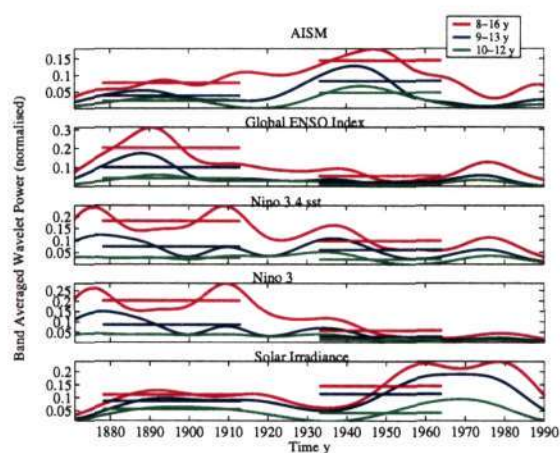


Figure 4.9. 8–16 y, 9–13 y and 10–12 y Band averaged wavelet power: AISM rainfall, ENSO, Nino 3.4, Nino 3 SST indices in the top four panels and solar irradiance in the bottom panel. Marked on respective curves are straight lines showing the means over each of the two test periods.

Table 4.1. Values of z statistic for the rainfall, ENSO and solar activity

Data	Criterion	$z\text{-stat} = -1.645 \rightarrow 95\%$	$z\text{-stat} = -3.719 \rightarrow 99.99\%$	
		$z\text{-stat}$ using 8-16 y band	the $z\text{-test}$ 9-13 y band	10-12 y band
Rainfall				
HIM	$\mu_2 > \mu_1$	-3.84	-3.55	-4.90
WCI	$\mu_2 > \mu_1$	-5.75	-4.51	-7.31
NWI	$\mu_2 > \mu_1$	-3.10	-4.52	-3.47
CNEI	$\mu_2 > \mu_1$	-6.58	-9.56	-9.35
PENSI	$\mu_2 > \mu_1$	-6.80	-3.33	-8.47
NEI	$\mu_2 < \mu_1$	16.16	28.88	59.01
AISM	$\mu_2 > \mu_1$	-11.99	-5.71	-7.16
Solar Activity				
Sunspot Number	$\mu_2 > \mu_1$	-13.48	-14.70	-7.08
Gr. Sunspot	$\mu_2 > \mu_1$	-16.28	-17.66	-7.08
Sol. Irradiance	$\mu_2 > \mu_1$	- 2.71	-2.89	2.60
ENSO Indices				
ENSO	$\mu_2 < \mu_1$	11.38	8.18	13.02
Nino 3.4	$\mu_2 < \mu_1$	8.55	2.60	2.02
Nino 3	$\mu_2 < \mu_1$	14.02	7.52	8.89

4.5 Conclusion

From this analysis we conclude the following:

- Wavelet power spectra of all the time series under consideration show substantial power in the 8–16 y period band.
- The contribution to the total wavelet power from the 8–16 y band varies from 11.3% (NEI) to 25.2% (HIM) among the rainfall time series, and between 14.8% (ENSO) to 21.1% (NINO3) in ENSO indices.
- Except for NEI, all the other six rainfall time series show that wavelet power is higher in the period of higher solar activity and lower in the period of lower solar activity, the difference between them being significant at confidence levels greater than 99.9%.
- Higher ENSO activity is connected with lower rainfall and lower solar activity.
- The wavelet power of the ENSO indices is higher during the lower solar activity period and lower in the higher solar activity period, thus showing a trend opposite to that of rainfall-solar activity. Even in these cases, the confidence levels at which the differences (in band averaged wavelet power over the two test-periods) are significant are greater than 99.99% for all cases except for the two bands (9–13 and 10–12 y) in the case of Nino 3.4, where the confidence levels are about 97.5%.

With these results in mind, we now go on to analyse the wavelet cross power spectrum in all these cases in the next chapter.

Wavelet Cross Spectral Analysis by Torrence-Compo Method

5.1 Introduction

The wavelet power spectrum results shown in the previous chapter for the time series of rainfall, solar activity and ENSO indices reveal interesting similarity in the distribution of wavelet power over a range of scales that demands further investigation. A multivariate analysis of the above time series enables inter-comparison between them, and the unraveling of any connections or associations between them. In order to carry out such an analysis, we look at simple bivariate cross-spectra of solar activity indices respectively with the rainfall and ENSO indices. An analogue of the Fourier cross-spectrum, called the wavelet cross spectrum, enables simultaneous description of the time-frequency characteristics of both the time series under consideration.

Using once again the Morlet continuous wavelet transform on data over the period 1871-1990, it is found that the global wavelet cross spectra between two solar activity indices (sunspot number and solar irradiance) and seven major Indian monsoon rainfall time series show significant power around the period of the 11 year solar cycle. Furthermore two distinct epochs are found in the computed cross-spectrum, the transition between them occurring around the decade 1915-1925, beyond which solar activity parameters show a significant increase. The details of the wavelet cross spectral analysis, the statistical significance testing technique used by Torrence and Compo (1998) and the results are presented in the following sections. We shall in particular demonstrate that the Torrence-Compo method has certain limitations when one of the time series (solar activity in our case) has a strongly periodic behaviour.

5.2 Wavelet Cross Power Spectrum

The wavelet power spectrum has been already introduced in the previous chapter. For the wavelet cross power spectral analysis presented in this Chapter, we utilize the easy-to-use toolkit, as well as the statistical significance testing procedure, outlined by Torrence and Compo (1998). We shall show in the next chapter that the Torrence-Compo procedure is misleading for analysing

problems of the present kind.

The cross wavelet spectrum $W_n^{RS}(s)$ between two time series $R_n(t)$ and $S_n(t)$, with the respective wavelet transforms $W_n^R(s)$ and $W_n^S(s)$, may be defined as

$$W_n^{RS}(s) = W_n^R(s) [W_n^S(s)]^* . \quad (5.1)$$

The cross wavelet power is $|W_n^{RS}(s)|$.

5.2.1 Global Wavelet Power Spectrum

A vertical slice through a wavelet spectrum on the time axis of the time-frequency plane is a measure of the local spectrum. The wavelet power at a given scale s at time t is called the local spectrum at the point (t, s) in the time-frequency plane. A time-average over all the local wavelet spectra gives the global wavelet spectrum,

$$\bar{W}^2(s) = \frac{1}{N} \sum_{n=0}^{N-1} |W_n(s)|^2, \quad (5.2)$$

where N is the total number of sample points in the data. Similarly a time average over all the local cross wavelet spectra, that is, the wavelet cross power over time t , gives the global cross wavelet spectrum at scale s as

$$\bar{W}_{RS}(s) = \frac{1}{N} \sum_{n=0}^{N-1} |W_n^{RS}(s)| . \quad (5.3)$$

5.2.2 Torrence-Compo Significance Testing Procedure

Torrence and Compo (1998) derive the confidence levels for cross wavelet power from the square root of the product of two χ^2 distributions. In the test, a peak in the wavelet power spectrum is accepted with a certain percentage confidence if the peak is significantly above a background or reference spectrum. Following Gilman *et al.* (1963), the reference spectrum is taken as

$$P_k = \frac{1 - \alpha}{1 + \alpha^2 - 2\alpha \cos(2\pi k/N)} . \quad (5.4)$$

Here $k = 0 \dots N/2$ is the frequency index, and $\alpha = (\alpha_1 + \sqrt{\alpha_2})/2$ where α_1 and α_2 are the lag-1 and lag-2 autocorrelation coefficients of the process under consideration. For a white noise background spectrum $\alpha = 0$, $P_k = 1$.

If the two time series $R_n(t)$ and $S_n(t)$ have background spectra given respectively by P_k^R and P_k^S , then according to Torrence and Compo (1998) the cross wavelet power distribution will be

given by

$$\frac{|W_n^{RS}(s)|}{\sigma_R \sigma_S} \implies \frac{Z_\nu(p)}{\nu} \sqrt{P_k^R P_k^S}, \quad (5.5)$$

where σ_R and σ_S are the standard deviations of R and S respectively, ν is the number of degrees of freedom with which χ^2 is distributed, p denotes the level of confidence and $Z_\nu(p)$ denotes the value of the χ^2 distribution with ν degrees of freedom at the confidence level p . For the complex Morlet wavelet $\nu = 2$ (Torrence and Compo (1998)).

5.3 Results for monsoon rainfall and solar activity

Detailed plots of the time series of all the annual rainfall, solar and ENSO indices under consideration have been shown in Chapter 2. It was seen there that both the rainfall and ENSO index time series appeared irregular and random, while the solar indicators revealed a clearly cyclic character. The results of the present analysis are now exhibited in the form of colour-coded con-

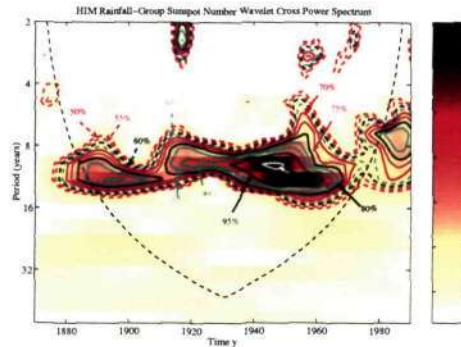


Figure 5.1. Wavelet cross power spectrum between HIM rainfall and sunspot number, contours showing regions at 50% to 99% confidence level

tour maps of wavelet cross power spectra as functions of time and period (already introduced in Chapter 4) for all the time series under consideration. Outlined on these graphs are thick contours in white, blue and green enclosing regions where wavelet cross power exceeds 99%, 95% and 90% confidence levels respectively, with respect to the reference spectra mentioned above. The cones of influence within which edge effects become important are also indicated by thin dashed lines in the figures.

Figure 5.1 shows the wavelet cross power spectrum between sunspot number and HIM rainfall as function of period. A wavelet cross power of noticeably high magnitude is observed here at the middle of the period range 8-16 years. Marked on this spectrum are the contours of regions with 50% to 99% confidence.

The global wavelet cross power spectrum is shown in figure 5.2. It can be seen that the global cross wavelet power crosses the 97.3% confidence line at a period of around 11 years.

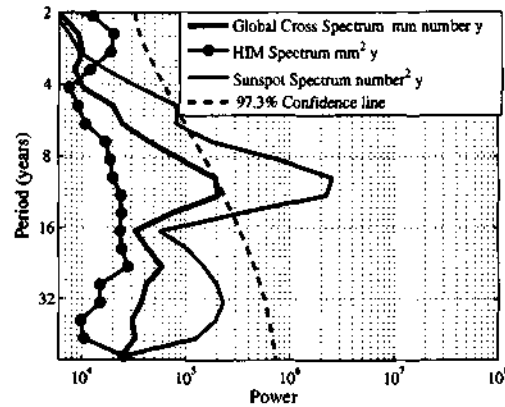


Figure 5.2. Global wavelet cross power spectrum between HIM rainfall and sunspot number

Figure 5.3 shows the wavelet cross power spectra of sunspot numbers with five homogeneous as well as AISM rainfall as function of period. A wavelet cross power of noticeably high magnitude can be observed in the middle of the period range 8-16 years in all the six cases. It may further be noted that in the case of WCI, NWI as well as AISM rainfall, the cross power in the 8-16 y period band is higher during the period 1920-1964, which in fact overlaps with test-period 2 (1933-1964) of Chapter 3. In all these three cases contours of 95% as well as 90% confidence level may be observed, particularly over the second test period.

In the other three cases (CNEI, NEI and PENSI), the results are less marked. There are only contours of about 90% confidence level in all three of them. Although a wavelet cross power of high magnitude is observed in the middle of the period range 8-16 years in case of CNEI, the contours of the 90% and 95% confidence regions are slightly shifted to the right compared to the NWI, WCI and HIM rainfall cases. In case of NEI rainfall, only a small area of 90% confidence is observed in the middle of the period range 8-16 years, and another similar contour is observed to the right of the cone of influence over 1972-1984. This is not entirely unexpected since it has already been studied and noted in the literature (see Parthasarathy *et al.* 1993, also Chapters 3 and 4 of this thesis) that the NEI has an out-of-phase relationship with HIM rainfall. Although a wavelet cross power of high magnitude is observed between PENSI rainfall and sunspots within two small contours in the middle of the period range 8-16 years, even here the power is significant only at 90% confidence.

The global wavelet cross power spectra corresponding to all these six rainfall-sunspot time series are shown in figure 5.4. It is seen that the cross wavelet power crosses the 95% confidence line at a period of around 11 years for WCI, NWI and AISM and 90% confidence level for CNEI,

NEI and PENSI rainfall.

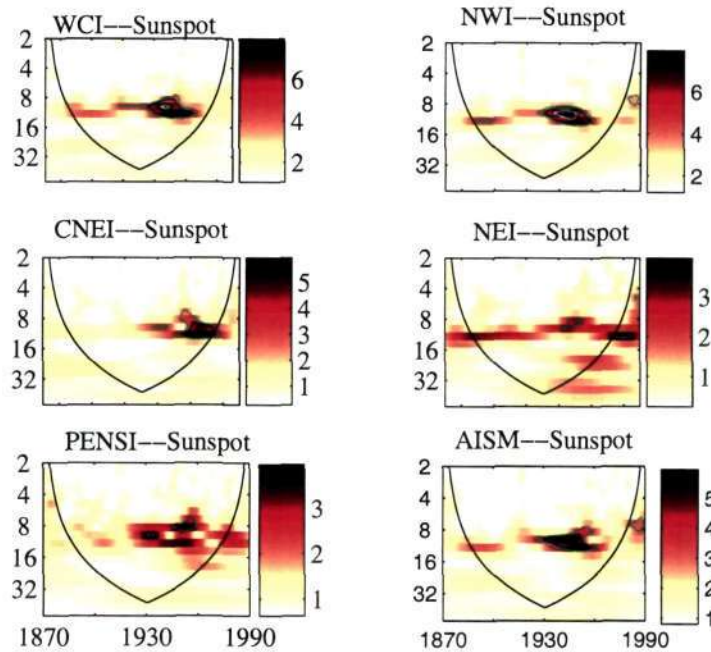


Figure 5.3. Wavelet cross power spectrum of five homogeneous and AISM rainfall with sunspot number. Contours of regions with 90%, 95% and 99% are shown respectively in green, blue and white lines.

Figure 5.5 shows the wavelet cross power spectra for AISM rainfall and solar irradiance as function of period. The correlation studies of Mehta and Lau (1997) revealed that solar irradiance and AISM rainfall co-vary with nearly the same phase. Their conclusion is supported from our results. A wavelet cross power of noticeably high magnitude is observed in the middle of the period range 8-16 years. The global wavelet cross power spectrum (see figure 5.6) shows that the cross wavelet power crosses the 95% confidence line at a period of around 11 years.

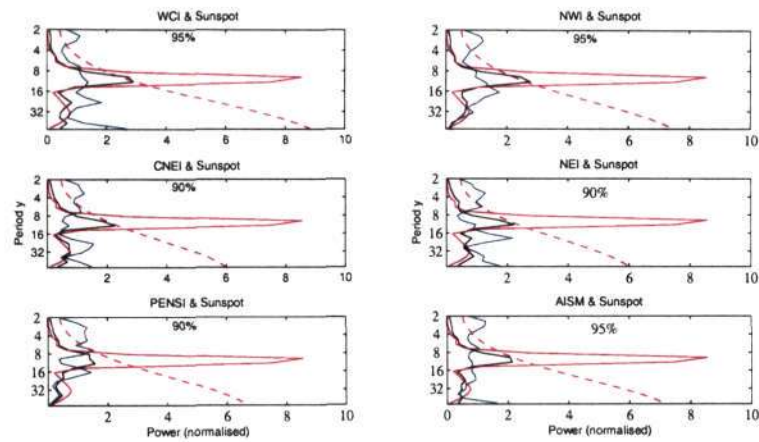


Figure 5.4. Global wavelet cross power spectrum of five homogeneous rainfall and AISM with sunspot number. Sunspot, Rainfall and Cross Spectrum shown respectively in red, blue and black lines. Confidence lines marked in red dashed lines and confidence levels indicated in each figure.

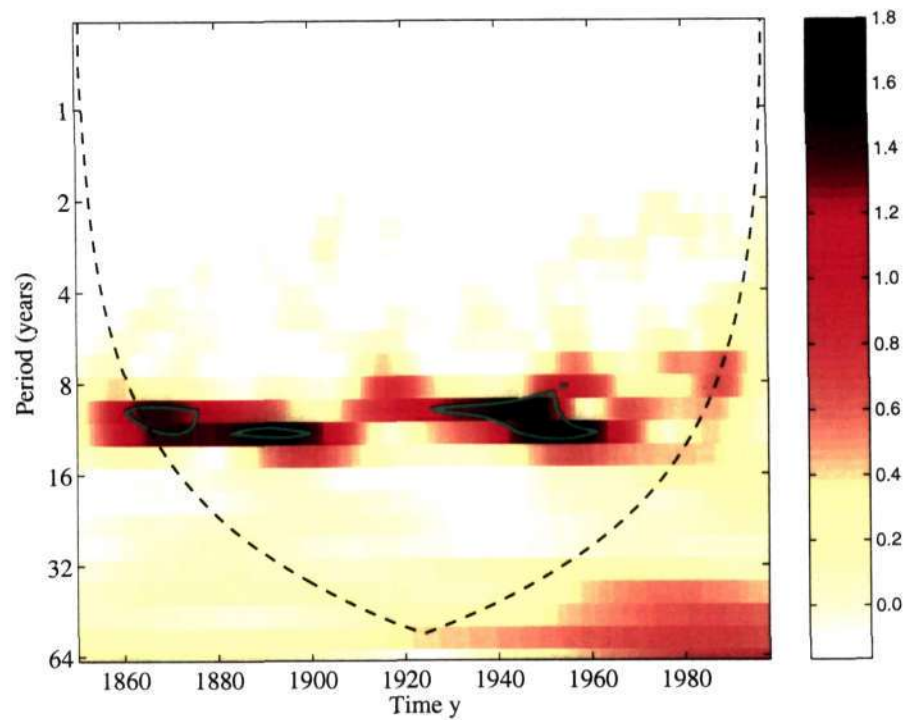


Figure 5.5. Wavelet cross power spectrum between AISM rainfall and solar irradiance, green and blue thick contours mark regions where the cross spectrum exceeds the reference spectrum at 90% and 95% confidence level respectively.

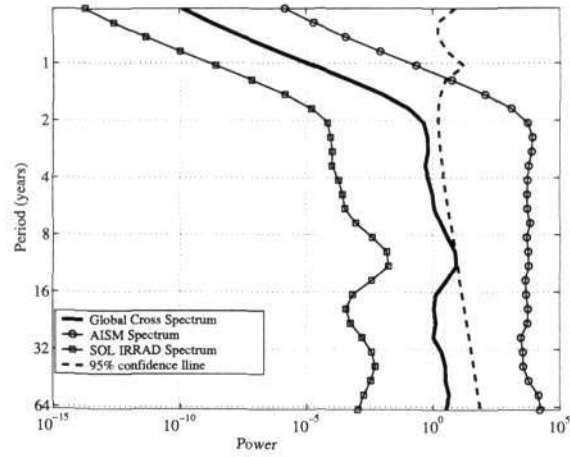


Figure 5.6. Global wavelet cross power spectrum between AISM rainfall and solar irradiance, dashed line mark regions where the cross spectrum exceeds the reference spectrum at 95% confidence level

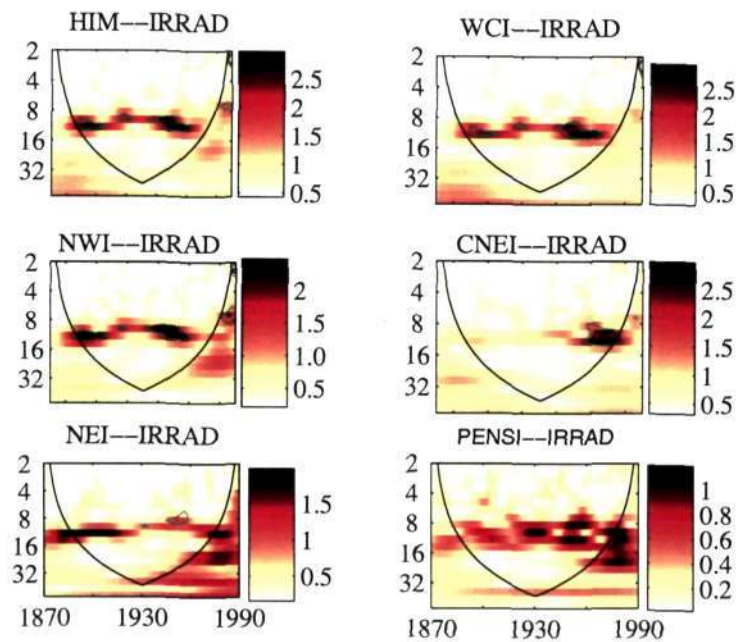


Figure 5.7. Wavelet cross power spectrum between homogeneous rainfall and solar irradiance, green and blue thick contours mark regions where the cross spectrum exceeds the reference spectrum at 90% and 95% confidence level respectively.

5.4 Results for ENSO index and monsoon rainfall

Applying the above analysis to the case of global ENSO index and monsoon rainfall time series, we obtain the following results. Figures 5.8 and 5.9 show respectively the wavelet cross power and the global wavelet cross power spectra between the global ENSO index and HIM rainfall. The regions where the spectrum is significant to more than 95% are marked in blue contours. It can be seen that these contours lie over small regions mostly spread across the 2–4 y period band, and less often across the 4–8 y, 8–16 y and even the 16–32 y period bands, although the last one falls within the cones of influence. Since the high cross power is not particularly over any period band, the global cross spectrum in figure 5.9 exceeds the reference background spectrum only at 65% confidence.

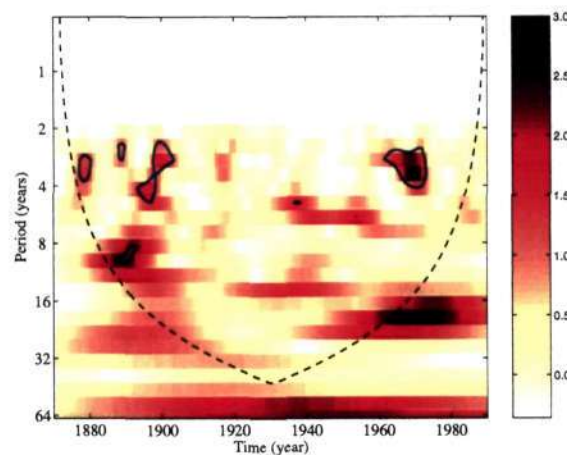


Figure 5.8. Wavelet cross power spectrum between ENSO index and HIM rainfall, blue thick contours mark regions where the cross spectrum exceeds the reference spectrum at 95% confidence levels.

Figure 5.10 shows respectively the wavelet cross power between ENSO and the five homogeneous as well as AISM rainfall time series. It can be seen that the contours of significant power lie over small regions spread across the 2–7 year period band in case of AISM. In case of NEI rainfall, these contours lie over small regions spread across the 3–7 y period band but there is also a comparatively larger contour in the 16–32 y period band, although half of this region falls within the cones of influence. The wavelet cross power spectrum of NWI with ENSO shows 95% contours in the 4–8 y period band and a bigger contour around the 22 y period, although the latter lies within the cones of influence.

The wavelet cross spectrum between WCI rainfall and the ENSO index have regions of 95% confidence distributed within the 2–6 y period band. However it can be seen that during the time-span 1880–1910 in the 8–16 y period band and 1940–1990 in the 16–32 y period band,

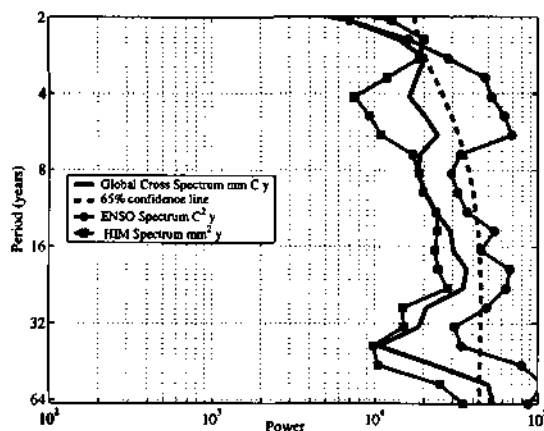


Figure 5.9. Global Wavelet cross power spectrum between ENSO index and HIM rainfall, dashed lines mark regions where the global cross spectrum exceeds the reference spectrum at 65% confidence levels.

there exists considerable crosspower. In case of ENSO index and CNEI rainfall, the 95% contour regions are spread over the 3–7 y period band. Interestingly there are two separate contours covering approximately the two solar activity test periods, the cross power in test period 1 being greater than that over test period 2. The wavelet cross power for ENSO index and PENSI rainfall also shows 95% contour regions spread over the 2–7 y period band. Even here, there are four separate contours covering approximately the two solar activity test periods, the cross power in test period 1 being much greater than that over test period 2.

The wavelet cross power spectrum between the global ENSO index and the AISM rainfall is shown in the top left panel of figure 5.10. It can be seen that these contours also lie over small regions spread across the 2–7 y period band. The global cross spectrum (figure 5.11) exceeds the reference background spectrum only at 67.5% confidence.

Figure 5.12 shows the global wavelet cross power spectrum between the ENSO index and NEI rainfall. The global cross spectrum exceeds the reference background spectrum only at 85% confidence. It may also be seen that both the individual global wavelet spectra for NEI and ENSO as well as the global cross spectrum between them seem to be in phase, peaking nearly at the same period bands of 4–8 y and 16–22y. It is interesting to note that all of them have a peak near the 22 y period. The global cross spectrum plot in figure 5.13 shows a peak in the 4–8 y period band, and also over the 16–32 y period band. It may be noticed that in the 8–16 y period band, the ENSO global spectrum exhibits a higher power as compared to the NWI rainfall spectrum.

The global wavelet cross power spectra together with the individual global wavelet power spectra for WCI and ENSO are shown in figure ???. It may be noticed that in the 4–8 y and

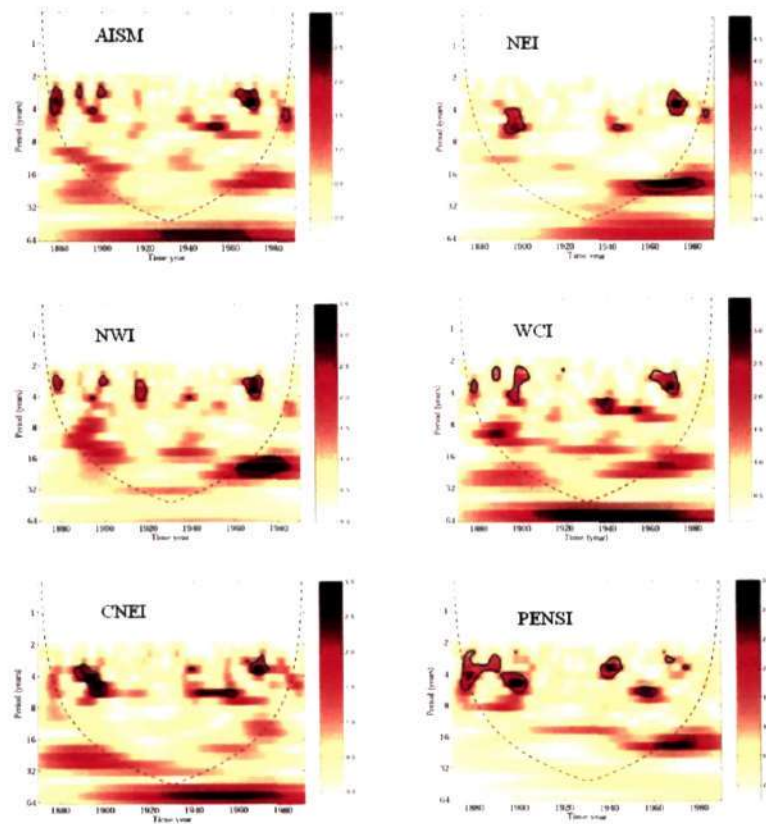


Figure 5.10. Wavelet cross power spectrum of ENSO index with five homogeneous and AISM rainfall; blue thick contours mark regions of 95% confidence levels.

8–16 y period bands the two individual spectra are out of phase while in the 2–4 y and 16–32 y period bands they are in phase with each other. The global wavelet spectra for the individual time series as well as the global cross spectra are shown in figure 5.14 for ENSO and CNEI rainfall. Even here all the three curves seem to go in phase, as in the NEI case.

The global wavelet cross spectrum for PENSI and ENSO index shows characteristics that are in-between the characteristics of the two individual wavelet spectra (see figure 5.15), and reveals a large hump over the 4–8 y period band and also peaks around 16 y.

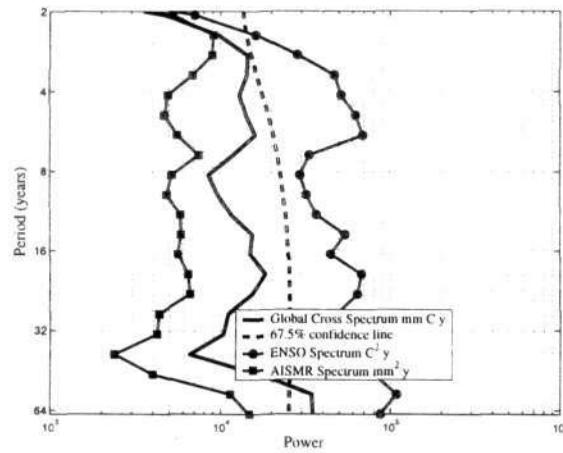


Figure 5.11. Global Wavelet cross power spectrum of ENSO index with AISM rainfall, dashed lines mark regions where the global cross spectrum exceeds the reference spectrum at 67.5% confidence levels.

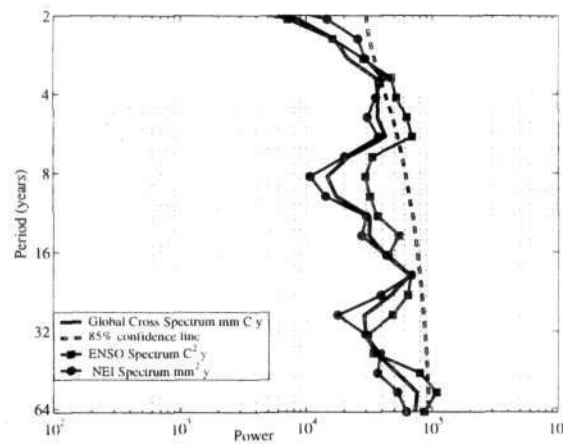


Figure 5.12. Global Wavelet cross power spectrum between ENSO index and NEI rainfall, dashed lines mark regions where the global cross spectrum exceeds the reference spectrum at 85% confidence levels.

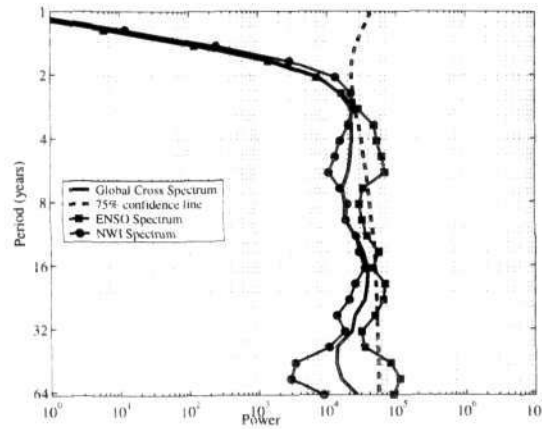


Figure 5.13. Global Wavelet cross power spectrum between ENSO index and NWI rainfall, dashed lines mark regions where the global cross spectrum exceeds the reference spectrum at 75% confidence levels.

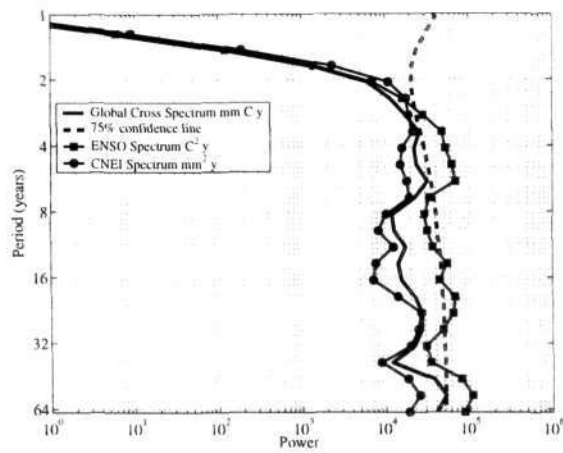


Figure 5.14. Global Wavelet cross power spectrum between ENSO index and CNEI rainfall, dashed lines mark regions where the global cross spectrum exceeds the reference spectrum at 75% confidence levels.

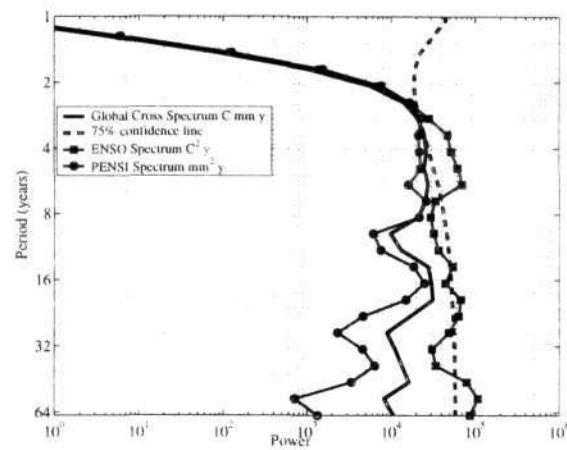


Figure 5.15. Global Wavelet cross power spectrum between ENSO index and PENSJ rainfall, dashed lines mark regions where the global cross spectrum exceeds the reference spectrum at 75% confidence levels.

5.5 Results for ENSO index and solar activity

Now we look at the wavelet cross spectra between the ENSO index and solar activity indicators. For the present we study the cross spectra with sunspot numbers and solar irradiance time series. Figure 5.15 (top panel) shows the cross spectrum between ENSO and sunspot number, with regions of 90% confidence spread over 4-8 y and 8-16 y period bands. Similarly the bottom panel of the figure shows the cross spectrum between ENSO and solar irradiance time series over a longer time duration from 1850–1998. One of the two distinct pairs of contours lies over test period 1, and the other over the 1964–1990 period, both within the 8-16 y period band.

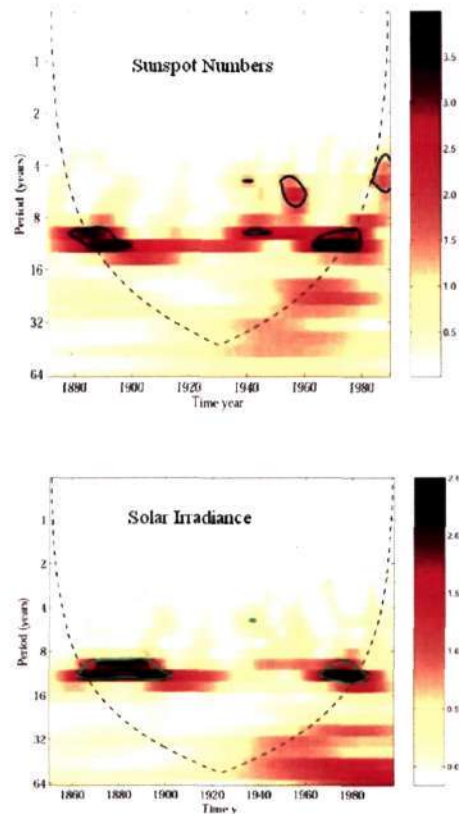


Figure 5.16. Wavelet cross power spectrum of ENSO index with sunspot number (top panel) and solar irradiance (bottom panel), blue thick contour mark regions where the cross spectrum exceeds the reference spectrum at 90% confidence level

The corresponding global cross spectrum in figure 5.17 shows a peak in the middle of the 8–16 y period band, where the cross spectrum exceeds the reference spectrum at 90% confidence.

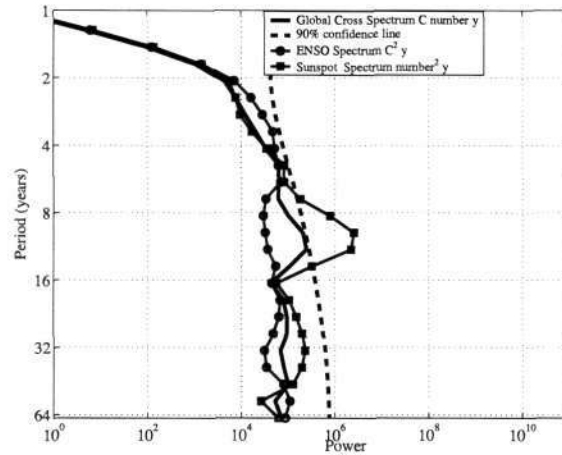


Figure 5.17. Global wavelet cross power spectrum between ENSO index and sunspot number, dashed line mark regions where the cross spectrum exceeds the reference spectrum at 90% confidence level

The global cross spectrum in figure 5.18 shows a peak in the middle of the 8–16 y period band where the cross spectrum exceeds the reference spectrum at 97.5% confidence.

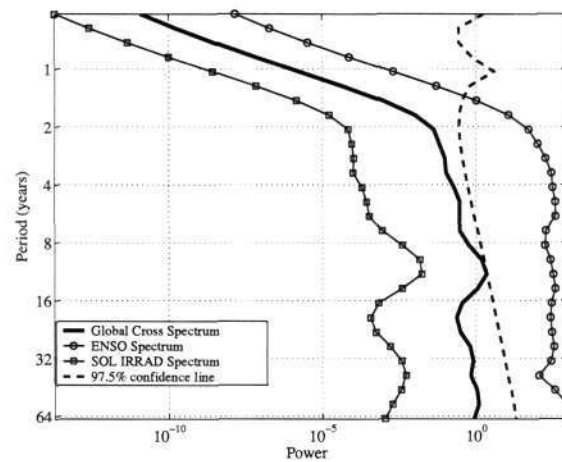


Figure 5.18. Global wavelet cross power spectrum between ENSO index and solar irradiance, dashed line mark regions where the cross spectrum exceeds the reference spectrum at 97.5% confidence level

The percentage contribution to the total wavelet cross power across all scales from individual period bands is shown in figure 5.19 for all the rainfall, solar activity and ENSO indices.

Table 5.5 shows the highest significance levels obtained in the cross spectral analysis presented in this chapter for each of the rainfall–sunspot number, rainfall–solar irradiance, ENSO–rainfall and ENSO–solar activity pairs. Column 1 lists the data, column 2 lists the highest

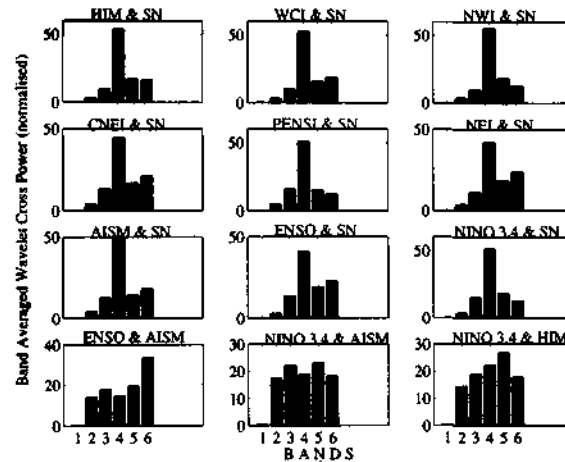


Figure 5.19. Wavelet cross power averaged over different period bands as percentages of the total wavelet cross power. Band (1): 1–2 y, (2): 2–4 y, (3): 4–8 y, (4): 8–16 y, (5): 16–32 y, (6): 32–64 y; the band limits are closed on the left and open in the right of the interval.

significance levels obtained in the wavelet cross spectrum, column 3 lists the duration over which the highest significance levels prevailed and column 4 lists the percentage confidence lines passed in the global cross spectrum in each case. It can be readily seen that the global significance levels for the rainfall–sunspot as well as ENSO–solar activity cases are higher than those for ENSO–rainfall cases.

Incidentally the present results demonstrate the advantages of the wavelet approach, as compared with classical correlation/power spectral density methods: (i) wavelets permit identification of epochs during which correlations at different significance levels may have prevailed; (ii) wavelet methods allow us to take account of slight variations in the effective period or scale ('meandering') of the effect of a given forcing, such meandering being presumably the result of the nonlinear interactions between different modes of the system.

Table 5.1. Highest significance levels obtained in cross spectra

Data	Significance level	Period	Global significance level
	Rainfall and	Sunspot Number	
HIM	99%	1940–1950	97.3%
WCI	99%	1940–1950	95%
NWI	99%	1935–1950	95%
CNEI	95%	1950–1970	90%
PENSI	90%	1943–1960	< 90%
NEI	90%	1940–1950	< 90%
	Rainfall and Solar	Irradiance	
AIMS	95%	1940–1950	95%
	ENSO and Rainfall		
HIM	95%	2–8 y	65%
WCI	95%	2–7 y	85%
NWI	95%	2–4 y, 16–24 y	95%
CNEI	95%	3–7 y	75%
PENSI	90%	3–7 y, 16–24 y	75%
NEI	95%	3–7 y, 16–24 y	85%
AIMS	95%	3–7 y	67.5%
	ENSO and	Solar Activity	
Sunspot Number	95%	4–16 y	90%
Sol. Irradiance	95%	8–16 y	97.5%

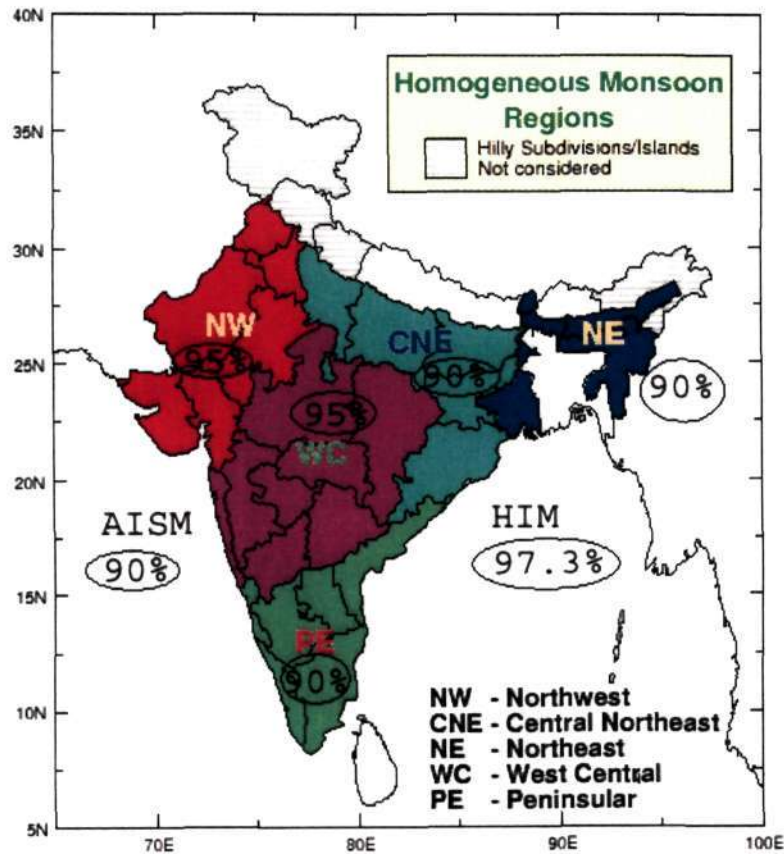


Figure 5.20. Homogeneous rainfall map of India showing percentage confidence levels at which the sunspot-rainfall global cross spectrum peaks.

5.6 Conclusions

- The Torrence–Compo test of statistical significance on the rainfall–solar activity wavelet cross spectrum reveals substantial cross power around the 11 y solar cycle period for all the indices considered. In particular the global cross power spectra for AISMR, WCI and HIM rainfall with the group sunspot number reveal a significant peak at the 11 year period at confidence levels of 95% or higher.
- Greater solar activity is associated in all cases with greater rainfall (this conclusion had also emerged earlier in Chapters 3 and 4, also see table 5.5), although at significance levels that are distinctly high in 3 and lower in 4 out of the 7 rainfall time series studied. This regional variation is consistent with the results mentioned in Chapters 1, 3 and 4.

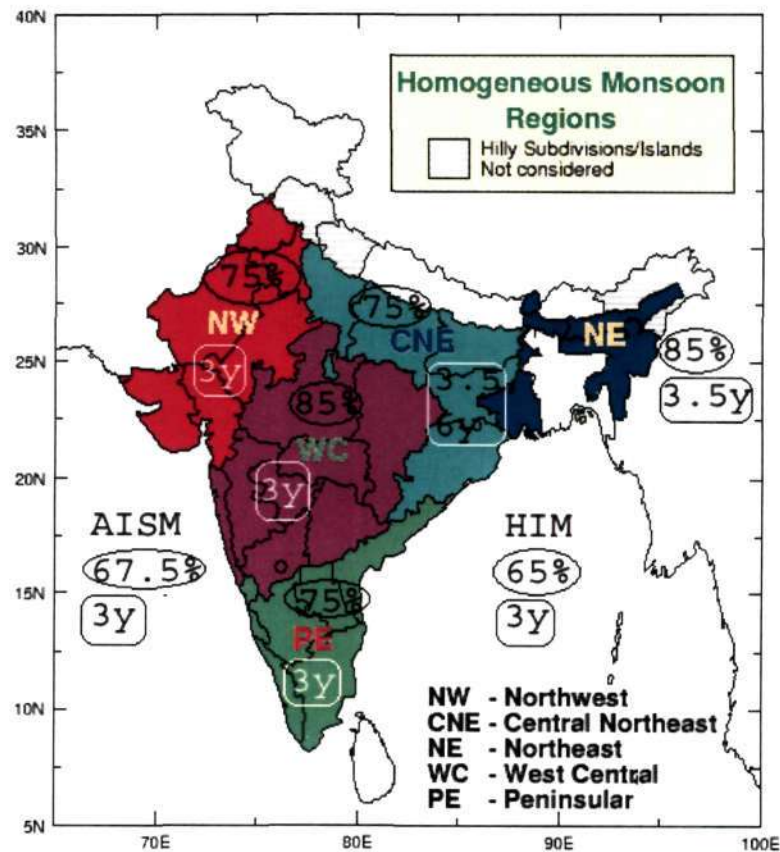


Figure 5.21. Homogeneous rainfall map of India showing percentage confidence levels as well as the period at which the ENSO-monsoon global cross spectrum peaks.

- On the ENSO-rainfall cross spectrum, the Torrence-Compo test reveals significant cross power spread over the 2–7 y period band across all the rainfall indices considered except for NWI where the 2–4 y band exhibits significant cross power. However, three regions (NEI, NWI and PENSI) have significant cross power also around the 16 y period, although parts of those regions were well within the cone of influence. However the global cross spectra for all the ENSO-rainfall indices were rather less significant, the confidence levels varying over the range 65% to 85%.
- Interestingly, the ENSO-solar activity cross spectra reveal considerable cross power in the 4–8 y and 8–16 y bands, the power over the first test period (1878–1913) being greater than over the second test period (1933-1964).
- The global cross spectrum for ENSO and solar activity index exhibits peaks at around the

11 y period at confidence levels of 90% or higher. In particular, the confidence level for the solar irradiance–ENSO index is as high as 97.5%. This indicates that there is a stronger connection between ENSO and solar activity as compared to that between ENSO and rainfall. Consistently with what is known in the case of rainfall, greater solar activity is associated with lower ENSO activity and vice-versa (see discussion in Chapter 1). This supports the results of Mehta and Lau (1997), Kodera (2004) and van Loon *et al.* (2004).

In the next chapter we evaluate the performance as well as limitations of the Torrence–Compo test with different ensembles of noise as test signals, and subsequently suggest an alternative statistical test which seems more appropriate to the problems on hand.

Wavelet Cross Spectral Analysis Of Rainfall Using Noise Test Signals

6.1 Introduction

We have reported in Chapters 3, 4, and 5 (see also Bhattacharyya and Narasimha (2005)) studies of the relations between solar activity and monsoon rainfall. These studies use an approach that differs from previous ones in selecting two test periods, each comprising three complete solar cycles, in which solar activity was consistently low and high respectively. By examining the monsoon rainfall in the 6 homogeneous zones identified by Parthasarathy *et al.* (1993), we found that rainfall is higher in the more solar-active period at confidence levels exceeding 75% in all 6 cases and 95% in 3 cases. On the rainfall–solar activity wavelet cross spectrum the Torrence–Compo test of statistical significance reveals significant cross power around the 11 y solar cycle period for all the indices considered.

In this chapter, the wavelet cross spectrum of the sunspot number and HIM rainfall is re-examined over the 120 y period 1871–1990 using Morlet continuous wavelets, in the context of a critical assesment of the Torrence-Compo test. The statistical significance of the computed cross-spectrum can in principle be estimated from the testing procedure outlined by Torrence and Compo (1998). It will be shown that this procedure suggests very high significance levels. This can be attributed to the use of a reference spectrum which utilises lag-1 and lag-2 auto-correlations of the signals being analysed. When one of these (solar activity in the present case) has a strong periodic component, the Torrence–Compo test is misleading. This is easily demonstrated by replacing the rainfall with white noise. For it turns out that the test suggests strong connections between white noise and sunspot numbers also. A new procedure is proposed here to overcome this limitation of the Torrence - Compo test. The principle behind the new procedure is to compare the cross spectrum under question with that between solar activity and three specially generated noise signals, one white and the other two simulating respectively the frequency spectrum and amplitude distribution of rainfall. The difference in solar–rainfall and solar–noise cross spectra can then be subjected to standard statistical tests to assess significance. The details of the above method and the results obtained therefrom are illustrated in

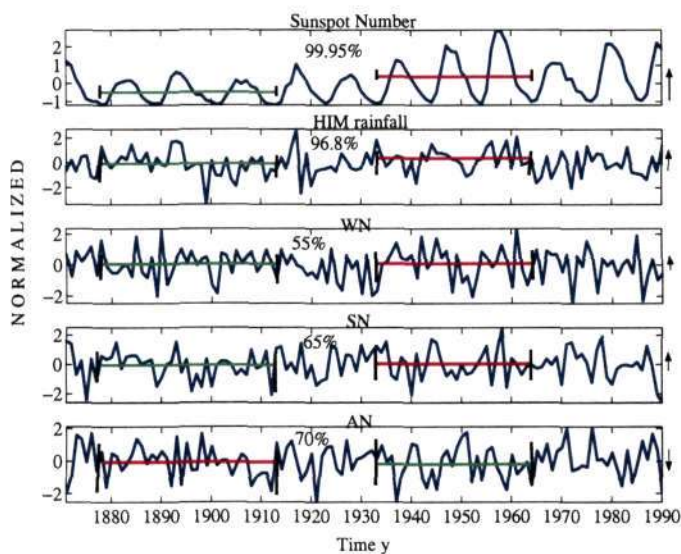


Figure 6.1. Time series of solar index, HIM rainfall and the three test signals for noise, indicating in each case the means over the test periods of low and high solar activity. The numbers marked in between the means indicate the percentage confidence levels at which the difference between means over the two periods is significant by the z -test.

the following sections.

6.2 Data Analysed and Methods Used

In this chapter we consider only HIM rainfall annual time series and one solar activity index, namely the yearly sunspot number. This should be adequate to illustrate the present approach. From the results in Chapters 3, 4 and 5 (see also Bhattacharyya and Narasimha (2005)) we know that the results would be a good representation of the links between solar activity and the southwest monsoon. The pattern of regional variation across India will be studied by the same method in the next chapter.

Three different synthetic noise signals are used as reference for comparison. The first is Gaussian white noise (WN). The second (SN) is generated to match the estimated power spectrum of HIM rainfall, using the spectral representation method of Grigoriu (1984). The third (AN) is generated from the probability distribution function of HIM rainfall using the stationary non-Gaussian translation process of Grigoriu (1998). The second algorithm is described in detail in the appendix 6A.

Figure 6.1 shows the normalized time series for sunspot number and HIM rainfall, and one (randomly selected) realization of each of the three noise time series. Figure 6.2 shows a comparison of the spectrum of SN and probability distribution of AN with the corresponding

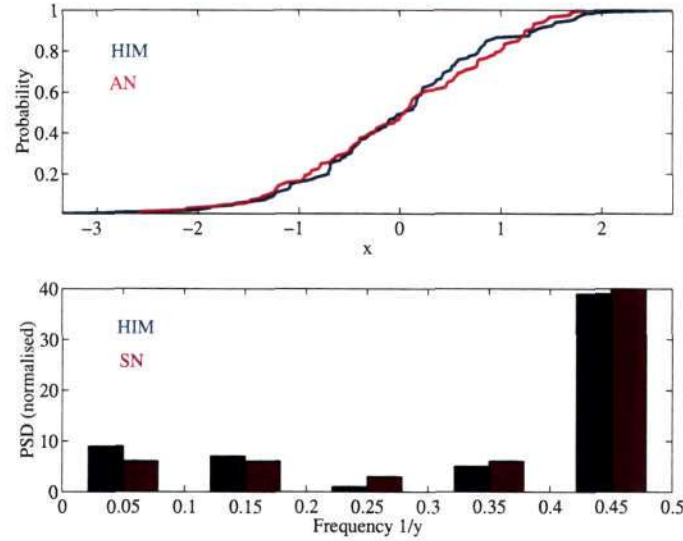


Figure 6.2. Comparison of probability distribution of AN and spectrum of SN with corresponding characteristics of HIM rainfall

characteristics of HIM rainfall. It is seen that the agreement is reasonable. All cross-spectra of rainfall with noise are computed over an ensemble of 1000 realizations of 120 samples each, and averaged. The size adopted for the ensemble was found to be large enough to yield robust estimates for the cross-spectrum, i.e. it can be taken as a reliable indicator of the cross-spectrum between white noise and sunspots. The computation of the wavelet cross spectrum and the Torrence–Compo test of statistical significance have already been described in Chapter 5.

6.3 Comparison between rainfall and noise cross-spectra

We compute the band averaged wavelet cross power which is defined as under.

6.3.1 Band Averaged Wavelet Cross Power

The band-averaged wavelet cross power $R_b^{RS}(t)$ is a weighted sum of the wavelet cross power spectrum over a given band of scales in the form proposed by Torrence and Compo (1998),

$$R_b^{RS}(t) = \frac{\delta j \delta t}{C_\delta} \sum_{j_1}^{j_2} \frac{|W_n^{RS}(s_j)|}{s_j}, \quad (6.1)$$

where $s_j = s_0 2^{j\delta j}$, $j = 0, 1, \dots, J$ and $J = \delta j^{-1} \log_2(N\delta t/s_0)$. We choose $\delta j = 0.25y$ in order to obtain a suitably fine resolution in scale (already mentioned in Chapter 4, section 4.2). The constant $C_\delta = 0.776$ is a scale-independent reconstruction factor for the Morlet function

(Torrence and Compo 1998).

Using the above formulations the cross power averaged over the bands 10-12 y, 9-13 y and 8-16 y are computed as functions of running time. These three bands, of progressively increasing width, are all centred around the well-known sunspot cycle with a period of about 11.6 y, and serve to allow for the variations noticed in the sunspot period (see discussion in Chapter 1 and Lassen and Christensen 1995). Over each of the two test periods of low and high solar activity comprising three complete solar cycles identified earlier in Chapter 3 of the thesis (see also Bhattacharyya and Narasimha 2005), namely 1878-1913 and 1933-1964, the band-averaged cross power $R_b^{RS}(t)$ between the rainfall and sunspot index, and those $R_b^{NS}(t)$ between each of the noise samples and sunspot index, are compared. The reason for confining attention to such test periods is to ensure that the statistical nonstationarity, that characterizes both rainfall and solar activity on longer time scales, does not affect the present analysis. (We may recall here that choosing two 5-cycle test periods did not alter the nature of the conclusions, but the confidence levels were lower (see Chapter 3, figure 3.6)). This comparison demands that we test whether differences between the band-averaged coefficients of different kinds are significant. Two quantities are relevant for the present investigation:

- the difference between rainfall and noise cross-spectra with sunspots, for any given period;
- the difference between rainfall and sunspot cross-spectra in the two test periods.

In either case, if \bar{R}_1 and \bar{R}_2 are the two cross-spectral measures under question, we form the z -test statistic

$$Z = \frac{(\bar{R}_1 - \bar{R}_2)}{\sqrt{[\text{var}(\bar{R}_1)/n_1 + \text{var}(\bar{R}_2)/n_2]}}, \quad (6.2)$$

where n_1, n_2 are the number of samples used to obtain the concerned averages. The z -test is adequate as we always have more than 30 samples in each case (see Crow *et al* 1960). The null hypothesis that there is no significant difference between the two means is rejected at confidence level $100(1 - \alpha)\%$ if $Z > z_\alpha$ for a one sided test against the alternative that the difference is greater than zero (see Crow *et al.* 1960).

6.4 Results

We first note that the contrast in solar activity between the two selected test periods is the highest that occurs during 1871-1990, the time interval over which reliable monsoon rainfall data are available (as already discussed in Chapter 3). Using the one-tailed z -test, the null hypothesis that the difference in the averages of the various time series (including the three noise signals) is zero over these two periods is rejected at the confidence levels marked in figure 6.1. In each panel, the averages of the respective quantities over these periods are marked in red

for the higher solar activity period (1933–1964) and in green for the lower solar activity period (1878–1913). It is seen that the mean annual HIM rainfall during 1933–64 is higher than that during the period 1878–1913 at a confidence level of 96.8% (confirming the results of Chapter 3). The confidence levels for the noise time series WN, SN and AN are respectively 55%, 65% and 70%, with the mean being slightly higher in the second test period for WN and SN and lower for AN. Over a larger number of realizations of 1000 samples, the confidence levels for the noise time series vary over the range 50 – 85%, the differences being either higher or lower between the two test periods at random.

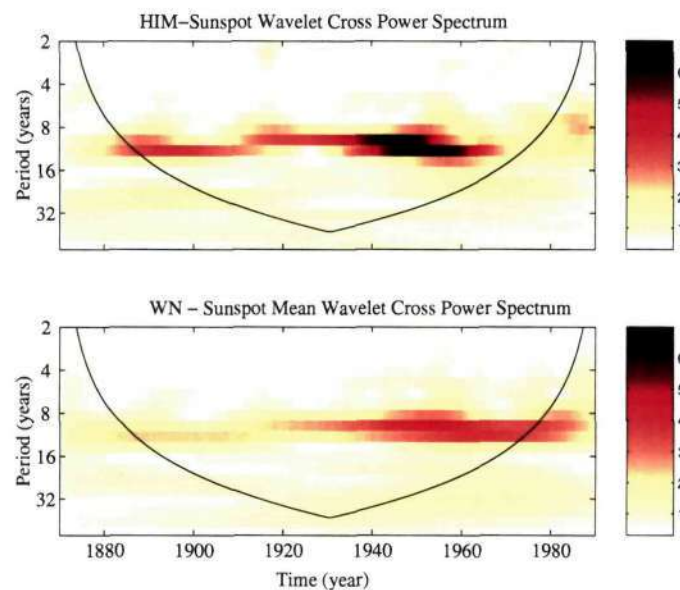


Figure 6.3. Wavelet cross power spectrum of HIM rainfall and sunspot number (top panel) and that between WN and sunspot number (bottom panel)

To investigate in greater detail whether there is indeed a significant difference between the association of solar activity index with rainfall as opposed to that with noise, we now present a wavelet cross spectral analysis of a solar activity index with rainfall and the noise signals. These take the form of colour-coded contour maps of wavelet cross spectra as functions of time and (Fourier) period, as shown in figure 6.3. The upper panel in figure 6.3 shows the wavelet cross spectrum of sunspot with HIM rainfall while the lower panel shows the same for sunspot and WN; both diagrams are drawn to the same scale to facilitate comparison. We recall that in the latter case, the cross spectrum shown is the mean over 1000 realizations of 120 samples each, and that 1000 realisations of noise are enough to represent the characteristics of the whole ensemble. In both cases, the maximum cross power is seen in the 8-16 year period band, particularly over the higher solar activity period. However the maximum power in the case of HIM-sunspot is

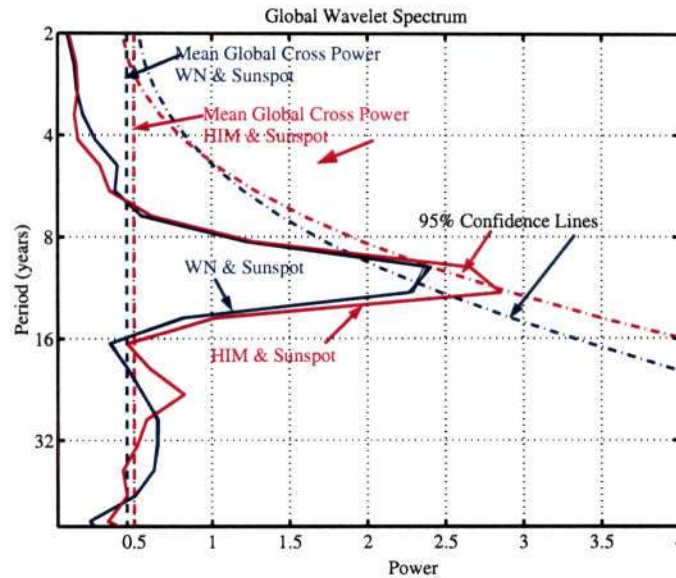


Figure 6.4. Global wavelet cross power spectra and confidence lines obtained from Torrence and Compo (1998) test.

approximately twice that in the case of WN–sunspot. The cones of influence within which edge effects become important are also indicated by solid black lines in figure 6.3.

The global wavelet cross power spectrum, already introduced in Chapter 5, is shown in figure 6.4 for the two cases shown in figure 6.3. It is seen that both noise and rainfall curves closely resemble each other, and that both peak in the 8–16 y period band. Superposed on these curves are dotted lines showing the mean global cross power across the entire period axis. Following the Torrence–Compo test for the significance of the global wavelet cross spectrum against the reference red noise background spectrum (see equation (5.4)), the 95% confidence lines for both cases are also shown in figure 6.4. It is evident that the difference between the global cross spectra for the signal and the noise is small, both being statistically significant to greater than 95% confidence level according to the Torrence–Compo test. Furthermore, by the same test, the individual cross-spectra are significant at confidence levels of 98% and 93% for rainfall and WN respectively.

At first sight this result seems to contradict the conclusion from Figure 6.1. However such results indicate the limitations of the Torrence–Compo test procedure. The first limitation is connected with the definition of the cross-spectrum, which is dominated by the strong periodic component in the sunspot time series even when the other signal in the pair is noise. The second is due to the model underlying the red noise reference spectrum adopted for a nearly periodic signal like that of sunspot number. For a periodic signal, the autocorrelation function is also periodic. So the basic premise of modeling the red noise background spectrum using lag-1 and

lag-2 autocorrelations for a periodic signal with periods much longer than 1–2 y needs to be questioned. One option is to model the background spectra using the actual solar activity index spectrum. However, we propose a different method here that is found to be effective.

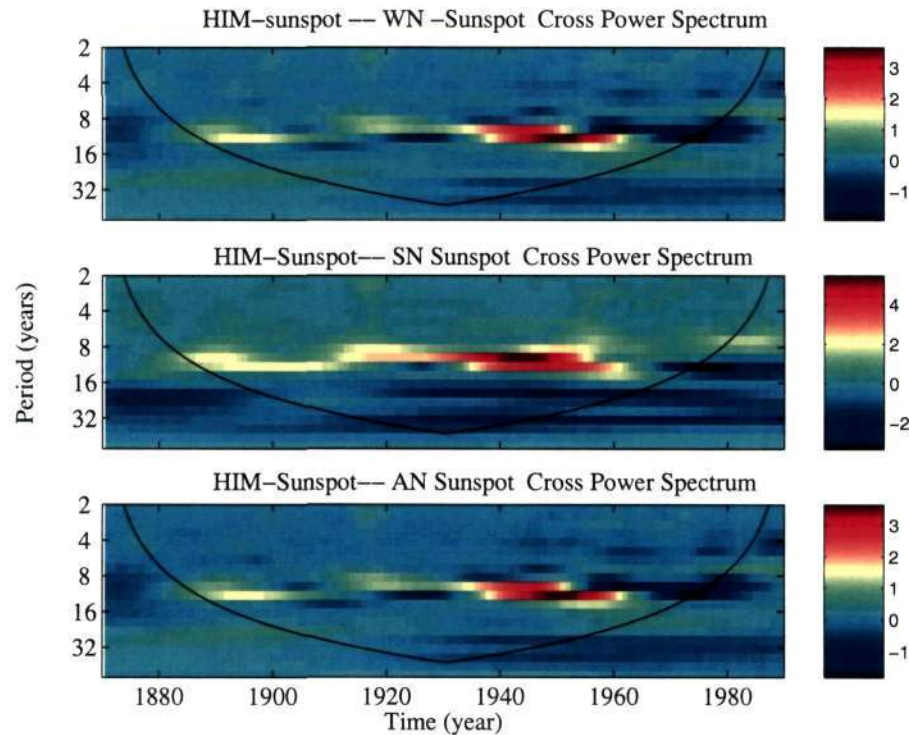


Figure 6.5. Difference between wavelet cross power of HIM-sunspot and (1) WN-sunspot (top panel), (2) SN-sunspot (middle panel), (3) AN-sunspot (bottom panel).

In this new method, the primary variable is the *difference* in the cross spectra between the HIM rainfall–sunspot number on the one hand, and those between sunspot number and WN, SN and AN respectively, on the other hand. The differences in the cross spectra are shown in figure 6.5. They range in all cases from small negative to larger positive values, the highest positive differences being in the test period 1933–1964 in the 8–16 y band in all three cases. We already know that although the sunspot cycle has a mean period of about 11.6 y, the solar cycle length can vary from 9–13 y (see discussion in Chapter 1). It may be noted that the value 11.6 y is close to the geometric mean of the ends of the 8–16 y band. For a more detailed analysis, we therefore choose three different bands, namely 8–16 y, 9–13 y and 10–12 y, over which to perform the statistical significance analysis on band-averaged cross power. Figure 6.6 shows the band-averaged wavelet cross power over the two test-periods for all four time-series pairs and all three period bands. It can be clearly seen that in each of the three bands, the highest cross-power is exhibited by HIM rainfall and sunspot number. Furthermore the differences between

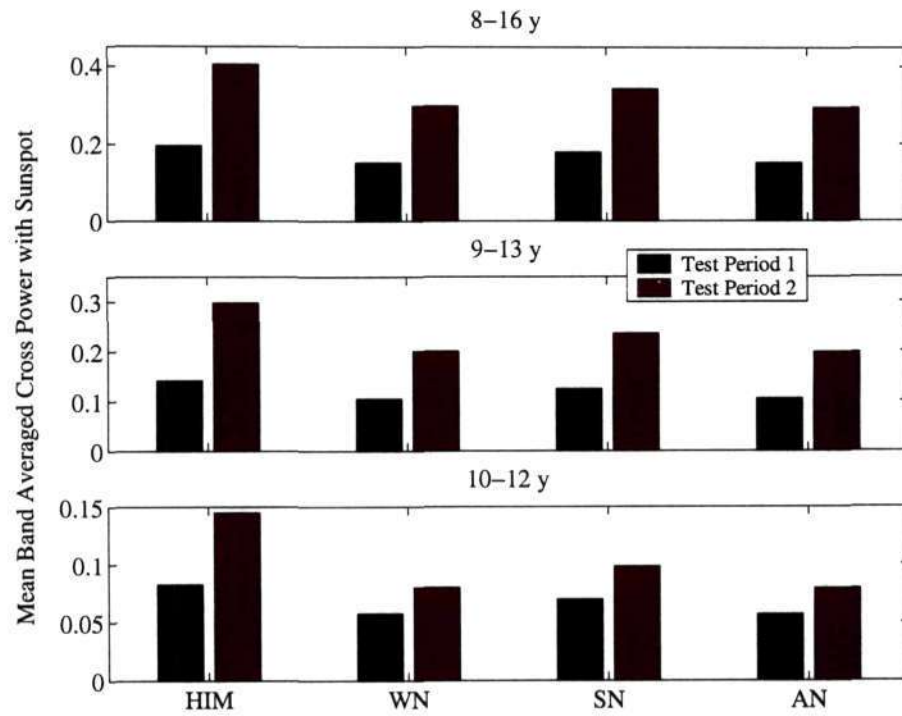


Figure 6.6. Wavelet cross power averaged over 8–16 y, 9–13 y and 10–12 y bands, with means in the two test periods.

the mean wavelet cross power of sunspot number with HIM rainfall and with the three noise time series WN, SN and AN respectively, over the two test periods, are tested for significance using the standard z -test. For all the cases $Z > z_\alpha$ for $\alpha = 0.0001$. In other words, the mean cross power between HIM and sunspots is greater than that between sunspots and noise WN, SN and AN respectively, at a confidence level greater than 99.99% in all the bands considered in this analysis.

6.5 Conclusions

The present chapter outlines a statistical comparison of the cross spectra of a solar activity index with HIM rainfall and with three noise signals respectively. The noise signals include those matching the spectrum and the probability distribution function of the rainfall time series. It is found that over two test-periods respectively of high and low solar activity, each comprising three complete solar cycles, the average cross power for rainfall and solar activity index exceeds that between noise and solar activity index at confidence levels of 99.99% or higher in each of the 8–16 y, 9–13 y and 10–12 y bands using the z -test. Furthermore we reconfirm that the HIM rainfall in the higher solar activity period (test period 2) exceeds that in the lower solar activity

period (test period 1) at a confidence level of 96.8%. The evidence for connections between HIM rainfall and solar activity thus appears to be strong.

Rainfall from all the other homogeneous regions are now subjected to this analysis and comparison with the test signals and the results therefrom are presented in the following chapter.

Appendix 6 A

Simulating test signals

The white noise is generated using the standard MATLAB command 'randn' which provides realisations of Gaussian random variables with mean 0 and variance 1. It was found that 1000 realisations of 120 samples each of these Gaussian random variables represented the ensemble characteristics adequately and are used to form the noise ensemble.

With target spectrum

The target spectrum for the simulation of the SN ensemble is the Fourier spectrum of the rainfall signal under consideration. The algorithm (due to Soong and Grigoriu (1993)) used for this is as follows:

- Step 1: Take the Fourier spectrum of the target signal (rainfall in this case), say $p_{RR}(\omega)$.
- Step 2: $\sigma = \sqrt{(2p_{RR}(\omega)d\omega)}$, where $d\omega$ is the frequency resolution.
- Step 3: For a selected value of $d\omega$, define the intervals $\Omega = [\omega - d\omega/2, \omega + d\omega/2]$ of width $d\omega$. This step constructs the array of frequencies to be generated in the simulated spectrum.
- Step 4: Let $R(t)$, of length N be a sample realisation of the signal to be simulated. Then $R(t) = \sigma [a \cos(\Omega t) + b \sin(\Omega t)]$, where a and b are vectors of Gaussian random variables of length N , and t is running time.

The above algorithm can be suitably run to generate as many realisations as desired.

With target PDF

For generating a signal with a desired (target) probability distribution function, first we derive the probability density function of the given signal. Next, we use this distribution function to suitably derive a memoryless transformation formula that maps normally distributed random variables to random variables possessing the desired probability distribution function. Details of the algorithm for this two-step process follow.

Let us model the time series as a random process $R(t)$ with probability density function $p_R(r)$, $a < r < b$, with specified mean m , bounds $[a, b]$ and variance σ^2 . According to the maximum entropy principle, given only partial information about a random variate, we should choose that probability density for it which is consistent with the given information, but otherwise has maximum uncertainty associated with it. To do this, first we find a family of density functions every member of which is consistent with the given information. Next, from this family, we choose that density function whose uncertainty or entropy is greater than that of any other member of the family.

Shannon's measure of uncertainty defines the entropy function of a probability distribution $p_R(r)$ to be

$$H(p_R(r)) = - \int_a^b p_R(r) \ln(p_R(r)) df, \quad a < f < b, \quad (6.3)$$

where $H(p_R(r))$ is a continuous, symmetric and strictly positive function. We now maximise the entropy function $H(p_R(r))$ subject to the constraints

$$\int_a^b p_R(r) df = 1 \quad (6.4)$$

$$\int_a^b f p_R(r) df = m \quad (6.5)$$

$$\int_a^b (f - m)^2 p_R(r) df = \sigma^2. \quad (6.6)$$

Now we solve the above problem using Lagrange's method of undetermined multipliers. The Lagrangian is then given by

$$L = \int_a^b g(p_R(r)) df \quad (6.7)$$

where

$$g(p_R(r)) = -p_R(r) \ln p_R(r) - \lambda_0 p_R(r) - \lambda_1 r p_R(r) - \lambda_2 (r - m)^2 p_R(r) + \lambda_0 + m \lambda_1 + \sigma^2 \lambda_2. \quad (6.8)$$

From the calculus of variations, it follows that for $\delta L = 0$, it is required that

$$\delta \left[\int_a^b g(p_R(r)) dr \right] = 0,$$

which in turn implies that $g(p_R(r))$ must satisfy the Euler-Lagrange equation

$$\frac{\partial g}{\partial p_R(r)} - \frac{\partial}{\partial r} \frac{\partial g}{\partial p_R(r)} = 0. \quad (6.9)$$

This simplifies to the final equation for the probability density function

$$p_R(r) = A \exp[-\lambda_1 r - \lambda_2 r^2], a < r < b, \quad (6.10)$$

where A, λ_1, λ_2 are constants to be determined from the constraint equations, which constitute a three-dimensional set of nonlinear simultaneous algebraic equations. They have to be solved using numerical techniques.

The last step involves integrating $p_R(r)$ to obtain the desired probability distribution function

$$\mathbf{R}(x) = \int_{-\infty}^x p_R(r) dr.$$

Let $Y(t)$ be a stationary Gaussian process with probability distribution Φ , zero mean and unit variance. Now if $R(t)$ is a real valued stationary non-Gaussian random process with specified probability distribution \mathbf{R} , then the process $R(t)$ can be expressed in terms of the process $Y(t)$ as a memoryless translation given by

$$R(t) = \mathbf{R}^{-1}[\Phi[Y(t)]] = G[Y(t)] \quad (6.11)$$

in which G is a real valued differentiable function defined on the real line. G is also assumed to be monotonically increasing. Such a non-Gaussian process $R(t)$, referred to as a translation process, constitutes a memoryless transformation G of a stationary Gaussian process $Y(t)$ (see Grigoriu 1984). The above equation can now be used for simulating the time series $R(t)$ with its desired probability distribution \mathbf{R} .

Spatial Analysis Of Cross Spectra

7.1 Introduction

Having analysed in Chapter 6 a comparison of the cross-spectra between sunspots on the one hand and HIM rainfall and appropriate reference noise signals on the other, we now perform the same analysis for all the other homogeneous rainfall regions of India. This enables us to learn more about not only the temporal but also the spatial variations among the different homogeneous regions. For each of the homogeneous regions, we first employ three ensembles of reference test signals, namely white noise (WN), noise simulating the rainfall spectrum (SN) and noise simulating the probability distribution of the rainfall time series under consideration (AN) (see Appendix 6A in the previous Chapter). Next we compute the ensembles of the cross spectrum of the sunspot number time series with ensembles of each of these test signals, and then test for the differences between each of these cross spectra and that between the original rainfall and sunspot number. The following sections present these results for each of the homogeneous regions and for AISM.

7.2 Results

The expressions for probability distribution and density functions obtained for each of the homogeneous rainfall time series using the above formulation are listed in tables 7.1 and 7.2. Table 7.3 gives the formula for simulating the spectrum and PDF matched noise signals for each homogeneous rainfall region.

Comparisons between the target PDF and the PDF of the simulated noise AN, for each of the homogeneous regions as well as for AISM, is shown in the top panels of figure 7.1. It is seen that the comparisons are reasonable. Each bottom panel of figure 7.1 shows the agreement between the target and the achieved spectrum of the simulated noise signal SN in the form of a bar diagram.

As an illustration of these test signals, samples of the three test signals for WCI, namely WN, SN and AN, along with the sunspot number and original WCI rainfall time series, are shown in figure 7.2. Marked on these panels are lines in red and green respectively showing the

Table 7.1. Probability density function of rainfall

Region	Probability Density
WCI	$p_{WCI}(r) = 0.39\exp(0.02r - 0.47r^2)$
NWI	$p_{NWI} = 0.39\exp(-0.01x - 0.48r^2)$
CNEI	$p_{CNEI} = 0.39\exp(-0.003 * r - 0.48 * r^2)$
NEI	$p_{NEI} = 0.39\exp(0.01 * r - 0.45 * r^2)$
PENSI	$p_{PENSI} = 0.38\exp(0.05 * r - 0.44 * r^2)$
AISM	$p_{AISM} = 0.37\exp(0.08 * r - 0.39 * r^2)$

Table 7.2. Probability distribution function of rainfall

Region	Probability Distribution
WCI	$R_{WCI} = 0.51\text{erf}(0.68r - 0.02) + 0.50$
NWI	$R_{NWI} = 0.50\text{erf}(0.69 * r + 0.01) + 0.50$
CNEI	$R_{CNEI} = 0.50\text{erf}(0.69r + 0.01) + 0.50$
NEI	$R_{NEI} = 0.51\text{erf}(0.67r - 0.01) + 0.50$
PENSI	$R_{PENSI} = 0.51\text{erf}(0.66r - 0.04) + 0.51$
AISM	$R_{AISM} = 0.53\text{erf}(0.63r - 0.07) + 0.52$

higher and lower mean over the two solar activity test periods. It is seen that the percentage confidence on the differences between the two means over the two test periods is high for the sunspot number (99.95%) and WCI rainfall (98.85%) time series, but much lower in case of all the noise signals (85%, 90% and 70% respectively for WN, SN and AN). Furthermore, the test signals often display trends opposite in phase to that of sunspot and WCI rainfall over the two test periods concerned (see the bottom panel in figure 7.2). The details of the simulated test signals for the other homogeneous regions and AISM are listed in table 7.4. ¹

Colour coded contour maps of the wavelet cross power spectrum between the sunspot number and all the homogeneous as well as AISM rainfall time series have already been presented in Chapter 5. For all these cases high cross power throughout the 8–16 y period band is observed, particularly over the second test period of 1933–1964. Figure 7.3 shows the global cross power spectrum between the sunspot number and actual rainfall in red as well as that between the test signal WN and the sunspot number in blue continuous lines for all the homogeneous region and AISM rainfall. Superposed on each one of them are the respective 95% confidence lines marked in dotted red and blue respectively. It can be seen that in both cases the global cross spectrum peaks in the middle of the 8–16 y band; although there are some differences between them in magnitude, both of them still pass the 95% confidence lines for WCI, NWI and AISM.

¹* Entries for the noise signals with $\mu_2 < \mu_1$ are shown with a star.

Table 7.3. Transformation function for simulating PDF matched noise signals for rainfall

Region	Rainfall simulating transformation
WCI	$r_{WCI} = (\text{erfinv}((0.89(\text{erf}(0.71y) + 1)/\sqrt{\pi} - 0.50)/0.51) + 0.016)/0.68$
NWI	$r_{NWI} = (\text{erfinv}((0.89(\text{erf}(0.71y) + 1.)/\sqrt{\pi} - 0.50)/0.50) - 0.01)/0.69$
CNEI	$r_{CNEI} = 1.44\text{erfinv}(1.76(\text{erf}(0.71y) + 1.)/\sqrt{\pi} - 0.99) - 0.02$
NEI	$r_{NEI} = 1.49\text{erfinv}(1.75(\text{erf}(0.71y) + 1.)/\sqrt{\pi} - 0.99) + 0.02$
PENSI	$r_{PENSI} = 1.51\text{erfinv}(1.73(\text{erf}(0.71y) + 1)/\pi^{1/2} - 0.99) + 0.06$
AIMS	$r_{AIMS} = 1.60\text{erfinv}(1.68(\text{erf}(0.71y) + 1)/\sqrt{\pi} - 0.99) + 0.11$

Table 7.4. Confidence level from z test for rainfall, and test signals WN, SN, AN

Data	Criterion	z -stat using the z -test			
		Actual Rainfall	WN	SN	AN
HIM	$\mu_2 > \mu_1$	96.8%	55%	65%	70%*
WCI	$\mu_2 > \mu_1$	98.85%	85%	90%	70%*
NWI	$\mu_2 > \mu_1$	75%	75%	55%*	65%*
CNEI	$\mu_2 > \mu_1$	85%	65%	55%	70%*
NEI	$\mu_2 > \mu_1$	75%	65%*	50%*	65%*
PENSI	$\mu_2 > \mu_1$	85%	95%	85%*	70%*
AIMS	$\mu_2 > \mu_1$	90%	90%	50%	70%*

Although the global cross spectra for the rainfall–sunspot lie below the 95% confidence line for CNEI, NEI and PENSI rainfall, the global cross spectra for WN–sunspot passes the 95% confidence line. From this it is evident that the Torrence–Compo (1998) significance test is not able to distinguish between the original time series and the noisy test signal in the cross spectrum. This has to do with the way the cross spectrum has been defined till now, as we have discussed in chapter 5. If the widely used Torrence–Compo test is applied to the cross spectrum as currently defined, it can quite often show spuriously significant connections (as with noise) at high confidence levels. This must be considered as a failure of the Torrence–Compo testing procedure. This limitation of the Torrence–Compo test could also be attributed to the modeling of the strongly cyclic sunspot signal by a red noise background spectrum with an autoregressive model for the autocorrelation function. The Monte Carlo type of testing scheme that we proposed in the previous chapter, and carry out in this chapter as well, is intended precisely to overcome this problem.

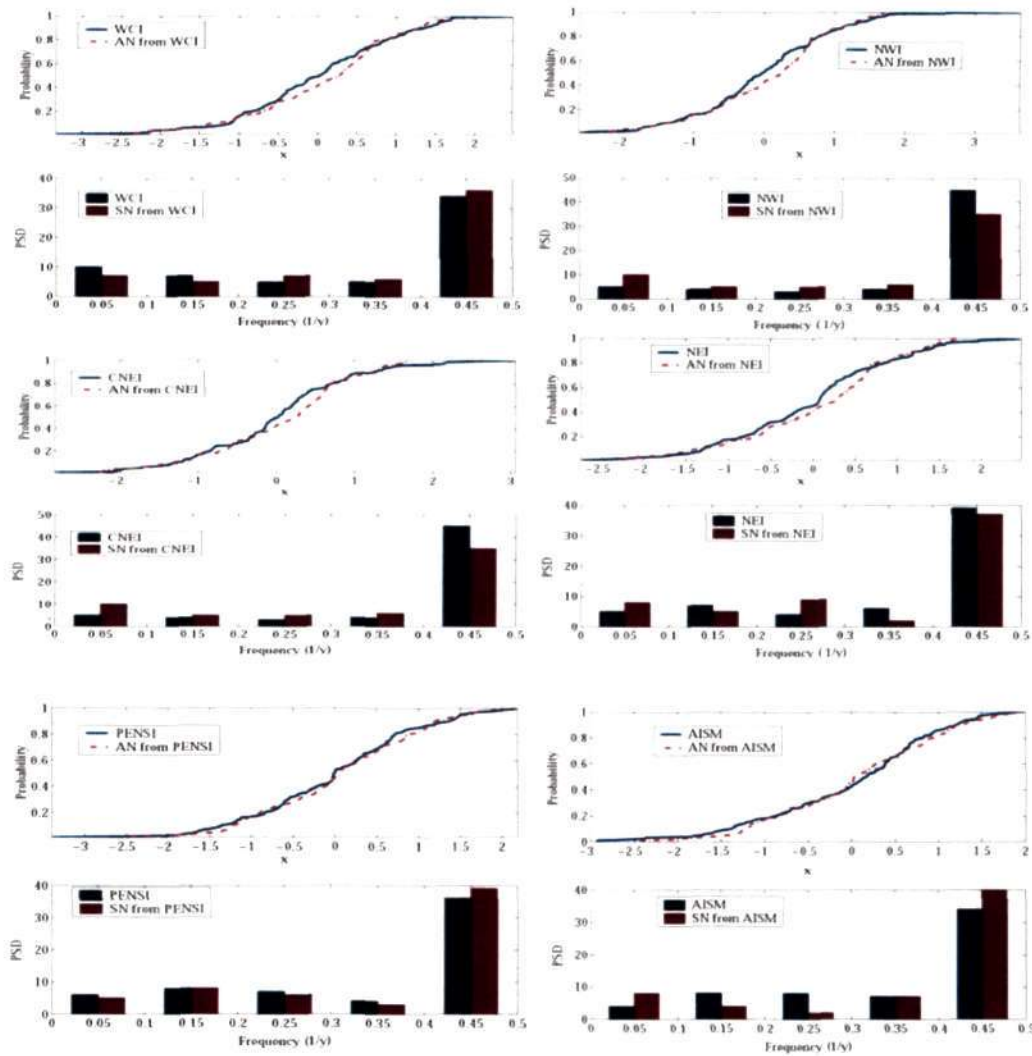


Figure 7.1. Comparison between PDF and Spectrum of target and simulated rainfall for five homogeneous regions and AISM.

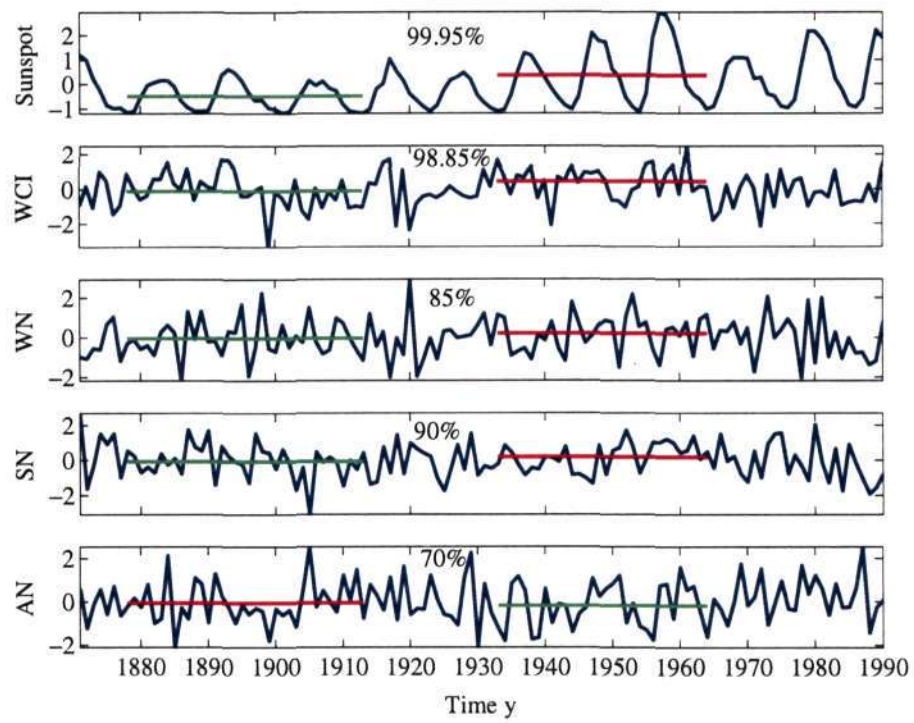


Figure 7.2. A sample of three test signals WN, SN, AN alongwith sunspot number and WCI rainfall.

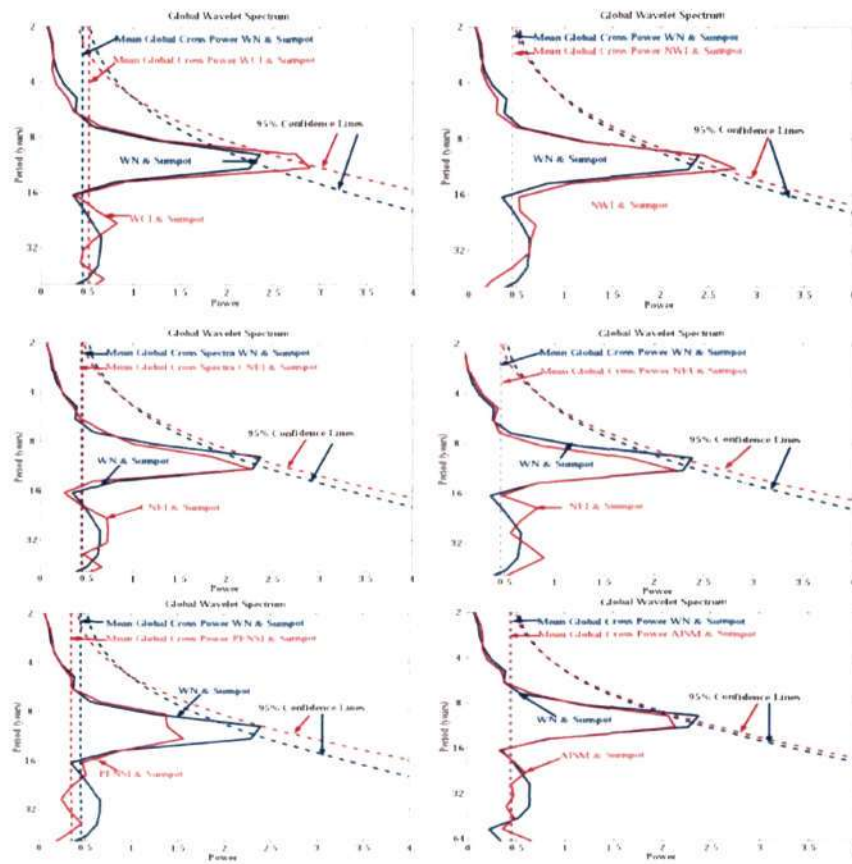


Figure 7.3. Global wavelet cross power spectra for rainfall-Sunspot and WN-Sunspot.

7.2.1 Noise Test Signal Approach

The principle behind our approach (as already discussed in the previous Chapter) is to take the cross spectrum between the sunspot numbers and noise as reference, and show how widely different the cross spectrum between rainfall and sunspots is, and use standard statistical tests to assess the significance of such differences.

The cross spectra between sunspot number and an ensemble of 1000 realisations of each of the test signals WN, SN and AN for the WCI case have been computed, and the mean cross spectrum in each case is shown in figure 7.4. It may be noted that while the cross power in these plots is concentrated again in the 8–16 y band, especially over the second test period, the magnitude of the normalised cross power in these cases is less than half that of the WCI–sunspot cross power. In figure 7.5 the difference between the WCI–sunspot cross power and the mean

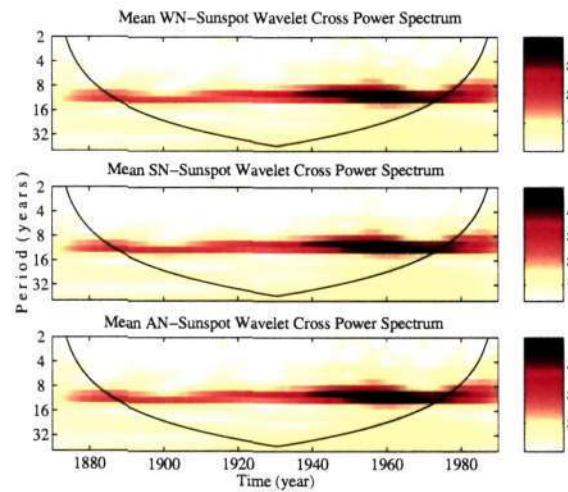


Figure 7.4. Mean Cross spectra of sunspot number with WN, SN and AN for WCI rainfall.

cross power between the three respective test signals and sunspot number is shown in the form of colour coded contour maps. Here dark blue shows small negative values (where the cross spectrum with the test signal exceeds that between WCI and sunspot) whereas comparatively larger positive values are shown in dark red. It is seen that the WCI–sunspot cross power far exceeds that between the test signals and sunspots. In the 8–16 y band, the differences in cross power between WCI and the test signals in their cross-spectra with sunspots are again higher in the second test period as compared to the first.

The mean cross spectra between sunspot number and an ensemble of 1000 realisations of each of the test signals WN, SN and AN for NWI are shown in figure 7.6. It may be noted that while the cross power in these plots are concentrated again in the 8–16 y band, especially over the second test period, the magnitude of the normalised cross power in these cases is less

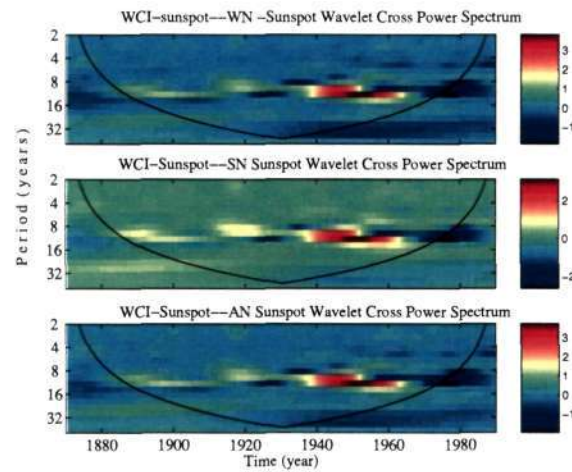


Figure 7.5. Difference between WCI-sunspot cross spectra and mean test signal–sunspot number cross spectra for each test signal.

than half that of the NWI–Sunspot cross power. In figure 7.6 the differences between the NWI–sunspot cross power and the mean cross power between the three respective test signals and sunspot number are shown. These differences in cross power between NWI and the test signals with sunspot are again higher in the second test period as compared to the first in the 8–16 y band.

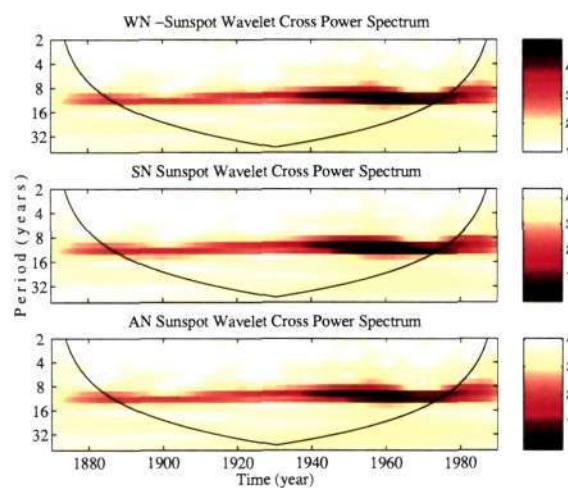


Figure 7.6. Mean Cross spectra of sunspot number with WN, SN and AN for NWI.

For CNEI rainfall, similar cross spectra are shown in figure 7.8. Again, while the cross power in these plots is concentrated in the 8–16 y period like the WCI and NWI cases, the magnitude

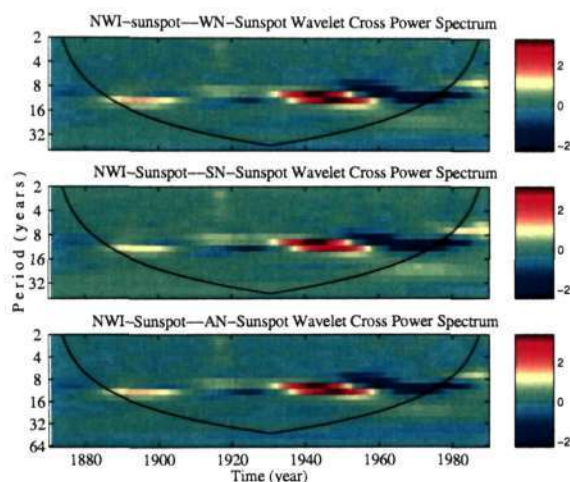


Figure 7.7. Difference between NWI-sunspot cross spectra and mean test signal–sunspot number cross spectra for each test signal.

of the normalised cross power for CNEI-noise cases is less than half that of the CNEI–sunspot case over the second test period. In figure 7.9 the difference between the CNEI–sunspot cross power and the mean cross power between the three respective test signals and sunspot number is shown. In the 8–16 y band, this difference is again higher in the second test period as compared to that in the first.

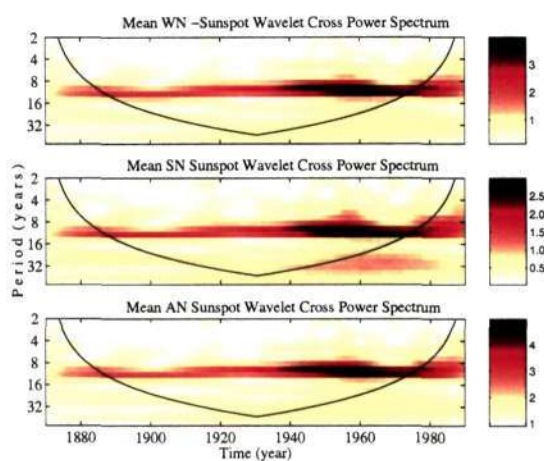


Figure 7.8. Mean Cross spectra of sunspot number with WN, SN and AN for CNEI.

For NEI rainfall, mean cross spectrum is shown in figure 7.10. Again the cross power in these plots is concentrated in the 8–16 y band, especially over the second test period. However, the magnitude of the normalised cross power in NEI-noise cases is nearly of the same order as that

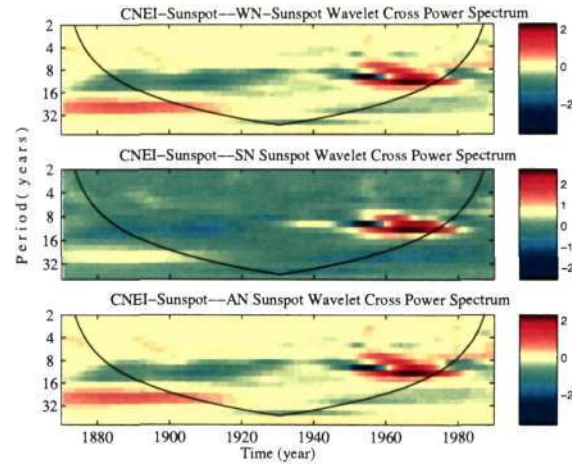


Figure 7.9. Difference between CNEI-sunspot cross spectra and mean test signal-sunspot number cross spectra for each test signal.

of the NEI-sunspot cross power. In figure 7.11 the differences between the NEI-sunspot cross power and the mean cross power between the three respective test signals and sunspot number are shown. These differences are again higher in the second test period as compared to the first in the 8–16 y band.

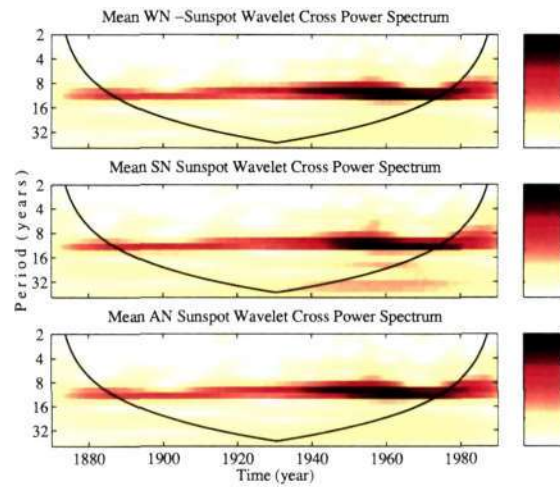


Figure 7.10. Mean Cross spectra of sunspot number with WN, SN and AN for NEI.

Similar cross spectra for PENSI rainfall are shown in figure 7.12. Over the second test period, the magnitude of the normalised cross power in PENSI-noise cases is of the same order as that of the PENSI-sunspot cross power, a result similar to the NEI case mentioned above. In figure 7.13 the differences between the PENSI-sunspot cross power and the mean cross power between

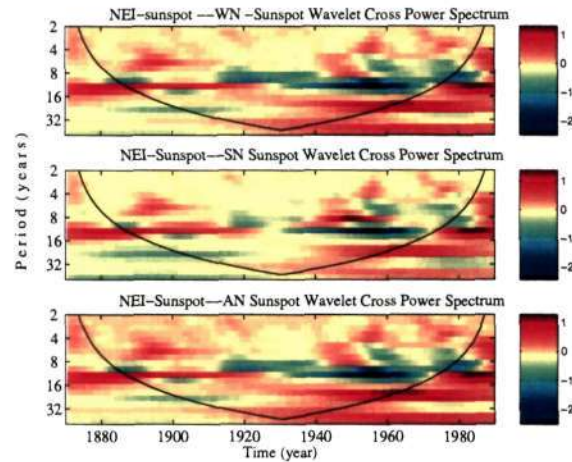


Figure 7.11. Difference between NEI-sunspot cross spectra and mean test signal–sunspot number cross spectra for each test signal.

the three respective test signals and sunspot number are shown. These differences are higher in the period 1920–1940 as compared to the first or second test period in the 8–16 y band.

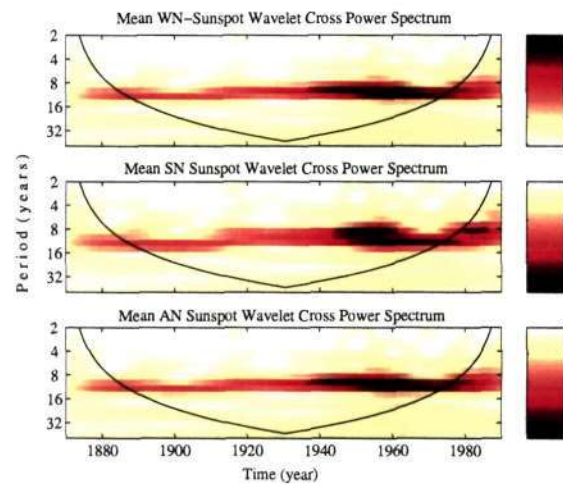


Figure 7.12. Mean Cross spectra of sunspot number with WN, SN and AN for PENSI.

For AISM rainfall (figure 7.14), the cross power is again concentrated in the 8–16 y period, especially over the second test period. The magnitude of the normalised cross power in these cases is a little less than that of the AISM–sunspot cross power. In figure 7.15 the differences between the AISM–sunspot cross power and the mean cross power between the three respective test signals and sunspot number are shown. It may be seen that the cross spectra with the test signals exceed that between AISM and sunspot to comparatively large negative values (shown in

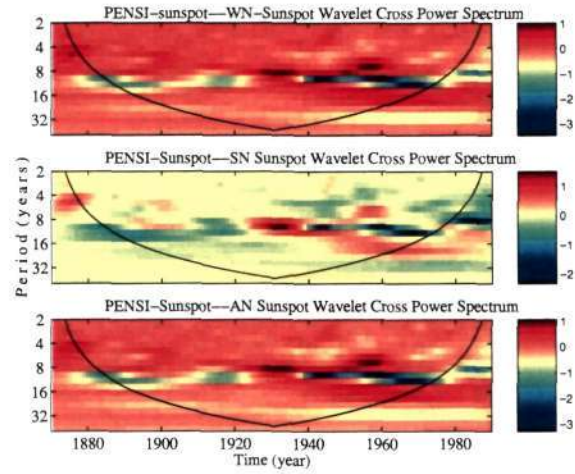


Figure 7.13. Difference between PENSI-sunspot cross spectra and mean test signal–sunspot number cross spectra for each test signal.

dark blue), the AISM-sunspot cross power exceeds those between the test signals and sunspots to small positive values shown in red. These differences in cross power between AISM and the test signals with sunspot are again higher in the second test period as compared to the first in the 8–16 y band.

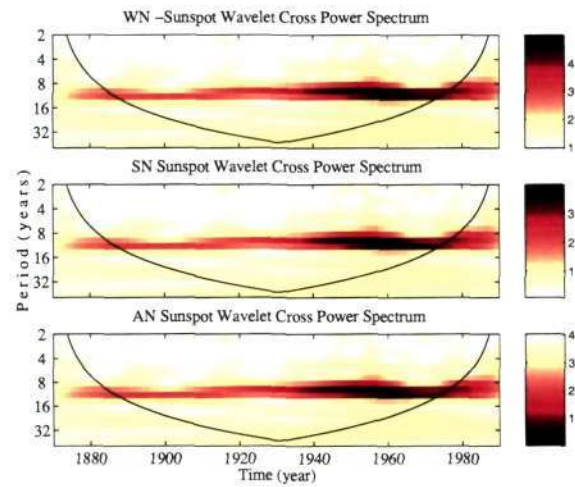


Figure 7.14. Mean Cross spectra of sunspot number with WN, SN and AN for AISM.

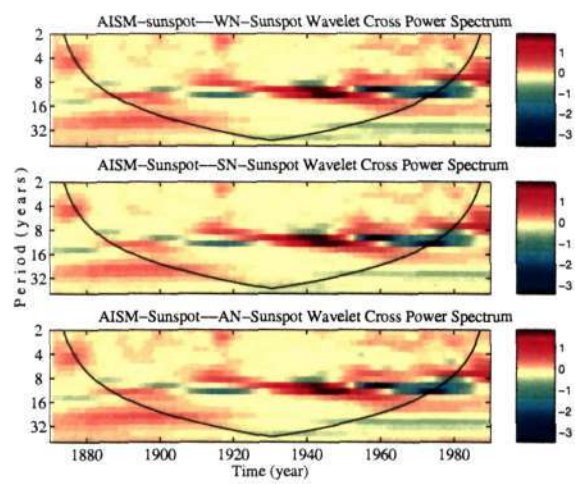


Figure 7.15. Difference between AISM-sunspot cross spectra and mean test signal-sunspot number cross spectra for each test signal.

7.2.2 Band Averaged Cross Power

Next we study the band-averaged cross spectra over the three bands 8–16 y, 9–13 y and 10–12 y, all covering the basic sunspot period of 11.6 y. We now compare the differences of the rainfall–sunspot cross spectra with each of the three test signal–sunspot cross spectra over each of the two test periods using the standard z -test. The results are shown in figure 7.16. The means of the band averages over both the test periods in all these figures are marked in red for the rainfall-sunspot case and in blue, black and cyan respectively for the WN, SN and AN – sunspot cross power. The observations from the band averaged cross power are listed below:

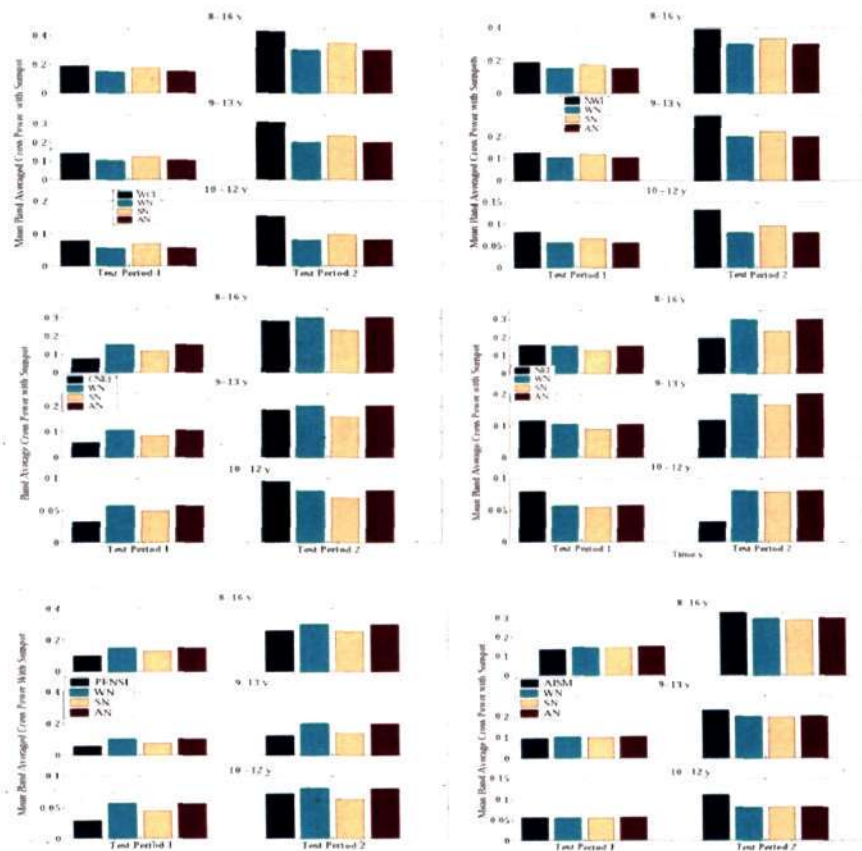


Figure 7.16. 9–13, 8–16 and 10–12 y band averaged wavelet cross power of rainfall and the test signals with sunspot number with means marked over the two solar activity test periods for all homogeneous rainfall and AISM.

- It can be seen at a glance that the lines in red are distinctly higher than the rest of the lines, indicating that the WCI-sunspot and CNEI-sunspot band averaged cross power are

always significantly higher than those for all the test signal-sunspot cases, particularly over the second test period.

- Over both test periods, the means for the NWI rainfall-sunspot are far greater than those for the test signal-sunspot cases.
- NEI-sunspot band averaged cross power is always significantly higher than those for all the test signal-sunspot cases, particularly over the first test period. Over the second test period, the scenario is in fact reversed. The red lines are distinctly lower than all the other lines for all the bands during the second test period. This implies that there is an inherent phase difference between NEI on the one hand, and HIM, WCI, NWI, and to some extent even CNEI, on the other. We shall see in the next chapter that NEI has a phase similar to that of the ENSO, El Nino and Nino 3 SST when we subject them to an identical analysis.
- The differences between PENSI and the test signals in their cross power with sunspots are higher in the period 1920–1940 as compared to either the first or the second test period in the 8–16 y band. For the 9–13 y band averaged wavelet cross power, the PENSI-sunspot case has lower values as compared to the test signal-sunspot cases, although the mean cross power over the second test period is higher than that over the first test period for all the time series considered in this case. For the 10–12 y band averaged cross power between PENSI and sunspots the results are identical to the NEI case except for the fact that in this case the mean cross power over the second test period for the PENSI-sunspot case is higher than that for SN-sunspot case.
- Over both the test periods, the means for the AISM rainfall-sunspot are greater than those for the test signals-sunspot cases over the second test period, as in the case of HIM, but lower than the test signal cases for the first test period (unlike HIM).

7.3 Conclusion

From the graphs displayed in this chapter, it is clear that the results from the regions WCI, NWI and AISM are similar in nature while NEI is distinctly different from all of them. CNEI and PENSI have characteristics that are in between those of WCI and NEI.

Next we perform the above analysis to study the connections of El Nino sea surface temperature to that of Indian homogeneous monsoon rainfall and the solar activity.

Connection Between ENSO, Indian Rainfall And Solar Activity

8.1 Introduction

An important factor which is of much interest to the climate community is the phenomenon called El-Nino-Southern Oscillation (ENSO). Several studies (Torrence and Webster 1998b,1999 and the references therein) on the impact of ENSO on the Indian monsoon describe the temporal variability of the ENSO-monsoon interaction. These studies suggest that ENSO and Indian monsoon share an inverse phase relationship, so that during an ENSO-year, the monsoon rainfall is likely to be below normal. This inverse relationship between AISM and the SST anomalies over various regions of the Equatorial Pacific has been well known for many years (see Sikka 1980, Pant and Parthasarathy 1981, Angell 1981, Rasmusson and Carpenter 1983, Krishna Kumar *et al.* 1999). More recently, it has been found that the SST anomaly affects the AISM rainfall to a larger extent than the SSTs or the SST anomalies themselves (see e.g. Rajeevan *et al.* 2005). (The anomalies in SST over the months December, January and February are subtracted from those over the succeeding months March, April and May to get the SST anomaly relevant to the rainfall of the monsoon season beginning in May–June.) A positive SST Nino 3.4 anomaly represents a strong El Nino over the Pacific, which in turn results in weakening of the monsoon circulation over Asia. Similarly, a negative implies weakening of the El Nino over the Pacific and strengthening of the monsoon over Asia.

A study of the influence of solar irradiance on the AISM-ENSO relationship by Mehta and Lau (1997) reported that while solar irradiance and monsoon co-vary with nearly the same phase, solar irradiance covaries with Nino3 SST with opposite phase on multi-decadal time-scales. It may be noted that in their study, 42% and 30% of the total solar irradiance variance were explained by the multi-decadal and 11-year irradiance components respectively. Furthermore, their study also indicated the possibility that the multi-decadal irradiance component influences the monsoon more than the 11 year component does.

The multi-decadal variability of the ENSO-monsoon system, together with the insight gained by using wavelet techniques on the variability of the Indian monsoon (Kailas and Narasimha

2000, Narasimha and Kailas 2001) and its connection with solar activity (as described in previous chapters), serve to provide further motivation for the work presented in this chapter. This chapter includes an analysis of the association between indicators of ENSO including SST Nino 3.4 tendencies, solar activity and Indian monsoon rainfall, using the continuous wavelet transform with the Morlet wavelet function.

8.2 The data analysed

The set of data analysed includes the time series for global SST ENSO index, Nino 3 and Nino 3.4 SST anomalies and *tendencies*, the sunspot numbers, solar irradiance, AISM, and the six homogeneous region rainfall time series over the period 1871-1990. The time step used in each of these time series is a year. The data for AISM rainfall, solar irradiance and global ENSO index are available for the longer time period 1850-1998 from the same data source described in Chapter 2. For studies with Nino 3.4 tendencies, the analysis also spans over the period 1871-2000. For the rest of the data the time period over which the analysis is performed is 1871-1990. The details regarding source and the time-domain analysis of each of the above mentioned data sets have been already reported and illustrated in Chapters 2 and 3.

As already discussed in Chapter 1, to establish a long term relationship with climate indices, a longer data stretch of precise solar irradiance measurements is required, whereas presently such measurements have been available only since 1978. For reasons set out in Chapter 1, we use the standardised solar irradiance provided by Lean (2004) for the present analysis.

8.3 Wavelet Method of Analysis

We use the continuous transform with the Morlet wavelet function in two stages. First, appropriate statistical significance tests as outlined by Torrence and Compo (1998) are performed over the wavelet cross spectrum (see Chapters 4 and 5 and also Bhattacharyya and Narasimha 2005a,b). Next we compute the band-averaged wavelet power over 2-7y and 8-16y period bands, and compare their evolution over time for the different time series under consideration. In the sections to follow we illustrate the results obtained from this analysis.

8.4 Results

8.4.1 ENSO - Solar Activity - AISM Rainfall

A plot of the raw annual time series of AISM rainfall, the global ENSO index, the solar irradiance and the sunspot index under consideration is shown in figure 8.1. Although these time series have been shown earlier in Chapters 2 and 3, we show them here again for ready reference. Both rainfall and ENSO index data appear irregular and random, while the solar indicators

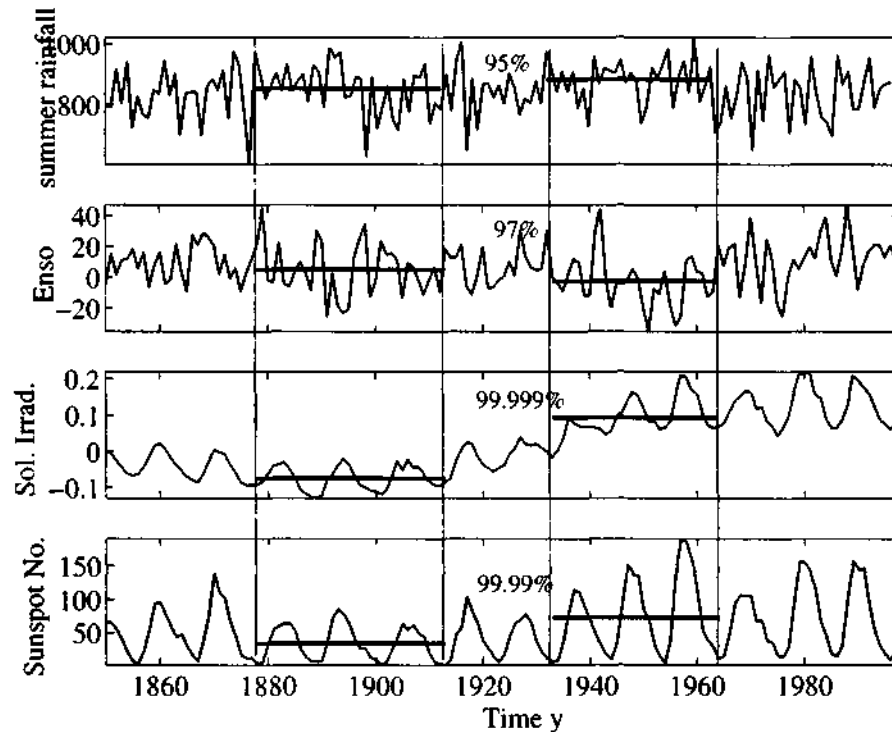


Figure 8.1. Raw time series of AISM rainfall in mm, ENSO index in hundredth of a degree Centigrade, solar irradiance in W/m^2 , and sunspot number, indicating epochs of low and high solar activity selected for analysis, and the means over the epochs for each parameter. The difference in means over the two test periods are significant at greater than 97%, 95%, 99.999% and 99.9% by the z -test, for AISM rainfall, ENSO index, solar irradiance and sunspot numbers respectively.

have a clearly cyclic character. In order to heighten the contrast, the same two test periods, already introduced in Chapters 2 and 3, namely 1878–1913 and 1933–1964, have been selected from the raw time series for the sunspot number. Superposed on each of the time series in thick lines are the values of the mean of the respective quantities over the two distinct test periods of solar activity. It is seen that, during the test period of lower solar activity, the mean rainfall is lower and the mean ENSO index higher, whereas during the test period of higher solar activity the mean rainfall is higher and the mean index is lower. A comparison of the mean rainfall, ENSO and solar activity over the two test-periods shows that mean rainfall and solar activity increase and the ENSO index decreases significantly from the first test period to the second, the difference in means being significant at confidence levels exceeding 97%, 95%, 99.999% and 99.9% respectively, for AISM rainfall, the ENSO index, the solar irradiance and the sunspot index by the z -test.

The results of the present analysis are displayed in the form of colour-coded contour maps (see

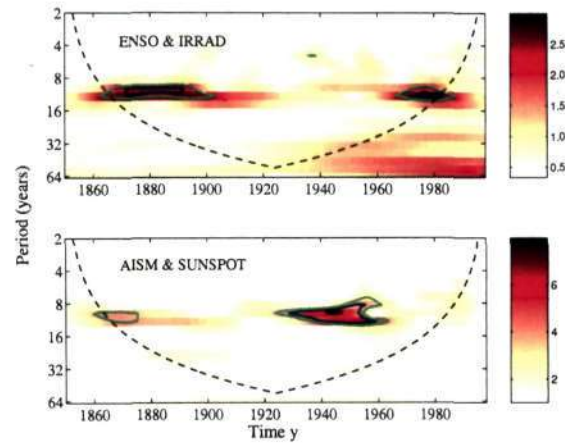


Figure 8.2. Wavelet cross power spectrum between ENSO index and solar irradiance (Top panel) and between sunspot number and AISM rainfall (Bottom panel). Contours in green, blue and black mark regions where the cross spectrum exceeds the reference spectrum at 90%, 95% and 99% confidence levels respectively.

figures 8.2 and 8.3) of wavelet cross power spectra as functions of time and (Fourier) period in a manner similar to the figures presented in Chapters 5, 6 and 7. Figure 8.2 (already shown earlier as figure 5.14 and reproduced here for ready reference) shows the wavelet cross power spectra between ENSO and solar irradiance (top panel) and between AISM rainfall and the sunspot numbers (bottom panel). The colour bars attached next to the figures show the minimum to maximum power in colours from white to red. Outlined on these graphs are contours enclosing regions where wavelet cross power is significantly higher, at 90%, 95% and 99% confidence levels (see figure 8.2) with respect to the reference spectra discussed in Chapter 5, equation 5.4. It is noticed that the highest power is in the 8-16 year period band in both cases, and that the powers are concentrated over the epochs of solar activity identified in figure 8.1, namely, 1878–1913 and 1933–1964. However, in the case of the cross spectrum between solar irradiance and ENSO, the higher power occurs over the period 1960-1990 in the 8–16 y band, as has also been noted in an independent study by Torrence and Webster (1999).

Figure 8.3 shows a similar set of plots but for the ENSO index and AISM rainfall (top panel) and for the ENSO index and sunspot numbers (bottom panel). From the top panel it is seen that significant power occurs in short stretches of time over the 2–7 y band, while the bottom panel shows significant power over a longer duration spanning the 4–16 y period band.

A comparison of the global wavelet cross power spectrum for all cases considered is shown in figure 8.4 (see also figure 5.15 and 5.16 showing cross spectrum between ENSO and solar activity parameters). A wavelet cross power of noticeably high magnitude is observed in the middle of the period range 8–16 years for all the cases considered except for that between ENSO

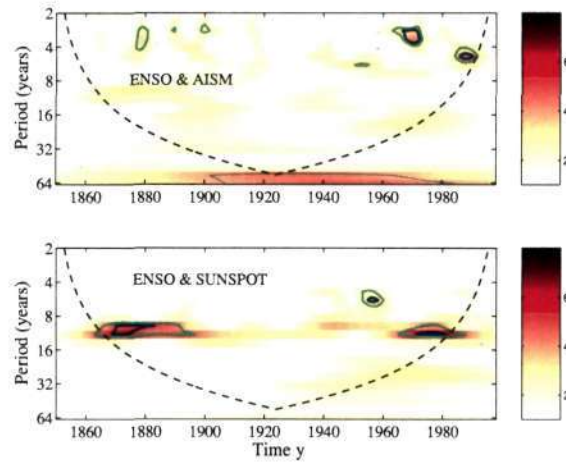


Figure 8.3. Wavelet cross power spectrum between ENSO index and AISM rainfall(Top panel) and between ENSO index and sunspot number (Bottom panel). Contours in green and blue mark regions where the cross spectrum exceeds the reference spectrum at 90% and 95% confidence levels respectively.

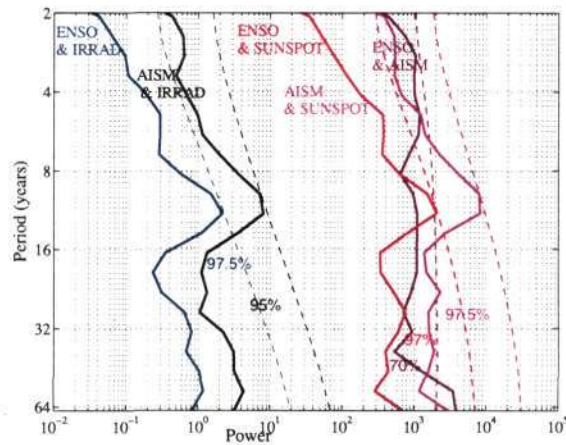


Figure 8.4. Global wavelet cross power spectrum between (a) ENSO index and solar irradiance marked in solid blue line, (b) AISM rainfall and solar irradiance in black, (c) ENSO index and sunspot number in orange, (d) AISM rainfall and sunspot in magenta, and (e) ENSO and AISM rainfall in purple. The corresponding dotted lines mark regions where the cross spectrum exceeds the reference spectrum at the confidence levels marked in the same order of colour. The % confidence levels crossed by each of the spectrum are given in the corresponding colours.

index and AISM rainfall. The ENSO-irradiance (shown in blue) and AISM-sunspot (shown in magenta) global wavelet cross power exhibit the highest significance levels (97.5%) in the 8–16 y period band, while ENSO-sunspot (shown in red) and AISM-irradiance (shown in black) reveal significant peaks in the 8-16 y band at 97% and 95% confidence levels respectively. The ENSO-AISM power (shown in purple) has the least significance (70%) and does not exhibit prominent peaks in the spectrum, although the amount of power in the cross spectrum is quite large.

8.4.2 ENSO-MONSOON

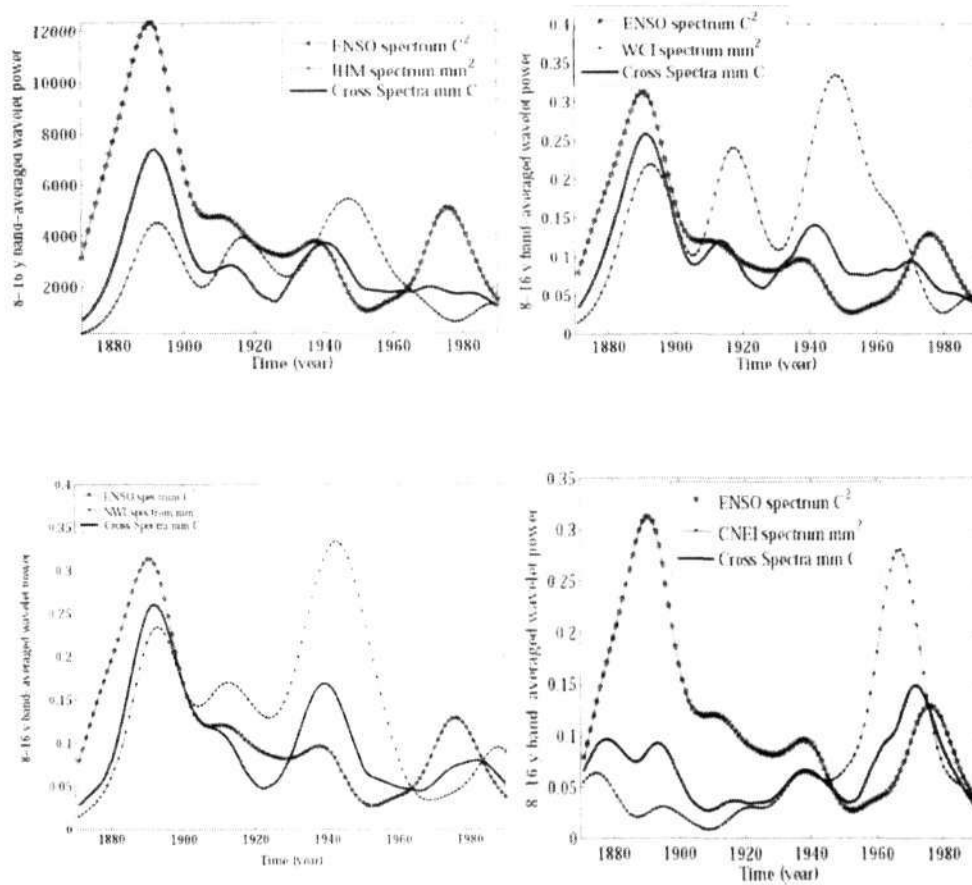


Figure 8.5. 8-16 y band averaged wavelet power and cross power between ENSO and HIM, WCI, NWI and CNEI rainfall

The ENSO-monsoon cross spectral analysis for the five homogeneous monsoon rainfall regions

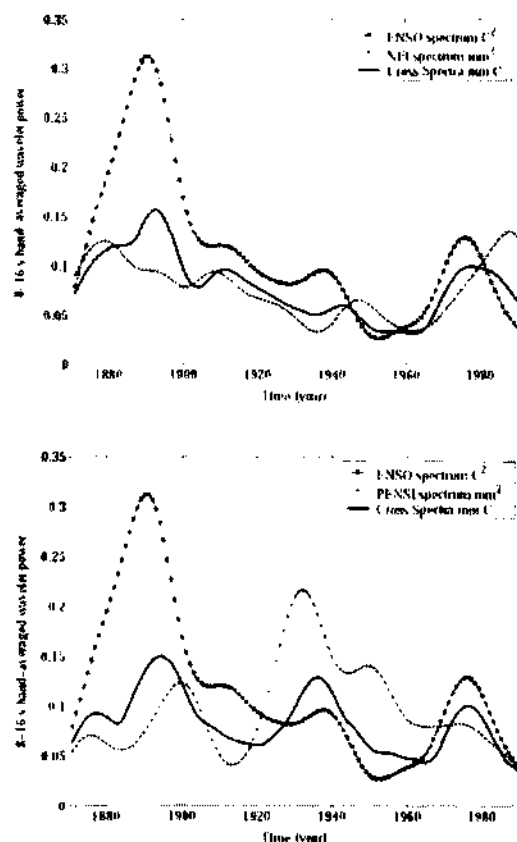


Figure 8.6. 8-16 y band averaged wavelet power and cross power between ENSO, and NEI and PENSI rainfall

as well as AISM rainfall have already been presented in Chapter 5, section 5.4. Figures 5.7-5.15 describe the results of wavelet cross spectrum and the global cross spectrum together with the confidence levels obtained using the Torrence-Compo test. Table 5.5 provides consolidated information on the highest significance levels obtained in different period bands for the ENSO-monsoon cross spectra corresponding to the different homogeneous rainfall regions. The 8-16 y band averaged ENSO-HIM cross spectrum (see figure 8.5, top left panel), shows higher (lower) cross power in the lower (higher) solar activity test period. The 8-16 y band averaged power for ENSO shows a similar trend whereas that for HIM shows the opposite trend. The WCI spectrum is similar to that of HIM, whereas the cross power of ENSO with WCI shows a trend similar to that of ENSO. The 8-16 y band averaged wavelet power for NWI shows higher power in the second test period as compared to the first, but the cross power shows an opposite trend, see figure 8.5 (bottom left panel). In the case of CNEI, the 8-16 y band averaged power

for ENSO is in nearly opposite phase to that for rainfall, and the band averaged cross power shows characteristics intermediate to those of the individual band averaged powers, see figure 8.5 (bottom right panel).

Figure 8.6 (top panel) shows the 8-16 y band averaged power for NEI. The power is higher over the first test period as compared to the second – a behaviour which is exactly opposite to that of HIM, WCI and NWI rainfall studied earlier in this section. The cross spectrum for NEI is consistent with the above observation on the 8-16 y band-averaged power. Figure 8.6 (bottom panel) shows the 8-16 y band averaged power for PENSI which shows lower power over both the test periods as compared to the transition period during 1920-1940 - a feature which is distinctly different from that for HIM, WCI, NWI on the one hand, and NEI rainfall on the other (both studied earlier in Chapter 5).

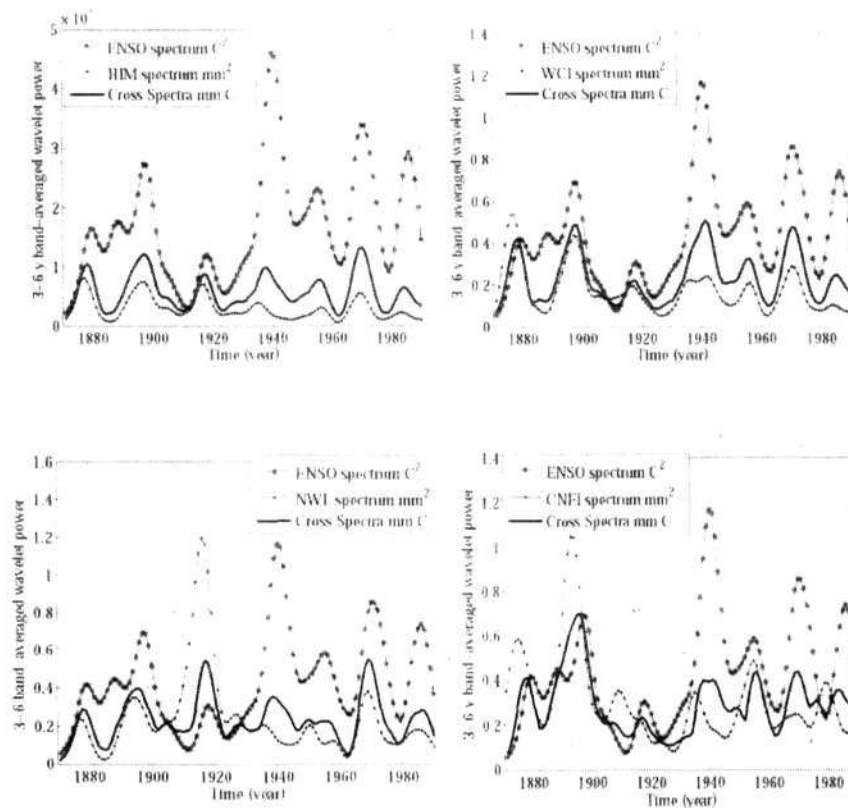


Figure 8.7. 3-6 y band averaged wavelet power and cross power between ENSO and HIM, WCI, NWI and CNEI rainfall

In the case of the 3-6 y band shown in figure 8.7 (top left panel), the plots are quite jittery in

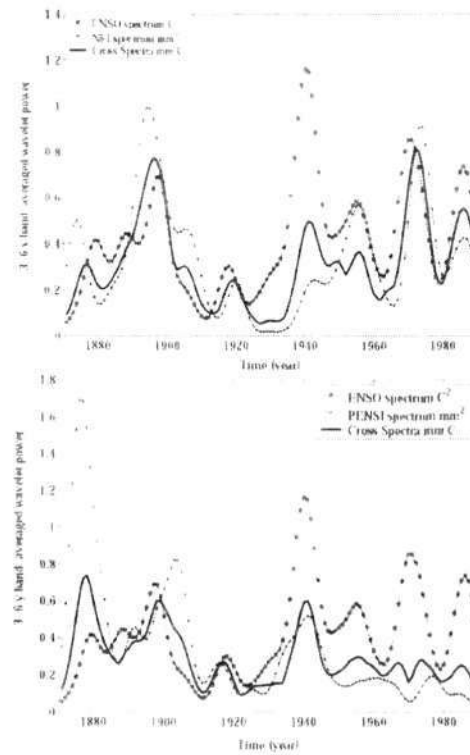


Figure 8.8. 3-6 y band averaged wavelet power and cross power between ENSO, and NEI and PENSI rainfall

the case of ENSO and HIM as well as the cross spectrum. However the trend for ENSO in the 3-6 y band is opposite to that seen in the 8-16 y band; on the other hand HIM does not show a prominent trend over the two test periods over the 3-6 y band. The cross-spectrum in 3-6 y band has characteristics in between those of the HIM and ENSO spectra in the same band. The 3-6 y band averaged power in figure 8.7 (top right panel) for ENSO shows lower power over the first test period and higher power over the second, while the WCI follows the reverse trend. The 3-6 y band averaged cross power in this case follows a trend intermediate to that of the individual ones. The 3-6 y band averaged wavelet power for NWI in figure 8.7 (bottom left panel) shows a peak over the transition period 1915-1925, whereas the cross spectrum shows features intermediate to those of the individual powers. In figure 8.7 (bottom right panel), the 3-6 y band averaged power for ENSO shows lower power over the first test period compared to the second, while the same for CNEI shows the opposite trend; however, the cross power between the two follows same trend as CNEI.

In the 3-6 y period band (see figure 8.8 top panel), the NEI exhibits higher power over the first test period as well as during the 1950-1990 stretch but lower power during the 1915-1950

period. The 3-6 y band averaged cross power shows characteristics in between the above two. In the same 3-6 y period band (see figure 8.8 bottom panel), PENSI exhibits higher power over the first test period as compared to the second, like the NEI case.

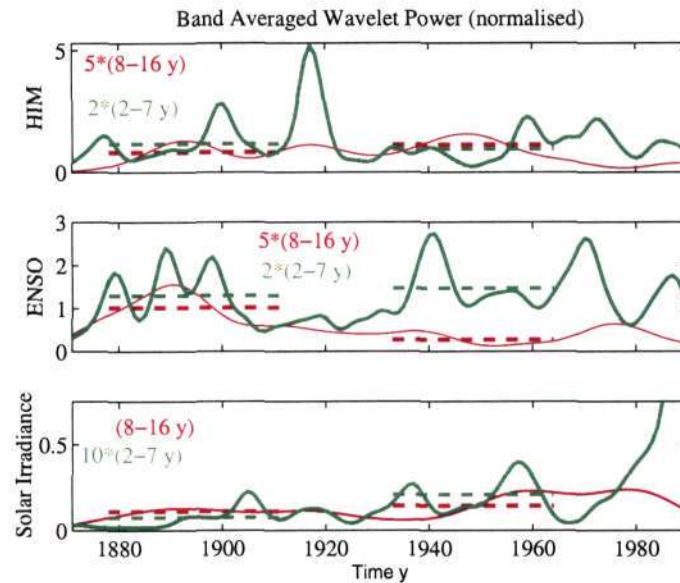


Figure 8.9. Band averaged wavelet power for ENSO and HIM rainfall and solar irradiance

Figure 8.9 shows a comparison between the 8-16 y and 2-7 y band averaged wavelet power for ENSO, HIM and solar irradiance. It is interesting to note that the 2-7 y band averaged ENSO power follows the same trend as the 8-16 y power for solar irradiance and HIM, whereas the 2-7 y band averaged power for HIM follows a trend opposite to that of its 8-16 y band-averaged power. We shall return to this question in section 8.5.

8.4.3 Results for connections between NINO 3.4, AISM, Solar Activity

In this section we present the results on the connections between Nino 3.4 SST, AISM, sunspot numbers and solar irradiance. The cross spectrum between Nino 3.4 and solar irradiance, as well as that between Nino 3.4 and sunspot number, are shown in the top and bottom panels of figure 8.10 respectively. In both cases the cross power is high in the 8-16 y period band. Figure 8.11 shows the cross spectrum between Nino3.4 SST and AISM having small contours of high power over the 3-8 y period band, but it also exhibits considerable power in the middle of the 8-16 y band over the period 1930-1950 and in the 16-32 y period band over the first test period. The global cross spectra of Nino 3.4 with AISM, sunspot number and solar irradiance, with the confidence lines plotted for respective cases, are shown in three vertical panels in figure 8.12. Figures 8.13 to 8.15 show respectively the 8-16 y and 3-6 y band averaged wavelet power for

the above three cases. It can be seen that in both the 8-16 y and 3-6 y bands, the Nino 3.4 is always out of phase with solar irradiance, sunspot and AISM rainfall.

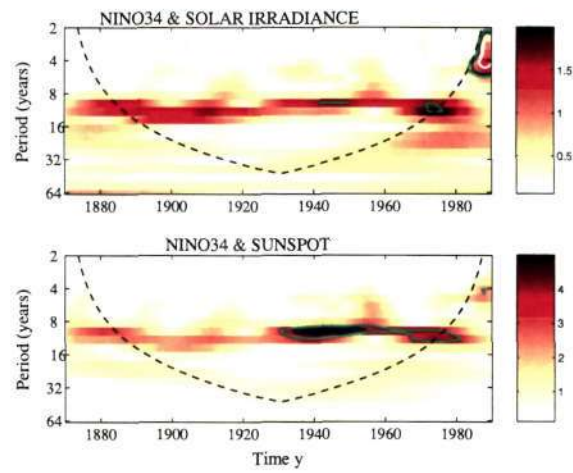


Figure 8.10. Wavelet cross power for Nino 3.4 with solar irradiance (top panel) and sunspot (bottom panel)

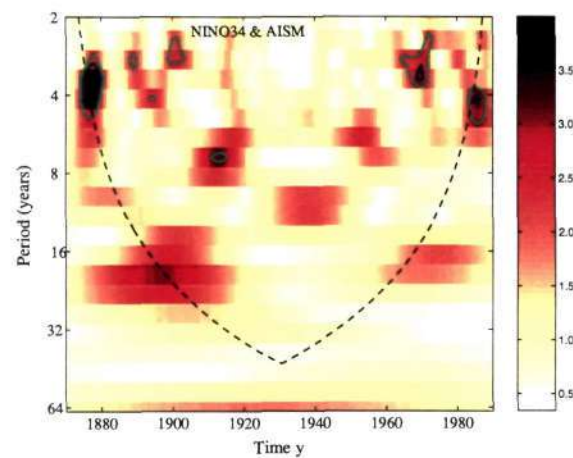


Figure 8.11. Wavelet cross power for Nino 3.4 with AISM rainfall

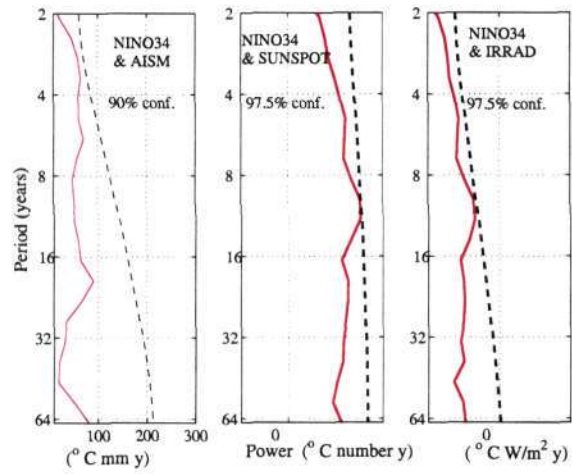


Figure 8.12. Global cross power for Nino 3.4 with AISM rainfall, solar irradiance and sunspot

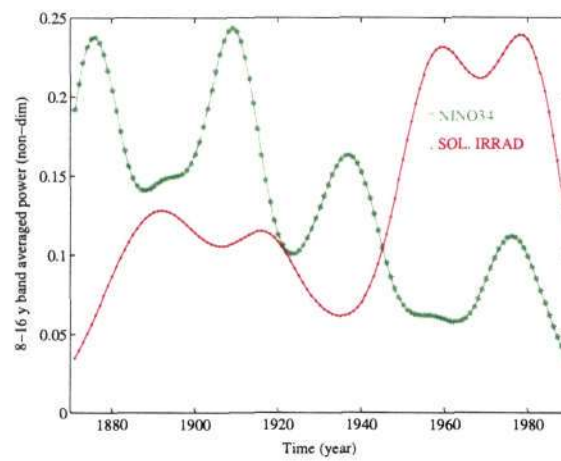


Figure 8.13. 8-16 y band averaged wavelet power for Nino 3.4 and solar irradiance.

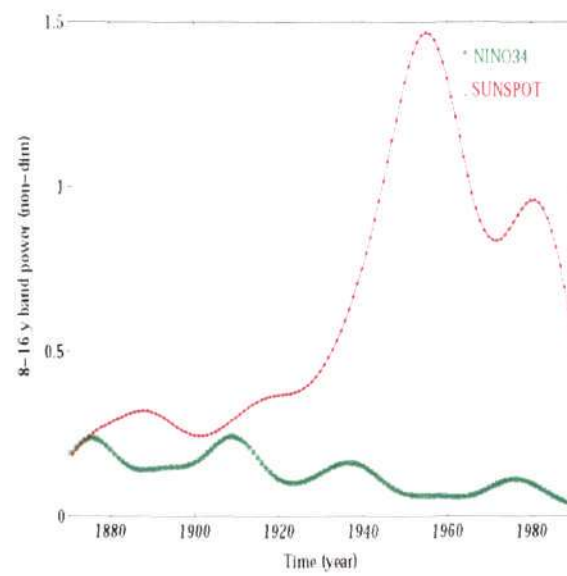


Figure 8.14. 8-16 y band averaged wavelet power for Nino 3.4 and sunspot.

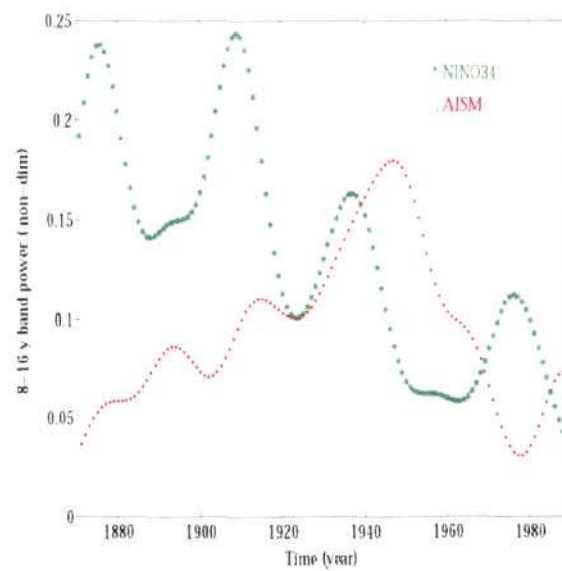


Figure 8.15. 8-16 y band averaged wavelet power for Nino 3.4 and AISM.

8.4.4 Results for Connections between Nino 3.4 Tendency, Rainfall and Solar Activity

We present here results on the connections of Nino 3.4 tendency with the Indian monsoon rainfall indices (AISM and all the homogeneous region time series) and with solar activity parameters.

Figure 8.16 shows the time series of Nino 3.4 tendency. Marked on the figure are means of the tendency respectively over the two test periods of higher (red) and lower (green) solar activity. The difference in the two means is significant to 80% by the z -test.

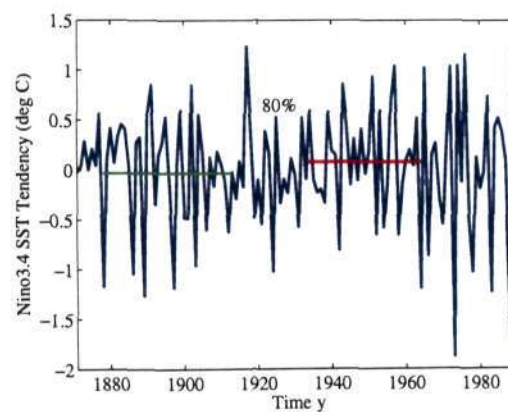


Figure 8.16. Time series for Nino 3.4 tendencies.

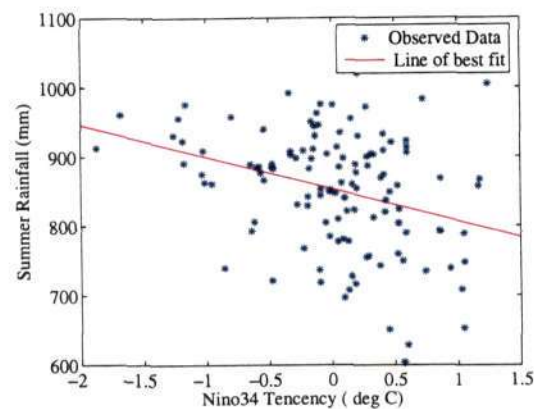


Figure 8.17. Scatter diagram of AISM rainfall against Nino 3.4 tendency time series.

Figure 8.17 shows a scatter diagram between the AISM rainfall and the Nino 3.4 tendency. The line of best fit marked on the figure shows a negative correlation between the two indices. The correlation coefficient is -0.33 at 99.9% confidence level, $[-0.52, -0.11]$ being the error

band at the same confidence level (which incidentally is higher than what is usually adopted). The correlation coefficient between the two for the period 1950-1990 turns out to be -0.44 at the 99.9% confidence level. This result agrees with Rajeevan *et al.* (2005).

The individual wavelet power spectra for Nino 3.4 tendency, AISM rainfall, sunspot number and solar irradiance time series are shown in figure 8.18 in four different panels. In the 2-6 y period band, Nino 3.4 SST tendency (top most panel) exhibits high power in the periods 1880-1906 (which is within the first test period of lower solar activity) and 1965-1990. Over the second test period of higher solar activity (1933-1964) there is lower power in the Nino 3.4 tendency. The AISM rainfall shows high power over the 2-6 y period band but considerable power also over the 8-32 y period band. In particular over the period 1955-1985 in the 2-8 y period band AISM shows substantial power, similar to the Nino 3.4 SST tendency. It seems that over the period 1965-1985, both rainfall and Nino 3.4 SST tendency show an increase in power, which is actually contrary to the well-known inverse relationship between the two. This result however agrees with the findings of Krishna Kumar *et al.* (1999) on the recent weakening of the ENSO-monsoon inverse relationship. In the two panels at the bottom, both sunspot numbers and solar irradiance show high power over the entire 8-16 y period band, although over the second test period (1933-1964) sunspot number shows higher power than the irradiance while over the period 1960-1990 irradiance shows higher power than the sunspots.

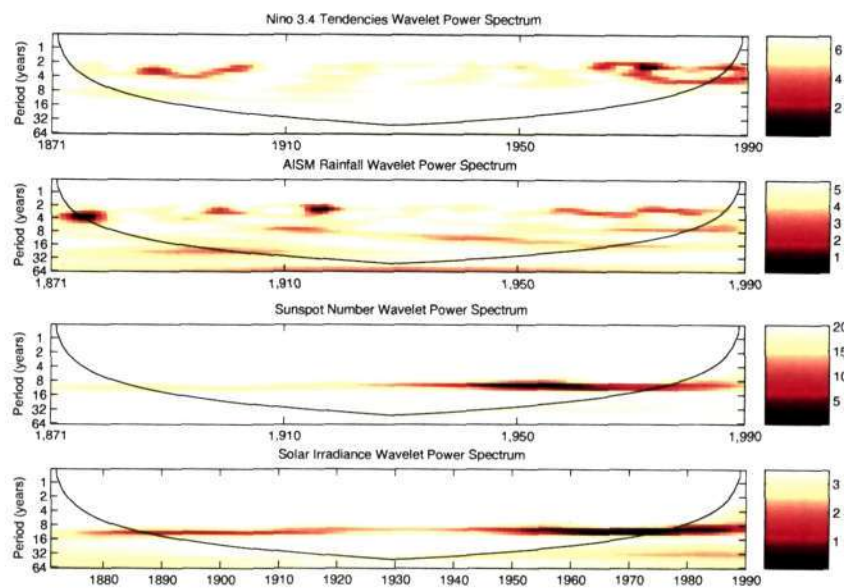


Figure 8.18. Wavelet Power Spectra for Nino 3.4 tendency (top panel), AISM rainfall (second panel), Sunspot Number (third panel) and Solar Irradiance (bottom panel).

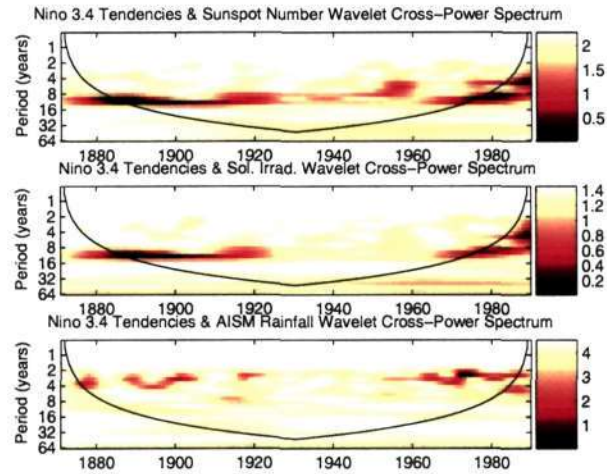


Figure 8.19. Wavelet Cross Power Spectra of Nino 3.4 tendencies with: Sunspot Number (top panel), Solar Irradiance (second panel), and AISM rainfall(bottom panel).

Next, we show in figure 8.19 the various wavelet cross power spectra among the four indices concerned. The top panel shows the cross spectrum for Nino 3.4 tendency and sunspot number. There is considerable cross-power over the period band 2-6 y, although it is highest in the 8-16 y period band. Over the first test period the cross power in the 8-16 y band is higher than that over the second test period; however, there is high power over the 1965-1990 period in the 8-16 y band. This shows that higher solar activity is connected with lower SST tendency and vice-versa. This result is again confirmed from the cross power spectrum of Nino 3.4 tendency with solar irradiance shown in the second panel. The cross power between Nino 3.4 tendency and AISM rainfall shows maximum power in the 2-8 y period band, with higher power over the first test period as compared to that over the second; but there is considerable power over the 1960-1990 period as well in the same band. This again confirms the weakening of the inverse relationship between the two after the 1970s.

Figure 8.20 shows the wavelet cross power spectra for Nino 3.4 tendency with HIM, WCI and NWI rainfall. In all these cases it is clearly seen that over the first test period of lower solar activity there is higher cross power compared to those over the second test period of higher solar activity. In figure 8.21 the cross power spectra between the CNEI, NEI and PENSI rainfall with Nino 3.4 tendency are shown in the top, middle and bottom panels respectively. The cross power for CNEI and NEI is high in the 2-8 y period band over three distinct epochs: 1882-1905 (which lies within the first test period of lower solar activity), 1950-1960 (which lies in the second test period), and 1965-1985. For PENSI rainfall and Nino 3.4 tendency, the cross power over the first test period is much higher than that over the second test period, although it is

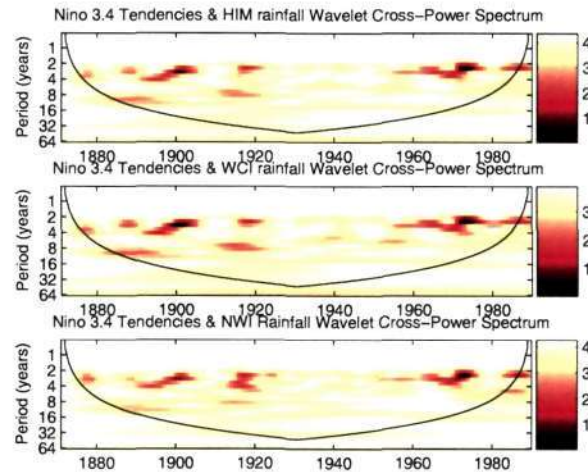


Figure 8.20. Wavelet Cross Power Spectra of Nino 3.4 tendencies with: HIM (top panel), WCI (second panel), and NWI rainfall (bottom panel).

quite high also over the period 1965-1985 in the 2-8 y period band.

Now we consider the slightly longer period of 1871-2000 for analysis. Figure 8.22 shows the wavelet cross power spectrum of Nino 3.4 tendency with solar irradiance in the top panel. Although there is high cross power in the 2-6 y period band particularly over 1990-2000, it is less compared to that over the first test period in the 8-16 y period band. This may be attributed to higher Nino 3.4 tendency over the period 1990-2000 as compared to the solar irradiance, which was not so high over the same period. On the other hand, the cross power between Nino 3.4 tendencies and AISM rainfall over 1990-2000 is not as low as may have been expected from the inverse relationship thought to characterize the ENSO–monsoon system (see second panel in figure 8.23). The cross power between solar irradiance and AISM rainfall, shown in the bottom panel of the figure, exhibits reasonable power in the 8-16 y period band over the period 1990-2000.

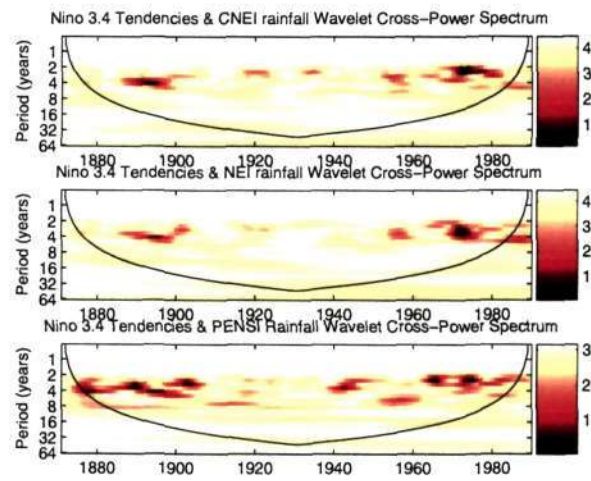


Figure 8.21. Wavelet Cross Power Spectra of Nino 3.4 tendencies with: CNEI (top panel), NEI (second panel), and PENSI rainfall (bottom panel).

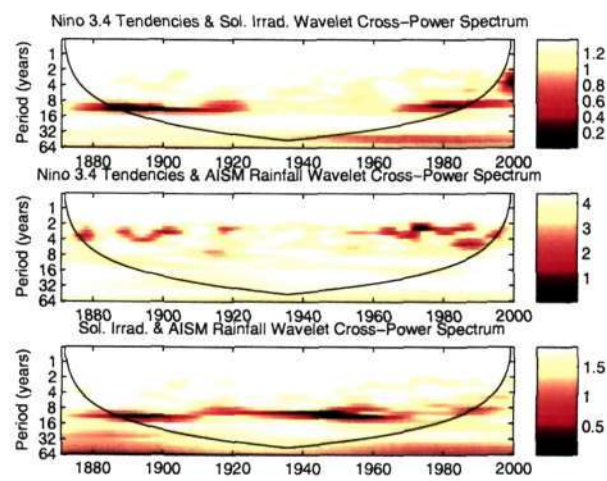


Figure 8.22. Wavelet Cross Power Spectra of Nino 3.4 tendencies with Solar Irradiance (top panel) and AISM rainfall (second panel), and between Solar Irradiance and AISM rainfall (bottom panel).

8.4.5 Results for connections between NINO 3, AISM and Solar Activity

Nino 3 SST has also been studied for connections with AISM and solar activity. Figure 8.23 shows the wavelet cross power for Nino 3 with sunspots (top panel) and with AISM (bottom panel). Figure 8.24 shows similar plots but for Nino 3 with solar irradiance and sunspot in the top and bottom panels respectively.

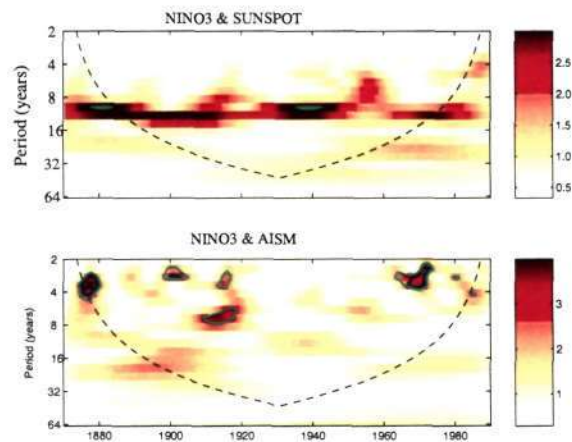


Figure 8.23. Wavelet cross power for Nino 3 and Sunspot (top panel) and Nino 3 and AISM (bottom panel).

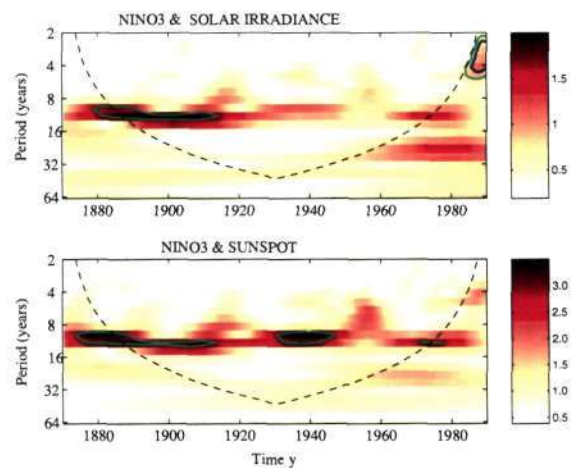


Figure 8.24. Wavelet cross power for Nino 3 and Solar Irradiance (top panel) and Nino 3 and Sunspot (bottom panel).

8.5 Discussion

In the work reported here, the correlations between solar activity and the rainfall and ENSO time series are found to be statistically highly significant, especially when they are studied over epochs of high and low solar activity. In contrast, the correlation between a full time series of an atmospheric process with the solar cycle (over a duration of 120 y say) often yields negligible correlation coefficients, as has in fact been reported by Labitzke and Loon (1990). ENSO covaries with high solar activity epochs negatively, at significance levels exceeding 97%. Sunspots and rainfall averaged over periods of order 30 y covary at higher significance levels than ENSO and rainfall, but contributions to rainfall power from ENSO are a factor of 3-4 higher.

The results from the wavelet cross spectral analysis provide confirmatory but far more detailed evidence for the above conclusions. Our results broadly agree with those outlined by Mehta and Lau (1997) insofar as the influence of ENSO and sunspot numbers on Indian monsoon rainfall is concerned. However, from our analysis, the connections between ENSO and solar activity come out to be stronger than the connection between AISM rainfall and ENSO.

Our results differ from Mehta and Lau (1997) regarding the role of the 11 y cycle. The statistical significance tests performed in this study on both the raw time series as well as on the wavelet cross spectra, with sample sizes respectively greater than 30 and 119, still hold good, and do not suffer from dearth of number of sample points as in the methods used by Mehta and Lau (1997). Thus, Mehta and Lau (1997) analyzed rainfall, SST and irradiance on the 11 year time scale using a narrow band Fourier filter centered at the 11 year period, in order to isolate the 11 year signal. They concluded that there was no consistent relationship between the 11 year components of solar irradiance and either the monsoon rainfall or solar irradiance or the Nino3 SST. Contrary to this conclusion, the present study finds that not only the rainfall but also ENSO show significant cross spectra with sunspots and other related parameters in the middle of the 8-16 y period band. The ENSO index by itself has a rather flat but high power spectrum at the 2-7 year band. ENSO also shows comparable power in the 8-32 y band. The rainfall shows multi-decadal periods and the solar indices show mainly the 11 year period and its harmonics and sub harmonics.

There are considerable variations in the ENSO-monsoon relations over the different homogeneous rainfall regions in India. In particular the connections of ENSO with HIM, WCI, NWI are qualitatively similar among themselves but are different from those with NEI and PENSI. The characteristics for ENSO-CNEI relations are somewhere in-between those for ENSO-HIM and ENSO-NEI relationships. This suggests that such relations vary in character from west to east in the Indian region, i.e. they are roughly organized along longitude.

As regards the connections with Nino 3.4 SST tendencies, our results agree with those reported by Rajeevan *et al.* (2005) in so far as the robust inverse relationship is concerned. However our results also confirm that over the 1970-2000 period, the so-called ENSO-monsoon

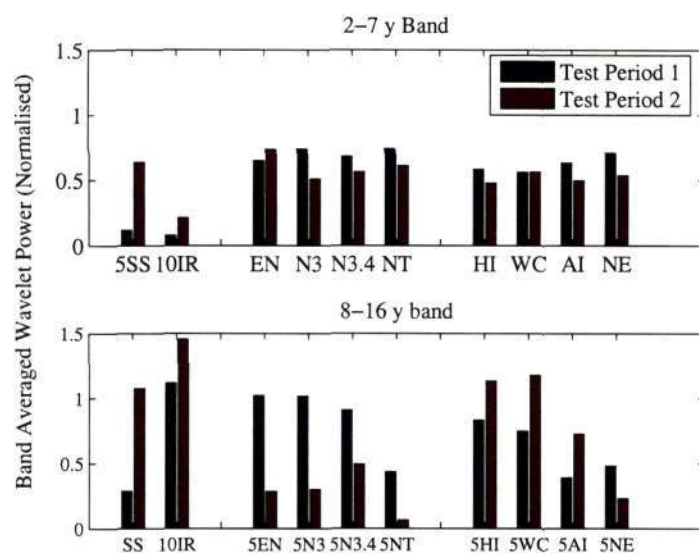


Figure 8.25. 2-7 y (top panel) and 8-16 y (bottom panel) band-averaged wavelet power for Sunspot numbers (SS), Solar Irradiance (IR), ENSO (EN), Nino 3 (N3), Nino 3.4 (N3.4), Nino 3.4 Tendencies (NT), HIM (HI), WCI (WC), AISM (AI) and NEI (NE) .

inverse relationship has weakened, as already reported by Krishna Kumar *et al.* (1999). There clearly are epochs over which the ENSO-monsoon relationship experiences a decreasing correlation, as suggested by Maraun and Kurths (2005).

Finally, figures 8.25 and 8.26 show a summary of the band averaged wavelet power and cross power respectively over the 2-7 y and 8-16 y bands for the ENSO-monsoon-sunspot *triad*. Figure 8.25 includes the band-averaged wavelet power, over both 2-7 y and 8-16 y bands, for ENSO indices (global ENSO, Nino 3, Nino 3.4, Nino 3.4 tendencies). All of them are higher in test period 1 than in test period 2 in the 8-16 y band. In the 2-7 y band the trend is the same for all indices except global ENSO, which is higher in test period 2 than in test period 1. Rainfall band-averaged wavelet power generally shows higher power in the second test period as compared to that in the first in the 8-16 y band, but lower power in the second test period as compared to the first in the 2-7 y band, except for NEI which has the opposite trend in the 8-16 y band. We have the important conclusion that while the solar activity and ENSO indices show nearly identical behaviour over both bands, rainfall shows opposite trends in the two bands.

Figure 8.26 shows the cross spectra over both the 2-7 y and 8-16 y bands. Band averaged cross power between all four ENSO indices and rainfall is higher in the first test period than in the second. The band averaged cross power between solar activity parameters and rainfall shows a trend opposite to that of ENSO-rainfall over both the bands under consideration. The

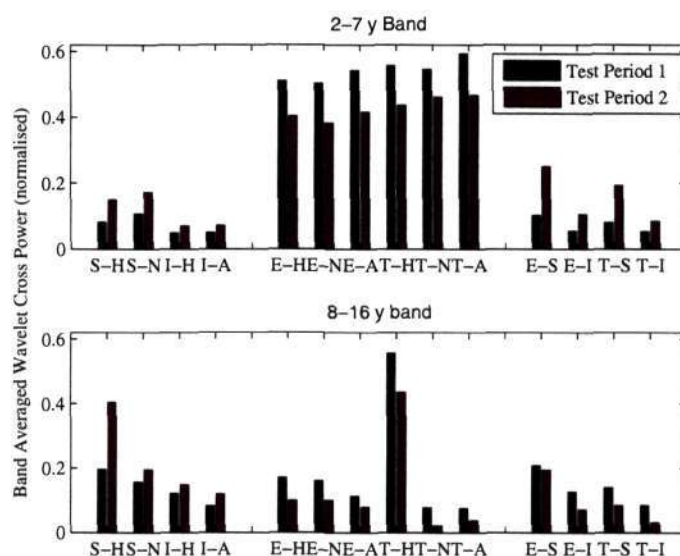


Figure 8.26. 2-7 y(top panel) and 8-18 y (bottom panel) band-averaged wavelet cross power for sunspot numbers-HIM (S-H), Sunspot-NEI (S-N), Irradiance-HIM (I-H), Irradiance-AISM (I-A), ENSO-HIM (E-H), ENSO-NEI (E-N), ENSO-AISM (E-A), Nino 3.4 -HIM (T-H), Nino 3.4 -NEI (T-N), Nino 3.4 -AISM (T-A), ENSO-Sunspot (E-S), ENSO-Irradiance (E-I), Nino 3.4 Tendency-Sunspot (T-S), Nino 3.4 -Irradiance (T-I).

ENSO-solar activity band averaged cross power in test period 2 is higher than in test period 1 in the 2-7 year band, but lower in test period 2 than in test period 1 in the 8-16 y band.

8.6 Conclusions

The present study involves AISM and homogeneous monsoon region rainfall, ENSO indices, solar irradiance and sunspot number, using wavelet cross spectral density analysis. The study indicates that there is considerable power in the wavelet cross power spectra in both 2-7 y and 8-16 y period bands for the ENSO-solar indices studied. However, the 2-7 y period band contains most of the cross power in case of ENSO-monsoon rainfall indices, while the 8-16 y period band contains most of the power in case of solar-rainfall indices. Furthermore, a detailed study on the variability of ENSO-monsoon-sunspot *triad* over two epochs of high and low solar activity suggests that, over the 2-7 year time scale, an increase in solar activity increases the ENSO index but decreases the monsoon rainfall in all regions, although there are regional variations on the magnitude of such a decrease in rainfall. The results for the 8-16 y time scale are however very different; here an increase in solar activity decreases the ENSO but increases the rainfall. A positive Nino 3.4 SST is associated with a decrease in the monsoon rainfall. Both these changes

occur in the test period of lower solar activity.

Wavelet Maps And Point Process Analysis of WTC Maxima

9.1 Introduction

We propose here a novel method for analysing the possible connections between solar processes and monsoon rainfall. The motivation for proposing this method comes from the wavelet (i.e the wavelet transform coefficient (WTC)) maps of Kailas and Narasimha 2000 and Narasimha and Kailas 2001, who studied homogeneous Indian Monsoon rainfall for the period 1870-1990. We first present a few wavelet maps drawn for rainfall in various parts of India, using the rainfall time series belonging to the country's different meteorologically homogeneous regions. Having observed the similarities and dissimilarities in the patterns shown by these maps, we go on to further analyse the observed similarities between the various rainfall maps and the sunspot map, and quantify these similarities with a simple regression-based mathematical model. The details of this analysis and the results so obtained follow in the sections below.

9.2 Wavelet Maps

A software package called NALLETS developed in VC++ by Dr. S. V. Kailas at the National Aerospace Laboratories, Bangalore, India, has been used for all the wavelet computations presented in this chapter. The package enables display of both the absolute magnitude and phase of the wavelet transform coefficients. It also provides for a choice of mother wavelet from among Morlet, Mexican hat and cubic spline. The package is available in both 1D and 2D versions and has been used extensively by Anandkumar and Kailas (1999), Kailas and Narasimha (1999), Kailas *et al* (1995) and Siddhartha *et al* (2000) for analysing atmospheric gust data and flow visualisation pictures of mixing layers and jets.

The results of a wavelet transform analysis are first presented here through colour coded contour-interval plots of the coefficients, which we refer to as wavelet maps. While presenting these maps we generally adopt 'local' scaling such that the coefficient is normalised at each wavelet time scale by its maximum value at that particular time scale. Equivalently, one could

consider the wavelet map in strips of short width in the scale axis, each strip being normalised within itself. All the wavelet maps presented here are locally normalised so as to reveal the temporal structure at long time scales. Although a region of intense activity in such a map may be globally (i.e. in terms of the highest value of the coefficient over the whole map) weak, it helps to highlight the presence of structure, which is the objective of our studies.

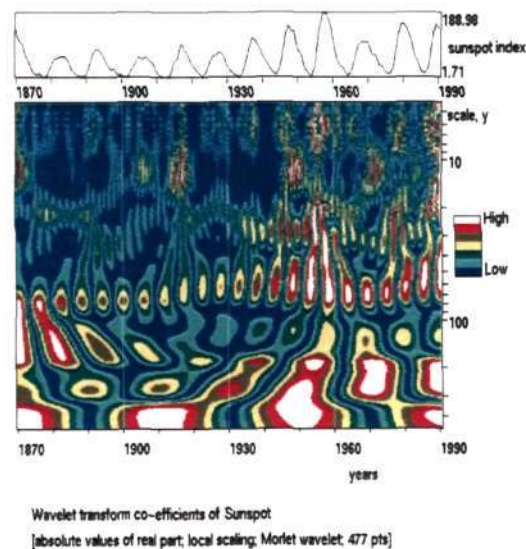


Figure 9.1. Wavelet transform coefficients of Sunspot Number (absolute values of real part; local scaling; Morlet wavelet; 1440 pts;)

Figure 9.1 shows the wavelet map for the sunspot number time series for the period 1870 to 1990. Only the absolute value of the real part of the transform in local scaling has been shown as contours over time and scale. A horizontal row of blobs separated by fixed time intervals in the wavelet map will represent a cycle in the original signal. The most striking feature of this wavelet map is the presence of several such structures in the form of blobs of red and white (indicating a high value of the coefficient) organized in roughly horizontal rows. It is interesting to observe, in the wavelet map for the sunspots, the presence of the pronounced 11 year cycle along with a few other weaker cycles.

A wavelet map for the NEI monsoon rainfall is shown in figure 9.2. A nearly horizontal row of blobs around the 11 year scale may be noted even there. The wavelet maps for four other homogeneous rainfall time series, namely HIM, CNEI, WCI and NWI, are shown in figure 9.3. Even here a prominent slowly meandering row of blobs is noticed around the 11 year

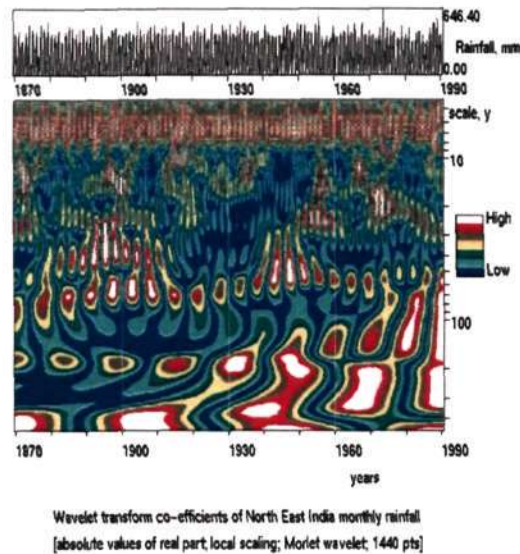


Figure 9.2. Wavelet transform coefficients of NEI monthly rainfall (absolute values of real part; local scaling; Morlet wavelet; 1440 pts;)

scale. Also present in these maps are other comparatively rapidly meandering rows of blobs at other scales. These have been thought to represent quasi-cyclic modes in the rainfall (see Kailas and Narasimha (2000)) and a detailed analysis of their approximate average periodicities has been published by Narasimha and Kailas (2001). The quasi-cyclic modes corresponding to the different average periods in rainfall are evident in these wavelet maps, as several roughly horizontal rows of blobs of varying intervals at different wavelet scales. The lower the period larger is the number of blobs at the lower wavelet scales. Thus the occurrence of a large number of fine blobs at the lowest scales is evidence of short periods while the fewer big blobs at larger scales are indicative of longer periods.

It is observed that the rainfall wavelet maps often exhibit striking similarity in pattern to the sunspot number wavelet map around the horizontal row of blobs around the 11 year scale. A major cycle of an approximately 11-year period is distinctly observed in all these figures at a wavelet scale of 30-50y. The presence of the 11-year period is apparent to varying degrees for the different rainfall time series considered. Since the sunspot index time series data is less noisy compared to the rainfall data, the presence of jitter in the wavelet map of the sunspot index data is comparatively less. We make a detailed statistical analysis for comparing the similarities observed in the rainfall and sunspot wavelet maps in the next section.

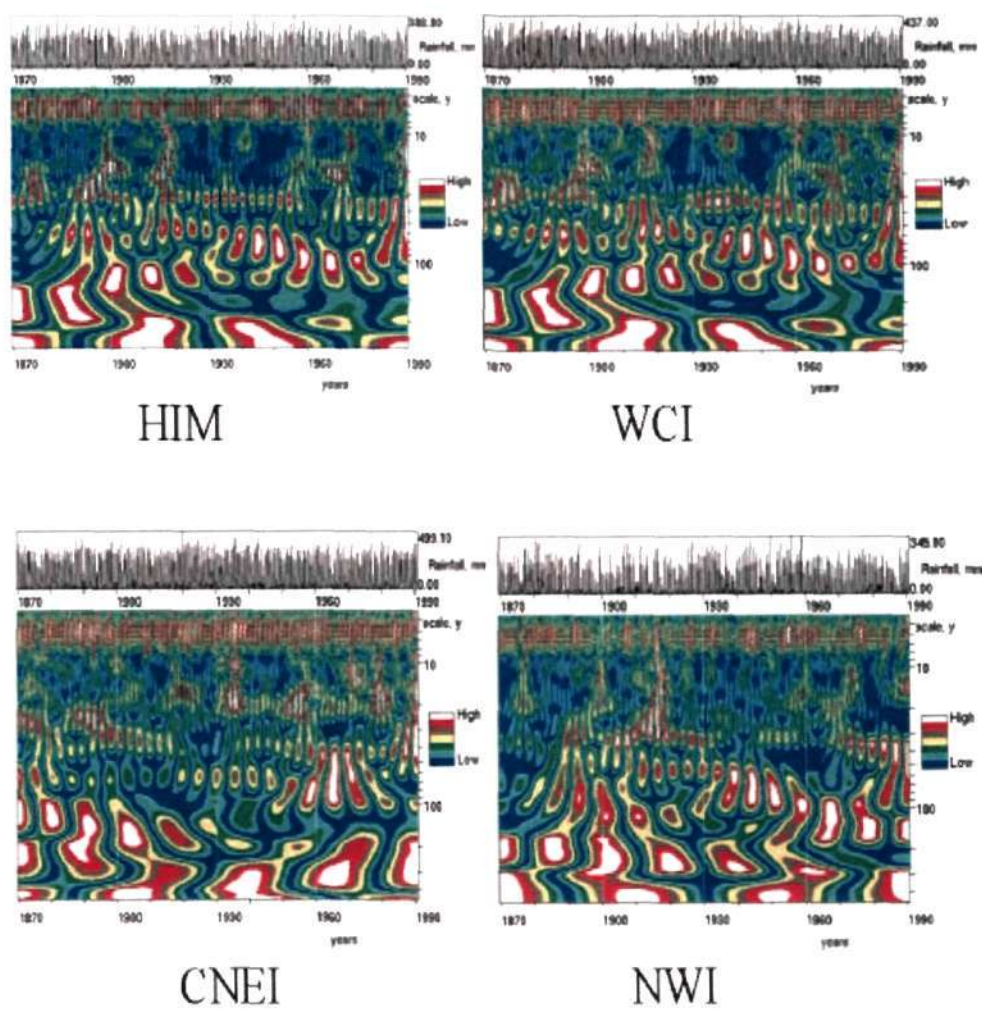


Figure 9.3. Wavelet transform coefficients of four homogeneous monthly rainfall (absolute values of real part; local scaling; Morlet wavelet; 1440 pts;)

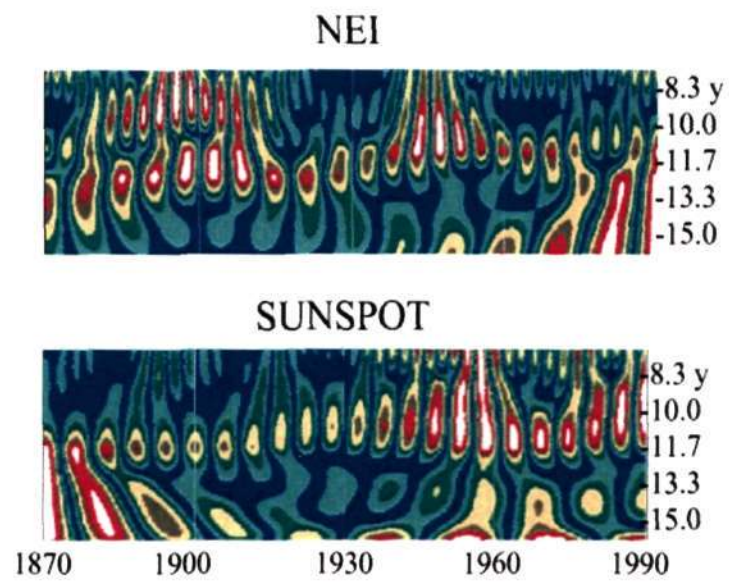


Figure 9.4. Comparison of NEI and Sunspot number WTC maxima around the 11 year period.

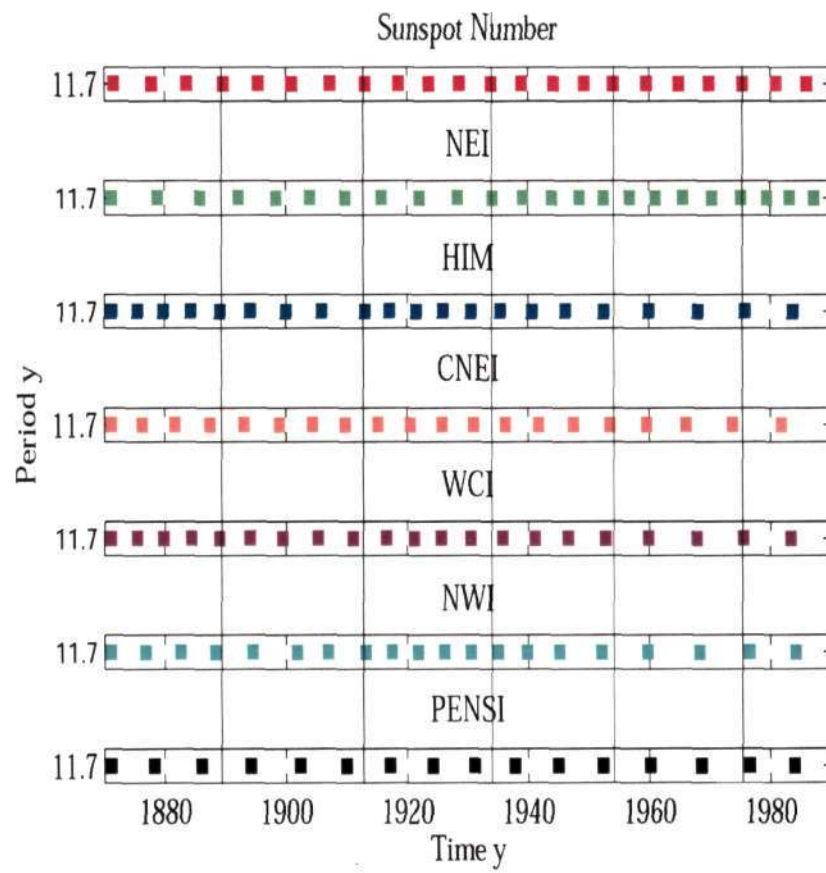


Figure 9.5. Point process time series of occurrence of WTC maxima in homogeneous rainfall and Sunspot number.

9.3 Statistical Analysis of Similarities

For the 11-year cycle, the local maxima in the figures for NEI and sunspots, in the wavelet period range 8–16 y, have been re-plotted on a zoomed scale in figure 9.4. The times of occurrence of the maxima in the two maps are separately plotted in the top two panels of figure 9.5. Also plotted in the other panels of figure 9.5 are the times of occurrence of WTC maxima for all the other five homogeneous rainfall time series.

It is seen that the similarity between the times of occurrence of WTC maxima in all these cases here is very striking. (Note that on the wavelet scale axis now the Fourier period is identified.) A remarkable near-simultaneity of WTC maxima for all 6 homogeneous rainfall and sunspot numbers is evident here but there are also significant phase differences at certain times. One can now model the temporal location of the maxima of the wavelet transform coefficients of the rainfall and sunspot indices as point processes in time. We recall that a point process may be defined as a stochastic time series which in the simplest case can be represented as points or dots on a real line, for example, points along a time axis at the instants of failure of light bulbs in a building (see for instance, Cox (1962, 1966, 1972) and Cox and Isham (1979)).

To focus on further analysis of the comparison between the two point processes, we first examine as to what may be the correct questions to ask. These questions might be crystallised appropriately into the following:

Given two point process time series data, how to devise a statistical or mathematical method
(i) for establishing whether there is any sort of dependency between the two data sets; and –
(ii) (if there exists one), for deriving the form of that dependency.

The above questions themselves can be treated as problems in mathematics which demand much attention and research. Some studies in the statistical analysis of dependencies in point processes using renewal theory were reported by Cox in the early 70's, see for instance Cox (1972). Most of these theories have been developed towards modeling and analysis of stochastic point processes governing rare events of occurrence as in Poisson and other renewal processes.

In a bivariate point process, the dependence of one type of event, say type A, on the other events, say type B, had been of interest in these studies (see for instance, Cox and Isham (1977)). One could perturb the hazard function of a renewal process by a factor depending on 'quantities' thought to influence the probability of occurrence, each such quantity being combined with an unknown regression coefficient. Estimates of the unknown regression coefficients may be obtained via a conditional likelihood technique, leading in particular to asymptotic significance tests for the presence of dependencies. In the present study, the assumptions underlying the renewal-theory-based analysis of dependencies were not really satisfied, and hence the theory was not found to be applicable. For this reason, a simple alternative approach towards answering

the questions in the regression framework has been developed.

9.3.1 Regression approach

In the framework of regression analysis, it is quite possible to detect trends in data from the two point processes in the following manner:

- Plot the WTC time series against each other and obtain a line/curve of best fit to the data by regression.
- Model the deviations of the data from the regressed curve appropriately as systematic or stochastic.
- For systematic deviations which have periodic components, model them as a sum of sinusoidal functions with unknown time-periods and amplitudes, the values of which can be sought as solutions to an unconstrained error minimisation problem.
- The superposition of the deviation model on the regressed curve provides an enhanced fit to the original data.
- The residual deviations of the model from the actual data can then be tested for their stochastic properties using an appropriate significance test with tight confidence levels.

9.3.2 Method Implemented

In order to ascertain whether there is indeed a relationship between the two processes, we focus our attention on the curves in figure 9.5 where the maxima in the WTC due to both rainfall and sunspot are plotted in coloured squares as function of time and scale. The approximate co-occurrence of WTC maxima of both series (accompanied by a slow change of phases) is evident here. A plot of the times of occurrence of WTC maxima in rainfall (T_R) against corresponding times of occurrence of WTC maxima in sunspot index (T_S) shows an approximately linear trend, as may be seen from the scatter diagram as in the top left panel of figure 9.6 for the NEI and bottom left panel for CNEI monthly rainfall time series data. The scatter in these diagrams is seen to be quite low. Note incidentally that both T_R and T_S are measured in units of years with the year 1870 as the origin.

The regressed line equation in the case of NEI is given by

$$T_R \simeq L(T_S) \equiv 0.97T_S + 3.84, \quad (9.1)$$

where $L(T_S)$ represents the best linear fit. The deviations from equation 9.1, i.e. $T_R - L(T_S)$, are small (less than 1 year in a time scale of 120 years), and what is even more interesting is that much of it seems systematic. These systematic deviations (see figure 9.6 top left panel), which

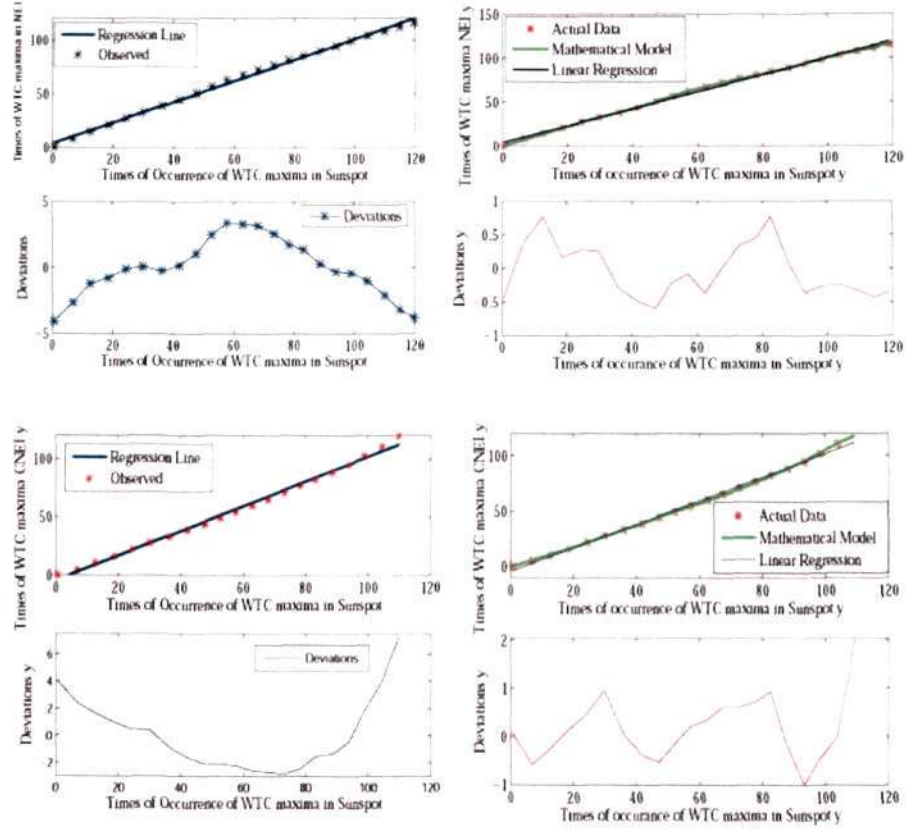


Figure 9.6. Regression analysis results of NEI and CNEI WTC with sunspot number WTC.

have significant periodic components, can be modelled as a sum of two sinusoids and expressed as

$$F_{per}(T_S; \theta) = L(T_S) + \theta_1 \sin\left(\frac{2\pi}{\theta_2} T_S + \theta_3\right) + \theta_4 \sin\left(\frac{2\pi}{\theta_5} T_S + \theta_6\right) \quad (9.2)$$

where $F_{per}(T_S; \theta)$ is the model incorporating the linear regression line $L(T_S)$ and the systematic cyclic variations as modelled by sinusoidal functions involving θ . Here $\{\theta\} = \{\theta_i\}, i = 1, \dots, 6$, is a set of underdetermined constants to be obtained as solutions to the optimisation problem in the \mathcal{L}^2 norm

$$\min f(T_S; \theta) = \| T_{per}(T_S; \theta) - T_R \|^2 = \sum_{i=1}^N (T_{per}(T_{S_i}; \theta) - T_{R_i})^2 \quad (9.3)$$

where $T_{R_i}, i = 1, \dots, 120$, is the set of times at which WTC maxima occur in rainfall as mea-

sured from the data. Using the nonlinear unconstrained minimisation routine '*fminsearch*' in the matlab optimisation tool box, a solution set for the constants θ can be obtained. When incorporated in the expression for $T_{per}(T_S; \theta)$ we obtain the expression

$$T_{per}(T_S; \theta) = 0.97T_S + 3.84 + 1.56 \sin\left(\frac{2\pi}{2.51}T_S + 2.27\right) + 1.33 \sin\left(\frac{2\pi}{1.00}T_S + 1.01\right). \quad (9.4)$$

This expression seems to model the WTC point process data in the top right panel of figure 9.6 reasonably well.

The residual stochastic deviations $(T_{per}(T_S; \theta) - T_{R_i})$ of the model $T_{per}(T_S; \theta)$ from the data T_R are also plotted in the top right panel of figure 9.6 as function of time. It is interesting to note that the magnitude of the deviations is very small (less than (0.83%)) compared to the time scale involved in the analysis. A χ^2 test performed on these deviations confirms at a 95% confidence level that the deviations indeed come from a normal distribution. The χ^2 test however is not sensitive enough for samples of small size, and involves an arbitrary choice of categories into which the data are classified. However a Kolmogorov-Smirnov test, with modified Lilliefors critical region values for the deviations (see appendix for details), confirms with 99% confidence that the deviations are indeed sampling fluctuations arising from normal distributions. The Lilliefors test for goodness of fit of an input data vector x to a normal distribution evaluates the hypothesis that x has a normal distribution with unspecified mean and variance, against the alternative hypothesis that x does not have a normal distribution. This test essentially compares the empirical distribution of x with a normal distribution having the same mean and variance as x . It is similar to the Kolmogorov-Smirnov test, but allows for the fact that the parameters of the normal distribution are estimated from x rather than being specified in advance.

The same procedures have been repeated over the other five homogeneous monthly rainfall time series. The regression analysis results for HIM and NWI rainfall are shown in figure 9.7 whereas those for WCI and PENSI are shown in figure 9.8.

The final expression for the model for times of occurrence of WTC maxima in the case of HIM rainfall is as follows:

$$T_{per}(T_S; \theta) = 1.03T_S - 6.66 + 9.48 \sin\left(\frac{2\pi}{91.05}T_S + 0.73\right) - 7.81 \sin\left(\frac{2\pi}{74.78}T_S + 0.05\right) \quad (9.5)$$

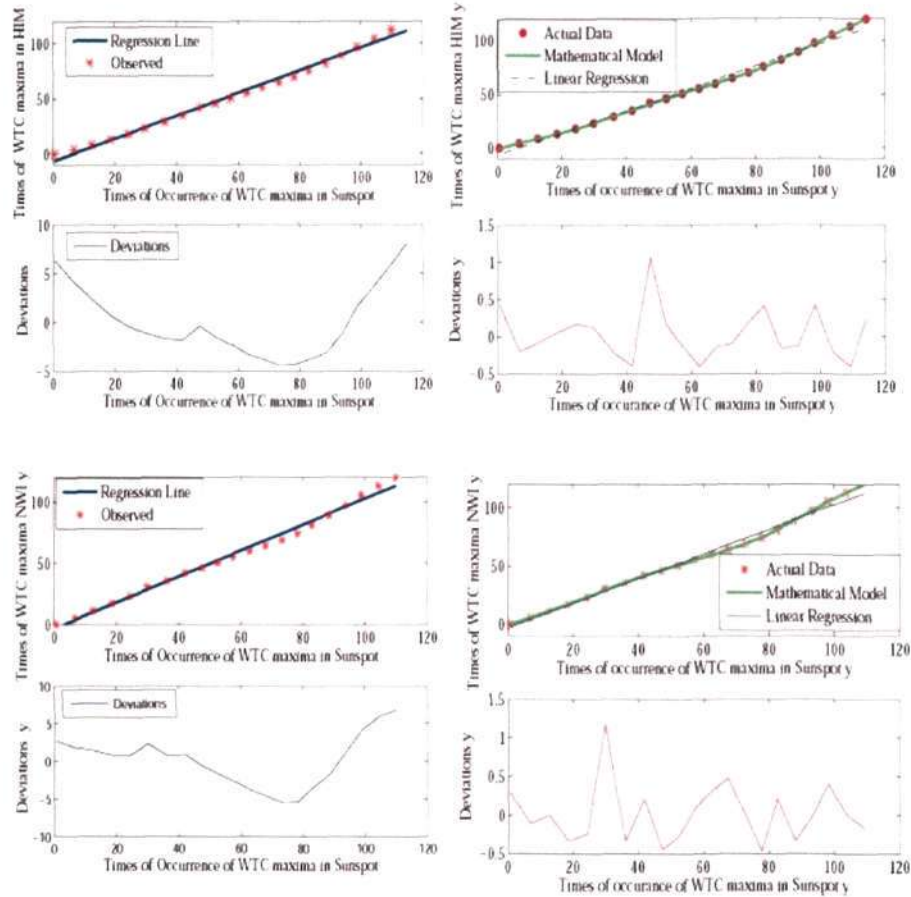


Figure 9.7. Regression analysis results for HIM and NWI WTC with sunspot WTC.

The model parameters for all the homogeneous rainfall cases are tabulated in Table 9.3.2. $\theta(1)$ and $\theta(4)$ are the amplitudes of the systematic deviations. $\theta(2)$ and $\theta(4)$ are the time-periods while $\theta(3)$ and $\theta(6)$ are the respective phases of these variations. In all these cases the hypothesis that deviations of model from data indeed come from normal distributions is confirmed at 99% confidence level.

9.4 Discussion

The new technique proposed in this chapter overcomes the limitation imposed by the Torrence-Compo test for statistical significance in a rather simple manner.

It is interesting to note the different time periods of the cycles identified through equations 9.1–9.5. The periodicities in the Indian monsoon rainfall reported by Krishna Kumar (1997) in his detailed study on Indian monsoons using, *inter alia*, spectral methods, and the quasi-cyclic

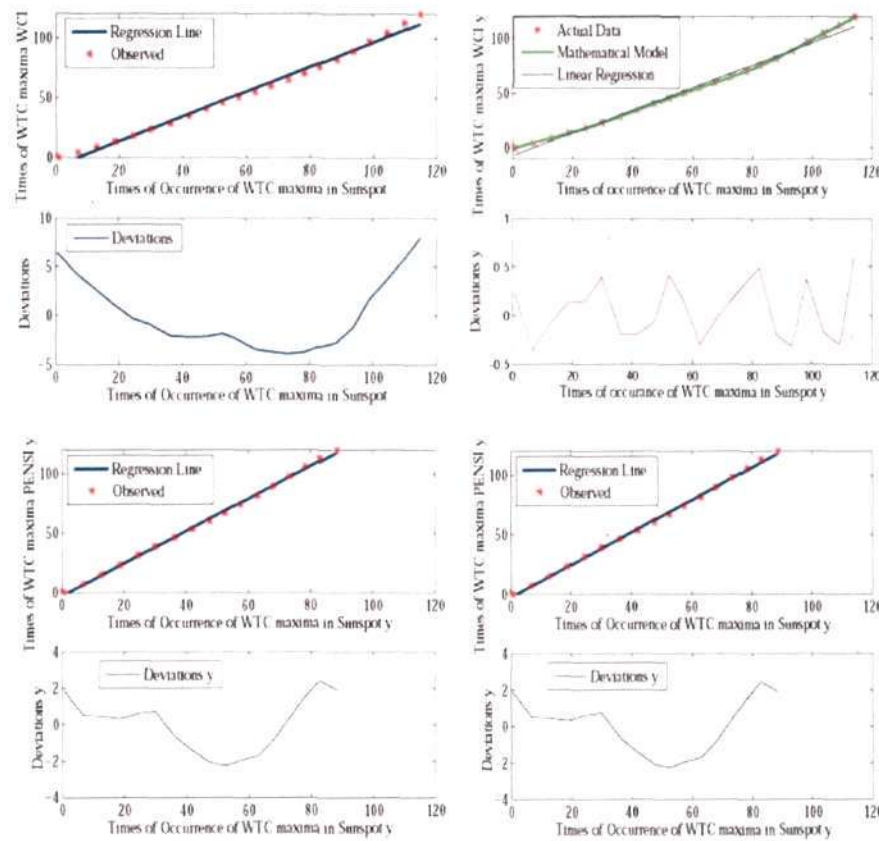


Figure 9.8. Regression analysis results for WCI and PENSI WTC with sunspot WTC.

Table 9.1. Table for model parameters for various metrological subdivisions

Data	Slope	Intercept	y	$\theta(1)$ y	$\theta(2)$ y	$\theta(3)$ rad	$\theta(4)$ y	$\theta(5)$ y	$\theta(6)$ rad
NEI	0.97	3.84	2.84	121.99	10.95	0.81	41.23	4.84	
HIM	1.03	-6.66	9.48	91.05	0.73	-7.81	74.78	0.05	
WCI	1.03	-6.88	15.81	88.81	0.67	13.63	79.39	-2.88	
NWI	1.06	-3.13	5.44	88.20	0.57	4.08	67.90	3.27	
CNEI	1.06	-4.36	11.60	86.08	0.70	9.80	77.48	-2.77	
PENSI	1.07	-0.82	1.15	30.11	-0.12	1.82	69.78	0.45	

periods in the monsoon rainfall observed by Kailas and Narasimha (Kailas and Narasimha 2000), are also exhibited by the wavelet maps of north-east India and homogeneous Indian monsoon rainfall time series. Further, cycles of periodicities of approximately 122, 88/90, 77/80, 67/70, and 30/42 years in the rainfall data have also been found in the present study. One can think

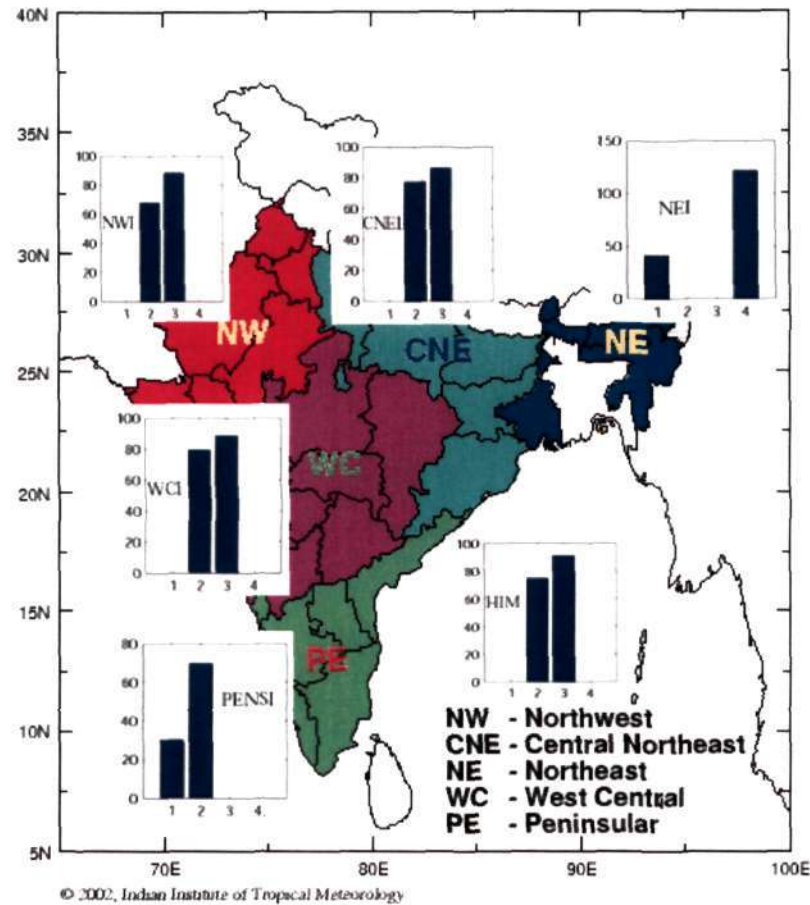


Figure 9.9. Homogeneous rainfall map of India showing the periods obtained from regression analysis. Band 1: 30–60 y, Band 2: 60–80 y, Band 3: 80–100y, Band 4: 100–122 y

of the above numbers as being close to integral multiples of 11 or 11.6 years; they may also be connected with other solar process characteristics. From figure 9.7 it is clear that WCI, NWI and CNEI are statistically homogeneous, whereas PENSI is slightly different, and NEI vastly so.

It would be interesting to consider whether this study provides a means for prediction of the occurrence of forthcoming cycles in monsoon rainfall data. The present approach provides information on the phase relationship between the two point processes, more directly than any other statistical procedures in common use. These results conform with the results obtained from the three different approaches of wavelet analyses between the monsoon rainfall and sunspot data described in Chapters 4 to 8 of the thesis. However, in the method proposed in this chapter, the nature of the correlation between sunspots and Indian monsoon rainfall is depicted in a much simpler manner as compared to other methods implemented so far in this thesis, and

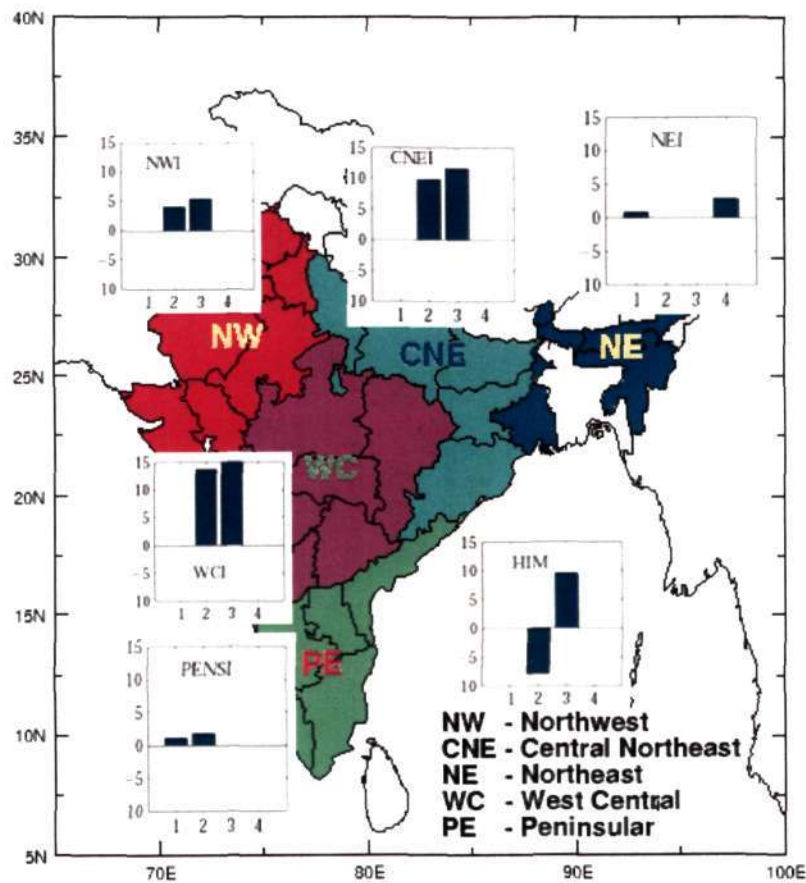


Figure 9.10. Homogeneous rainfall map of India showing the amplitudes for different period bands obtained from regression analysis. Band 1: 30–60 y, Band 2: 60–80 y, Band 3: 80–100y, Band 4: 100–122 y

furthermore phase information is provided.

We have not pursued these questions in great detail here, leaving them for future investigation. There are grounds for believing, however, that the novel method proposed in this Chapter has great promise and potential, and deserves much further study than it has been possible to devote to it in the present thesis.

9.5 Conclusions

- Regression analysis using a novel point–process approach reveals a nearly linear trend between times of occurrence of rainfall and sunspots WTC maxima in the 9–13 y band, with small systematic and stochastic deviations from the regressed line.

-
- Suitable (periodic) function models for the systematic deviations have been obtained through an unconstrained error minimisation scheme, providing potentially useful information on periods and phases.
 - These models provide an excellent fit to the point process time series of the WTC maxima obtained from actual data for rainfall and sunspots.
 - The Lilliefors significance tests on the residual stochastic deviations suggest with 99% confidence that they are sample fluctuations obtained from normal distributions.
 - These results indicate a strong connection between solar processes and monsoon rainfall around the 11 year period and enable quantitative studies of phase relationships.
 - There are regional variations in the relations between sunspots and rainfall. WCI, NWI, CNEI have great similarity in these relations; e.g. both periods and amplitudes from the linear fit are very nearly the same. PENSI is somewhat different. The reasons for these variations need to be investigated.
 - The proposed technique appears to have considerable potential.

Conclusions, Explanations and Vistas Ahead

10.1 Conclusions

This thesis presents an analysis of possible connections between solar activity and Indian monsoon rainfall, using chiefly for the latter the reliable data set that has been accumulated in India over the period 1871-1990. Following are the major conclusions from the thesis:

- A simple time domain analysis reveals that over the period 1871–1990 solar activity parameters exhibit nonstationarity. The analysis of rainfall is performed over two distinct test periods (1878–1913 and 1933–1964) respectively of low and high solar activity, each comprising three complete solar cycles, representing the highest contrast in the 120 y period. The analysis covers all the six homogeneous zone rainfall data published by Parthasarathy *et al.* (1995), namely West Central India (WCI), North West India (NWI), Homogeneous Indian monsoon (HIM), Peninsular India (PENSI), Central North East India (CNEI) and North East India (NEI), and also for the All India Summer Monsoon (AISM). Greater solar activity is associated in all cases with greater rainfall, although at significance levels that are distinctly high (exceeding 97%) in 2 out of the 6 homogeneous cases (HIM (97%) and WCI (99%)), and greater than 75% even in the other 4 cases (NEI (75%), NWI (75%), CNEI (80%) and PENSI (85%)). (AISM rainfall does not represent a homogeneous region, and for this reason is not the best case for studying solar/rainfall associations; but even here the confidence level for the association is 95%.)
- In 9(15) out of 29 subdivisions, rainfall is higher during the high solar test period at z -test confidence levels exceeding 90%(80%) respectively.
- The strongest connections between solar activity and rainfall (confidence levels > 96%) are observed in subdivisions along the west coast (Konkan (99.9%), Kerala (97%) and Coastal Karnataka (96.3%)) and in central India (West Madhya Pradesh (99.9%)), and the weakest in north-east India (North Assam (77.5%) and Sub-Himalayan West Bengal (67.5%).

- The mean Pacific SST anomalies related to ENSO are higher in the lower solar activity period than in the higher solar activity period, unlike rainfall. The confidence levels to which these differences in means are significant are highest in the case of global ENSO data (95%) and lowest in the case of Nino3.4 (55%).
- Wavelet power spectra of all the rainfall time series under consideration show substantial power in the 8–16 y period band, varying from 11.3% (NEI) to 25.2% (HIM) among the rainfall time series. Contributions to ENSO indices vary from 14.8% (global ENSO) to 21.1% (NINO3).
- Except for NEI, the five homogeneous and AISM rainfall time series show that wavelet power in the 8-16 y band is higher in the period of higher solar activity and lower in the period of lower solar activity, the difference between them being significant at confidence levels greater than 99.9%.
- The wavelet power of the ENSO indices, averaged over the 8-16 y band, is higher during the lower solar activity period and lower in the higher solar activity period, thus showing a trend opposite to that of rainfall-solar activity. This is to be expected from the well-known inverse relationship between ENSO and rainfall. Even in these cases, the confidence levels at which the differences (in band averaged wavelet power over the two test-periods) are significant are greater than 99.99% for all three ENSO indices in the 8-16 y, 9-13 y and 10-12y bands, except for the 10-12 y and 9-13 y bands in the case of Nino 3.4, where the confidence levels are about 97.5%.
- The Torrence–Compo test of statistical significance on the rainfall–solar activity wavelet cross spectrum reveals significant cross power around the 11 y solar cycle period for all the rainfall indices considered. In particular the global cross power spectra for AISM, WCI and HIM rainfall with the group sunspot number reveal a peak around the 11 year period at confidence levels of 95% or higher.
- Cross spectral analysis confirms that greater solar activity is associated in all cases with greater rainfall (supporting the conclusion from time-domain analysis), although at significance levels that are distinctly high (> 95%) in 3 (HIM, WCI and AISM) and lower (< 90%) in 4 (NWI, CNEI, NEI and PENSI) out of the 7 cases studied. This variation is organized roughly along the longitude across the country; it is not inconsistent with the simulations of Haigh *et al.* (2004), which suggest that one effect of solar activity would be a displacement of such atmospheric circulation systems as the Hadley cell. Our analysis suggests a small latitudinal displacement of an appropriate circulation system with higher solar activity, implying a rising component in the west and a sinking component in the east.

- On the ENSO-rainfall cross spectrum, the Torrence-Compo test reveals significant cross power spread over the 2-7 y period band across most of the indices considered, but NEI, CNEI and PENSI have significant cross power also around the 16 y period, although some of those regions are well within the cone of edge influence in the wavelet maps. However the global cross spectra for all the ENSO-rainfall indices were rather less significant, the confidence levels varying from 65% to 85%.
- Interestingly, the ENSO-solar activity cross spectra reveal considerable cross power in the 4-8 y and 8-16 y bands, the power in both bands over the first test period (1878-1913) being greater than over the second test period (1933-1964).
- The global cross spectrum for ENSO and solar activity indices exhibits peaks at around the 11 y period at confidence levels of 90% or higher. In particular, the confidence level for the solar irradiance-ENSO index is as high as 97.5%. This shows that there is a stronger connection between ENSO and solar activity as compared to the ENSO-rainfall connection. Greater solar activity is associated with lower ENSO activity and vice-versa, supporting the well-known inverse relationship between ENSO and rainfall. More importantly, this finding suggests that Indian rainfall is affected by solar processes indirectly through ENSO.
- A statistical comparison of the cross spectra of sunspots with HIM rainfall and with three noise signals respectively has been performed. The noise signals include those matching the spectrum and the probability distribution function of the rainfall time series. It is found that over the two test-periods already mentioned, the average cross power for HIM rainfall and sunspot number exceeds that between noise and sunspots at confidence levels of 99.99% or higher in the 8-16 y, 9-13 y and 10-12 y bands using the z -test.
- As regards spatial variation of the solar activity-rainfall relations, the results from the regions WCI, NWI and AISM are similar in nature while NEI is distinctly different from all of them. CNEI and PENSI possess characteristics that are in between those of WCI and NEI. This again shows a roughly longitudinal variation in the relations, varying from strong in the west to weak in the east.
- A study involving AISM rainfall, ENSO index, solar irradiance and sunspot number, using wavelet cross spectral density analysis as outlined by Torrence and Compo (1998), reveals that although there is considerable power in the wavelet cross power spectra in both 2-7 y and 8-16 y period bands for the ENSO-solar indices studied, the 2-7 y period band contains most of the cross power in the case of ENSO-monsoon rainfall indices, while the 8-16 y period band contains most of the cross power in the case of solar-rainfall indices.
- The contributions from the 2-7 y and 8-16 y bands to cross power between the various indices considered here are summarized in tables 10.1 and 10.2. Many of the conclusions

drawn in this thesis are displayed in quantitative terms in the Table. In particular, we may note :

- the strongest contributions are in the pairs sunspot-rainfall, Nino 3.4 tendency-rainfall, sunspot-Nino 3.4 and sunspot-Nino 3.4 tendency;
 - the cross power for AISM rainfall are in between those of HIM and NEI rainfall;
 - the contributions to ENSO-rainfall cross spectra from the 8-16 y band are not substantially less than from the 2-7 y band.
-
- Furthermore, a detailed study of the variability of the ENSO-monsoon-sunspot triad over the two epochs of high and low solar activity suggests that, on the 2-7 year time scale, an increase in solar activity increases the ENSO index and decreases the monsoon rainfall over all regions, but there are regional variations in the magnitude of such a decrease. The results on the 8-16 y time scale are however much different. An increase in solar activity is associated with a decrease in the ENSO index and an increase in the rainfall over the 8-16 y band. The net effect of solar activity on rainfall therefore appears to be the result of counteracting influences on the two bands i.e. on short and long periods; scale-interactions therefore appear to be important.
 - The effect of positive Nino 3.4 SST tendencies on the monsoon rainfall is to decrease the rainfall. Both these effects occur in the test period of lower solar activity.
 - The link between monsoon rainfall and solar activity emerges as having the strongest evidence; the ENSO-solar activity connection is stronger than for the ENSO-monsoon connection.
 - A novel approach, using wavelet analysis and point process theory to unravel the existence of possible correlations between the solar cycle period as extracted from the yearly means of sunspot numbers and the periodicities of Indian monsoon rainfall, has been proposed. Striking similarity between the wavelet transform coefficient maps of sunspot number time series and those of homogeneous Indian and north-east India monsoon rainfall monthly time series, especially around the 11-year period, have been revealed. These similarities are quantified by devising statistical schemes for identifying a trend or dependence between the two point processes given by wavelet transform coefficient maxima around the 11-year average period for the monsoon rainfall and sunspot number indices. A regression analysis reveals a predominantly linear trend between times of occurrence of WTC maxima, with small but systematic deviations from the regressed line superposed on it. Suitable periodic function models for these systematic deviations from the linear trend have been obtained through an unconstrained error minimisation scheme. The combined

linear-periodic regression models provide excellent fits to the wavelet transform coefficient maxima time series obtained from actual data. The deviations of the regression model from the data are small ($< 1\%$) compared to the magnitude of the variables involved, and the Lilliefors test on these residual deviations suggests with 99% confidence that they are sample fluctuations obtained from normal distributions. The study also suggests the presence of certain sub-harmonics of the solar cycle period in the monsoon rainfall time series, and provides information on their phase relationships.

- The evidence for multi-decadal connections between Indian rainfall and solar activity, directly and mediated through ENSO, is thus strong, as tested by three different procedures: time-domain analysis (which uses sunspot numbers only to select periods of greatest contrast in solar activity), wavelet cross spectra (band-averaged and otherwise, which use quantitative solar activity data to analyse effects in different period bands), and point process methods (which provide phase information, suggesting a modulation of the effect of the 11 y cycle by cycles of longer periods).

Table 10.1. % Contribution to cross power

Data	2-7 y band (%)	8-16 y band (%)
Sunspot and HIM	12.78	56.84
Sunspot and WCI	12.92	54.81
Sunspot and NWI	13.38	59.46
Sunspot and CNEI	17.69	46.51
Sunspot and NEI	15.22	45.26
Sunspot and PENSI	21.06	55.62
Sunspot and AISM	17.10	51.91
Irradiance and HIM	10.26	44.56
Irradiance and WCI	9.96	41.65
Irradiance and NWI	11.40	49.59
Irradiance and CNEI	13.68	36.16
Irradiance and NEI	10.78	36.84
Irradiance and PENSI	17.19	49.23
Irradiance and AISM	13.24	40.03
ENSO and HIM	27.26	23.83
ENSO and WCI	26.24	21.11
ENSO and NWI	31.79	28.07
ENSO and CNEI	33.90	15.18
ENSO and NEI	28.66	17.93
ENSO and PENSI	43.53	26.12
ENSO and AISM	31.97	19.55
Nino 3 and HIM	36.67	28.16
Nino 3 and WCI	36.31	26.01
Nino 3 and NWI	39.28	30.44
Nino 3 and CNEI	45.11	17.56
Nino 3 and NEI	39.25	22.57
Nino 3 and PENSI	51.67	27.05
Nino 3 and AISM	43.39	23.98

10.2 Possible Explanations

Section 1.6 has already presented a review of the current position on models that purport to explain possible relations between solar processes and terrestrial climate. It will be recalled that the 11 y sunspot cycle results in flux changes of order $2\text{W}/\text{m}^2$, which is a few tenths of one percent of the mean flux of about $1350\text{W}/\text{m}^2$. An amplifier is therefore required to convert these small flux changes to significant changes in terrestrial climate. Many proposals, reviewed

Table 10.2. % Contribution to cross power (contd)

Data	2-7 y band (%)	8-16 y band (%)
Nino 3.4 and HIM	33.09	28.58
Nino 3.4 and WCI	32.95	26.24
Nino 3.4 and NWI	35.80	32.17
Nino 3.4 and CNEI	41.31	19.29
Nino 3.4 and NEI	36.76	23.78
Nino 3.4 and PENSI	48.87	29.52
Nino 3.4 and AISM	39.52	24.58
Nino 3.4 Tendency and HIM	51.15	22.06
Nino 3.4 Tendency and WCI	49.25	20.64
Nino 3.4 Tendency and NWI	57.10	23.25
Nino 3.4 Tendency and CNEI	59.28	12.76
Nino 3.4 Tendency and NEI	53.58	16.31
Nino 3.4 Tendency and PENSI	66.03	20.22
Nino 3.4 Tendency and AISM	57.59	16.55
ENSO and Sunspot	16.52	43.53
ENSO and Irradiance	11.53	35.79
Nino 3 and Sunspots	18.99	50.71
Nino 3 and Irradiance	15.04	44.43
Nino 3.4 and Sunspots	18.27	53.94
Nino 3.4 and Irradiance	14.89	47.28
Nino 3.4 Tendency and Sunspots	27.65	49.48
Nino 3.4 Tendency and Irradiance	23.33	42.88

in Chapter 1, have been made to explain how the required amplification may occur. One of the significant findings of the present thesis is that the strength of the association between monsoon rainfall and solar processes varies systematically across India. Roughly speaking, the association is strong along the West Coast, West Central India and Central North East India and becomes weaker towards the North East. This suggests a variation that is a stronger function of longitude than latitude, and possibly also an effect of solar processes on the position and/or intensity of major circulation systems such as the Hadley cell or the Walker circulation. Simulations by Haigh (2005) show a displacement of the Hadley cell in response to changes in solar radiation flux. It will also be recalled that the variations in radiant flux are much higher in the ultra-violet region of the spectrum than in the visible. Keeping these facts in mind, a plausible schematic of the effect of solar radiation on climate is provided in figure 10.1. This however is no more than a broad summary of the various models that have been proposed, and should be considered only illustrative.

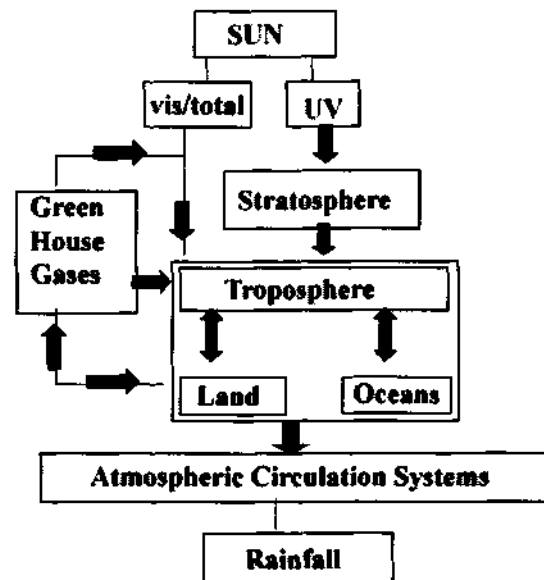


Figure 10.1. Possible Explanation

10.3 Vistas Ahead

We believe that this thesis has shown that even with samples of only a hundred or so years of meteorological data, it is possible to devise mathematical and statistical methods that can detect, with considerable confidence, the effects of solar processes on meteorological parameters like monsoon rainfall on multi-decadal scales. The methods developed here can therefore be thought of as adding considerable value to the analysis of the reliable data that has been directly acquired, even if only for what are relatively short periods from the point of view of long-time climate research.

Many of the methods used here depend on wavelets, which provide a powerful tool for analysis of non-stationary processes. Wavelet analysis has been used here in conjunction with two other new methods. First is a method of significance testing that depends on Monte Carlo-type simulations using matched spectrum/PDF noise signals, rather than reference red or blue noise spectra determined by short-lag correlations. The second method constructs point processes from WTC maxima or minima, and compares them for inter-relations between two variables using regression and unconstrained optimisation methods.

We believe that these methods should have wide applicability to problems encountered in analysing climate change.

References

- [1] Agnihotri R., Dutta K., Bhushan R. and Somayajulu B. L. K., 2002: Evidence for solar forcing on the Indian monsoon during the last millennium, *Earth and Planetary Science Letters*, **198**, 521-527.
- [2] Agnihotri R. and Dutta K., (2003): Centennial scale variations in monsoonal rainfall (Indian, east equatorial and Chinese monsoons): Manifestations of solar variability, *Current Science*, **85**, 459-463.
- [3] Anandakumar K., and Kailas S.V., 1999: *Journal of Aerospace Engineering, Proceedings of International Mechanical Engineering, Part G*, **213**, 143-162.
- [4] Anderson B. M. and Wodehouse C. A., (2005): Let all the voices be heard, *Nature* , **433**, 587-588.
- [5] Arnold N., 2002: Solar variability, coupling between atmospheric layers and climate change, *Phil. Trans. R. Soc. London*, **A360**, 2787-2804.
- [6] Barlaud M., (ed.) 1994: *Wavelets in Image Communication*, Elsevier, Amsterdam, 99-196.
- [7] Beer J., Blinov A., Bonani G., Finkel R. C., Hofmann H. J., Lehmann B., Oeschger H. Sigg A., Schwander J., Staffelbach T., Stauffer B., Suter M. and Wölfli W., 1990: Use of ^{10}Be in polar ice to trace the 11-year cycle of solar activity, *Nature*, **347**, 164-166.
- [8] Bhattacharyya S. and Narasimha R. , Possible association between Indian monsoon rainfall and solar activity, *Geophysical Research Letters*, **32**, 5, doi: 10.1029/2004GL021044, 2005.
- [9] Burroughs W. J., 1992: *Weather cycles*, Cambridge Univ. Press
- [10] Cox D. R., 1962: *Renewal Theory*, Methuen, London.
- [11] Cox D. R. 1972 : The Statistical Analysis of Dependencies in Point Processes, *Stochastic Point Processes*, ed. P. A. W. Lewis, Wiley, New York.
- [12] Cox D. R. and Isham V. 1979: Point Processes. *Chapman and Hall*, London.
- [13] Cox D. R. and Lewis P. A. W. 1966: *Statistical Analysis of Series of Events*, Methuen, London.
- [14] Chui C. K., 1992: *An Introduction to Wavelets*, Academic Press.
- [15] Crow E. L., Davis F. A., and Maxfield M. W., 1960: Statistics Manual, Dover Publications, Inc. New York.
- [16] Daubechies I., 1990: The wavelet transform, time frequency localization and signal analysis, *IEEE transactions on Information Theory*, **36**, 5, 961-1005.
- [17] Daubechies I., 1992: Ten Lectures on Wavelets, *CBMS-NMF Regional Conference Series*.

- [18] Damon P. E. and Laut P., 2004: Pattern of strange errors plagues solar activity and terrestrial climate data, *EOS*, **85**, 39, 370-374,
- [19] Farge M., 1992: Wavelet transforms and their applications to turbulence, *Ann. Reviews of Fluid Mechanics*, **24**, 395-457.
- [20] Feng Bo, Xi-zheng K. E. and Hua-ling Ding, 1998: Wavelet analysis of sunspot numbers, *Chinese Astronomy and Astrophysics*, **22**, 1, 83-91.
- [21] Fligge M., Solanki S. K. and Beer J., 1999: Determination of solar cycle length variations using the continuous wavelet transform, *Astronomy and Astrophysics*, **346**, 313-321.
- [22] Foukal P., and Lean J., 1990: An empirical model of total solar irradiance variation between 1874 and 1988, *Science*, **247**, 556-558.
- [23] Foukal P., North G., and Wigley T., 2004: A stellar view on solar variations and climate, *Science*, **306**, 68-69, 2004.
- [24] Friis-Christensen E. and Lassen K., 1991: Length of the Solar Cycle: An Indicator of Solar Activity Closely Associated with Climate, *Science*, **254**, 698-700.
- [25] Gilman D. L., Fuglister F.J., and Mitchell J. M. Jr. , 1963: On the power spectrum of "red noise". *Journal of Atmospheric Science*, **20**, 182-184.
- [26] Grigoriu M., On the spectral representation method in simulation, *Probabilistic Engineering Mechanics*, **8**, 610-620, 1984.
- [27] Grigoriu M., Simulation of Stationary Non-Gaussian Translation Processes, *Journal of Engineering Mechanics*, **124**, 2, 121-126, 1998.
- [28] Grossman A. and Morlet J., 1984: *SIAM Journal of Mathematical Analysis*, **15**, 723-736.
- [29] Haigh Joanna D., 1996: The impact of solar variability on climate, *Science*, **272**, 981-984.
- [30] Haigh J. D., 1999 (a): A GCM study of climate change in response to the 11-year solar cycle, *Q. J. R. Meteorological Society*, **125**, 871-892.
- [31] Haigh J. D., 1999 (b): Modelling the impact of solar variability on climate, *Journal of Solar and Terrestrial Physics*, **61**, 63-72.
- [32] Haigh J. D., Climate variability and the influence of the sun, *Science*, **294**, 2109-2111, 2001.
- [33] Haigh J. D., Blackman M., and Day R., 2005: The response of tropospheric circulation to perturbations in lower stratospheric temperature, *Journal of Climate*, **18**, 17, 3672-3685.
- [34] Huang N., Zheng S., Long S. R., Wu M. C., Shih H. H., Zheng Q., Yen N., Tung C. C. and Liu H. H., 1998: The empirical mode decomposition and the Hilbert spectrum for nonlinear and non-stationary time series analysis, *Proceedings of Royal Society, London* , **A**, **454**, 903-995.
- [35] Iyengar R. N. and Raghu Kanth S. T. G., 2004: Intrinsic mode functions and a strategy for forecasting Indian monsoon rainfall, *Meteorology and Atmospheric Physics*, (in press).

- [36] Jagannathan P. and Bhalme H. N., 1973: Changes in the Pattern of Distribution of South-west Monsoon Rainfall Over India Associated with Sunspots, *Monthly Weather Review*, **101**, 9, 691-700.
- [37] Jagannathan P. and Parthasarathy B., 1973: Trends and Periodicities of Rainfall Over India, *Monthly Weather Review*, **101**, 4, 371-375.
- [38] Jagannathan P. and Raghavendra V. K., 1964: Wet-Spells in Indian Arid Zones, Jodhpur, India, *Ministry of Education and UNESCO South Asia Cooperation Office, New Delhi*, 648-656.
- [39] Kailas S.V., Bhat G. S. and Kalavathi K., 1995: *Proceedings of sixth Asian Congress in Fluid mechanics*, Singapore 993-997.
- [40] Kailas S.V. and Narasimha R., 1999: *Experiments in fluids*, **27**, 167-174.
- [41] Kailas S.V. and Narasimha R., 2000 : Quasi cycles in monsoon rainfall using wavelet analysis, *Current Science*, **78** , 592-595.
- [42] Kelly P.M. and Wigley T. M. L., 1990: *Nature*, **347**, 460.
- [43] Kelly P.M. and Wigley T. M. L., 1992: Solar cycle length, greenhouse forcing and global climate, *Nature*, **360**, 328-330.
- [44] Kodera K., 2004: Solar influence on the Indian Ocean Monsoon through dynamical processes, *Geophysical Research Letters* , **31**, L24209, doi:10.1029/2004GL020928.
- [45] Kodera K., 2005: Solar influence on troposphere through stratospheric dynamical processes, *Proceedings of SORCE 2005, September 14-16th, Durango, Colorado, USA*.
- [46] Krishna Kumar K. 1997: Seasonal Forecasting of Indian Summer Monsoon Rainfall: diagnostics and Synthesis of Regional and Global signals, *PhD Thesis, Indian Institute of Tropical Meteorology, University of Pune*.
- [47] Krishnakumar K., Rajagopalan B., and Cane M. A., 1999: On the weakening relationship between the Indian monsoon and ENSO, *Science*, **284**, 2156-2159.
- [48] Kronland-Martinet R., Morlet J. and Grossman A., 1987: *International Journal of Pattern Recognition and Artificial Intelligence*, **2**, 97-126.
- [49] Kulkarni J. R., 2000: Wavelet analysis of the association between the southern oscillation and the Indian summer monsoon, *International Journal of Climatology* , **20**, 89-104.
- [50] Labitzke K. and Loon H. van, 1997: The signal of the 11-year sunspot cycle in the upper troposphere-lower stratosphere, *Space Science Reviews*, **80**, 393-410.
- [51] Labitzke K., Austin J., Butchart N., and Knight J., 2002: The global signal of the 11 year solar cycle in the stratosphere: Observations and models, *Journal of Atmospheric and Solar Terrestrial Physics*, **64**, 203-210.
- [52] Lassen K. and Friis-Christensen E., 1995: Variability of the solar cycle length during the past five centuries and the apparent association with terrestrial climate, *Journal of Atmospheric and Terrestrial Physics*, **57**, 8, 835-845.

- [53] Lau K. M. and Weng H., 1995: Climate Signal Detection Using Wavelet Transform: How to make a time series sing, *Bulletin of the American Meteorological Society*, **76**, 12, 2391-2402.
- [54] Lean J., Beer J., and Bradley R., 1995: Reconstruction of solar irradiance since 1610: Implications for climatic change, *Geophysical Research Letters*, **22**, 3195-3198.
- [55] Lean J., ftp://ftp.ncdc.noaa.gov/pub/data/paleo/climate_forcing/solar_variability/lean2000_irradiance.txt, 2004
- [56] Lean J., Wang Y. M., and Sheeley N. R. Jr., 2002: The effect of increasing solar activity on the sun's total and open magnetic flux during multiple cycles: Implications for solar forcing of climate, *Geophysical Research Letters*, **29**, doi: 10.1029/2002GL015880.
- [57] Lee R. B., Gibson M.A., Wilson R.S and Thomas S., 1995: Long-term total solar irradiance variability during sunspot cycle 22, *J. Geophysical Research*, **100**, 1667-1675.
- [58] Mallat S., 1989: Multiresolution approximations and wavelet orthonormal bases of $L^2(R)$, *Transactions of American Mathematical Society*, **315**, 69-87.
- [59] Maraun D. and Kurths J., 2004: Cross wavelet analysis: significance testing and pitfalls, *Nonlinear Processes in Geophysics*, **11**, 4, 505-514.
- [60] Maraun D. and Kurths J., 2005: Epochs of phase coherence between ENSO and Indian monsoon, *Nonlinear Processes in Geophysics*.
- [61] Meehl G. A., 1987: The annual cycle and inter annual variability in the tropical Indian and Pacific ocean regions, *Monthly Weather Review*, **115**, 27-50.
- [62] Mehta V. and Lau K.M., Influence of solar irradiance on the Indian monsoon-ENSO: relation at decadal-multidecadal time scales, *Geophysical Research Letters*, **24**, 159-162, 1997.
- [63] Mendoza B., Perez-Enriquez R., and Alvarez-Madrigal M., 1991: Analysis of solar activity conditions during periods of El Nino events, *Ann. Geophysicae*, **9**, 50-54.
- [64] Meyer Y., 1993: Wavelets: algorithms and applications, *SIAM*, Philadelphia
- [65] Narasimha R. and Kailas S. V., 2001: A Wavelet Map of Monsoon Variability, *Proceedings of the Indian National Science Academy*.
- [66] NASA 2004, <http://science.msfc.nasa.gov/ssl/pad/solar/image/zurich.gif>
- [67] Neff U., Burns S. J., Mangini A., Mudelsee M., Fleitmann D. and Matter A., 2001: Strong coherence between solar variability and the monsoon in Oman between 9 and 6 kyr ago, *Nature*, **411**, 290-293.
- [68] Normand C., 1953: Monsoon seasonal forecasting, *Quarterly Journal of Royal Meteorological Society*, **79**, 463-473.
- [69] Parthasarathy B., Munot A. A. and Kothawale D. R., 1993: *Proceedings of Indian Academy of Science (Earth and Planetary Science)*, **102**, 121-155.

- [70] Parthasarathy B., Munot A. A. and Kothawale D. R., 1995: Contributions from Indian Institute of Tropical Meteorology, Pune : Monthly and seasonal rainfall series for all-India homogeneous regions and meteorological subdivisions: 1871-1994, *Research Report no. RR-065, Indian Institute of Tropical Meteorology, Pune.*
- [71] Rai Choudhuri A., 1999: The solar dynamo, *Current Science*, **77**, 11, 1475-1486.
- [72] Rajeevan M., Pai D. S., and Kumar Anil R., 2005: New statistical models for long range forecasting of southwest monsoon rainfall over India, *NCC Research Report*, **1**.
- [73] Rasmusson E. M. and Carpenter T. H., 1983: The relationship between eastern equatorial Pacific sea surface temperature and rainfall over India and Sri Lanka, *Monthly Weather Review*, **111**, 517-528.
- [74] Reid G. C., 1991: Solar irradiance variations and global ocean temperature, *Journal of Geomagnetism and Geoelectricity*, **43**, 795-801.
- [75] Reid G. C. and Gage K. S., 1998: The climatic impact of secular variations in solar irradiance in secular solar and geomagnetic variations in the last 10000 years, *Kluwer Series*, [Eds. F. R. and A. W. Wplfendale, NATO AS], 225-243.
- [76] Ruzmaikin A. and Feynman J., 2002: Solar influence on a major mode of atmospheric variability, *Journal of Geophysical Research*, **107**, D14, doi: 10.1029/2001JD001239.
- [77] Ruzmaikin A., 2005: Signals from the Nile river, *Proceedings of SORCE 2005, September 14-16th, Durango, Colorado, USA.*
- [78] Shindell D. T., Schmidt G. A., Miller R. L., and Rind D., 2001: Northern Hemisphere winter climate response to greenhouse gas, ozone, solar and volcanic forcing, *Journal of Geophysical Research*, **106**, 7193-7210.
- [79] Shindell D., Faluvegi G., Schmidt G., and Aguilar E., 2005: Present day and historical response to solar forcing in the fully coupled chemistry-climate GISS model E, *Proceedings of SORCE 2005, September 14-16th, Durango, Colorado, USA.*
- [80] Siddhartha S. S., Narasimha R., Basu A. J. and Kailas S. V., 2000: *Fluid Dynamics Research*, **26**, 105-117.
- [81] Sirocko F., Sarnthein M., Erlenkeuser H., Lange H., Arnold M. and Duplessy J. C., 1993: Century-scale events in monsoonal climate over the past 24000 years, *Nature*, **364**, 322-324.
- [82] Solanki S. K., and Fligge M., 1999: A reconstruction of total solar irradiance since 1700, *Geophysical Research Letters*, **26**, 16, 2465-2468.
- [83] Sri Lakshmi S., Tiwari R.K. and Somvanshi V.K., 2002: ANN based prediction of Indian rainfall index (IRF) using ENSO variability and sunspot cycles, *39th Annual Convention and Meeting on Sustainability Science and Environmental Geophysics, 4-6 October 2002, NEERI Nagpur*
- [84] Stager Curt J., 2005: Solar variability and rainfall at Lake Victoria, East Africa, during the last millennium, *Proceedings of SORCE 2005, september 14th-16th, Durango, Colorado, US.*

- [85] Torrence C. and Compo G. P., 1998: A Practical Guide to Wavelet Analysis, *Bulletin of the American Meteorological Society*, **79**, 1, 61-78.
- [86] Torrence C. and Webster P. J., 1998: The annual cycle of persistence in the El Nino/Southern Oscillation, *Quarterly Journal of Royal Meteorological Society*, **124**, 1985-2004.
- [87] Torrence C. and Webster P. J., 1999: Interdecadal Changes in the ENSO-Monsoon System, *Journal of Climate*, **12**, 2679-2690.
- [88] Trenberth K. E., 1997: The definition of El-Nino, *Bulletin of American Meteorological Society*, **78**, 2771-2777.
- [89] Troup A. J., 1965: The 'Southern Oscillation', *Quarterly Journal of Royal Meteorological Society*, **91**, 90-506.
- [90] Tukey J.W., 1950: Sampling theory of power spectrum estimates, *Proceedings of the symposium on Applications of Auto-correlation Analysis to Physical problems, Woods Hole, Massachusetts, June 13-14, 1949*, Office of Naval Research, NAVEXOS-P-735, Washington D.C., 47-67.
- [91] van Loon H., Meehl G. A., and Arblaster J. M., 2004: A decadal solar effect in the tropics in July-August, *Journal of Solar Atmospheric and Terrestrial Physics*, **66**, 1767-1778.
- [92] van Loon H., 2005: A probable influence in the Pacific ocean of the decadal solar oscillation, *Proceedings of SORCE 2005, September 14-16th, Durango, Colorado, USA*.
- [93] Visser K., Thunell R. and Stott L., 2003: Magnitude and timing of temperature change in the Indo-Pacific warm pool during deglaciation, *Nature*, **421**, 152-155.
- [94] Walker G.T., 1923: Correlation in seasonal variation of weather, *VIII. Mem. India Met. Dept.*, **24**, 75-131.
- [95] Walker G. T. and Bliss E. W., 1937: World Weather VI, *Memoirs of Roy. Meteorological Society*, **4**, 39, 119-139.
- [96] Waldmeier M., 1961: The sunspot activity in the years 1610-1960, *Zurich Schulthess and Co*.
- [97] Weng H. Y. and Lau K. M., 1994 : Wavelet, period-doubling and time frequency localisation with application to satellite data analysis, *Journal of Atmospheric Science*, **51**, 2523-2541.
- [98] Wigley T.M.L. and Raper S.C.B., 1990: *Geophys. Res. Lett.* **17**, 2169-2172.
- [99] Willson R. C. and Hudson H. S., 1988: Solar luminosity variations in solar cycle 21, *Nature*, **332**, 810-812.
- [100] Yasunari T., 1990: Impact on Indian monsoon on the coupled atmosphere/ocean system in the tropical Pacific, *Meteorological and Atmospheric Physics*, **44**, 29-41.

532.593
POS